

UC San Diego

UC San Diego Electronic Theses and Dissertations

Title

The response of convection driven by surface buoyancy fluxes to surface mechanical forcing

Permalink

<https://escholarship.org/uc/item/6q0156tj>

Author

Matusik, Katarzyna Ewa

Publication Date

2015

Peer reviewed|Thesis/dissertation

UNIVERSITY OF CALIFORNIA, SAN DIEGO

**The response of convection driven by surface buoyancy fluxes to surface
mechanical forcing**

A dissertation submitted in partial satisfaction of the
requirements for the degree
Doctor of Philosophy

in

Engineering Sciences (Mechanical Engineering)

by

Katarzyna Ewa Matusik

Committee in charge:

Stefan Llewellyn Smith, Chair
Myrl Hendershott
Eugene Pawlak
James Rottman
Kraig Winters

2015

Copyright
Katarzyna Ewa Matusik, 2015
All rights reserved.

The dissertation of Katarzyna Ewa Matusik is approved, and
it is acceptable in quality and form for publication on micro-
film and electronically:

Chair

University of California, San Diego

2015

DEDICATION

To Desi & Louis.

EPIGRAPH

With the new day comes new strength and new thoughts.

—Eleanor Roosevelt

TABLE OF CONTENTS

Signature Page	iii
Dedication	iv
Epigraph	v
Table of Contents	vi
List of Figures	viii
List of Tables	xii
Acknowledgements	xiii
Vita	xvi
Abstract of the Dissertation	xvii
Chapter 1 Introduction	1
1.1 The meridional overturning circulation	1
1.2 Horizontal convection	3
1.2.1 Governing parameters & equations	4
1.2.2 Relevant timescales	7
1.2.3 Previous experimental work	10
1.2.4 Previous numerical work	14
1.3 The effect of surface stress	15
1.4 Motivation and thesis layout	19
Chapter 2 The experiments	20
2.1 Apparatus	22
2.1.1 Mechanical forcing	23
2.1.2 The effect of sink location	24
2.2 Synthetic schlieren (SS)	29
2.2.1 Setup	30
2.2.2 DigiFlow processing	32
2.2.3 MATLAB processing	34
2.3 Conductivity probe	36
2.3.1 Probe traverse	36
2.3.2 Data acquisition	37
2.3.3 Calibration	38
2.3.4 Adjustment for temperature variation	40
2.3.5 Thermocouple measurement	41

2.4	Particle image velocimetry (PIV)	42
2.4.1	The laser	43
2.4.2	Computer wiring	44
2.4.3	DaVis 6.2 software	45
2.4.4	Laser sheet optics	46
2.4.5	Setup	48
2.4.6	Seeding particles	50
2.4.7	Digital image processing	51
2.4.8	PIV processing	51
2.5	Experiment procedure	52
 Chapter 3		
	Experiments with concurrent mechanical and buoyancy forcing imposed on the surface	55
3.1	Qualitative results	58
3.2	Quantitative results	60
3.3	Stability and adjustment	65
3.4	Governing Physics	71
3.4.1	Derivation of the recycling box model equations	72
3.4.2	Nondimensionalization	76
3.4.3	Virtual origin correction	79
3.4.4	Estimation of the turbulent diffusivity	81
3.5	Results of the recycling box model	82
3.6	Discussion	86
3.7	Conclusions	89
 Chapter 4		
	Experiments with competitive mechanical and buoyancy forcing imposed on the surface	92
4.1	Qualitative results	94
4.1.1	Flow features for a low density plume	98
4.2	Quantitative results	100
4.2.1	Flow stability	104
4.3	Scaling arguments	105
4.4	Discussion	108
4.5	Conclusions	111
 Chapter 5		
	Conclusions	114
5.1	Overview and application	114
5.2	Future work	117
 Bibliography	119

LIST OF FIGURES

Figure 1.1:	Schematic of the highly idealized global overturning circulation, obtained from Kuhlbrodt et al. (2007)	2
Figure 1.2:	Photograph of dye tracer transport in horizontal convection forced at the bottom boundary, taken from the experiments of Mularney et al. (2004).	11
Figure 1.3:	Schematic of the experimental setup of Pierce and Rhines (1996). The authors explored the effect of a sloping endwall on the entrainment dynamics of the plume.	13
Figure 2.1:	Schematic of experimental setup used for all experiments.	21
Figure 2.2:	Schematic of experimental setup to investigate the effect of sink location on a solutal buoyancy–driven circulation.	25
Figure 2.3:	Calibration curve used to recover the spatially–averaged (in the spanwise direction) density field.	26
Figure 2.4:	Steady–state maps of the density perturbation for $A = 1$. For each experiment, the tank is initially filled with freshwater, and the saline source density is $\rho_d = 1035 \text{ kg m}^{-3}$	27
Figure 2.5:	Steady–state maps of the density perturbation for $A = 0.08$. For each experiment, the tank is initially filled with freshwater, and the saline source density is $\rho_d = 1035 \text{ kg m}^{-3}$	28
Figure 2.6:	Photograph of the synthetic schlieren setup.	31
Figure 2.7:	A snapshot of the LabVIEW Main Control panel used to traverse the conductivity probe, which integrates a calibration scheme into the data acquisition. The panel plots the conductivity probe’s voltage output as a function of depth in real time.	38
Figure 2.8:	A snapshot of the LabVIEW Calibration panel used to calibrate the conductivity probe.	39
Figure 2.9:	Plot of voltage output from conductivity probe vs. temperature for seven densities. The voltage output linearly increases with increasing fluid temperature.	41
Figure 2.10:	Slope values corresponding to the relationship between the conductivity probe’s voltage output and the temperature of the water plotted against density.	42
Figure 2.11:	Photograph of BNC connections on the back of the laser power supply, as necessary for operation of the Nd:YAG laser.	44
Figure 2.12:	Photograph of computer wiring for the laser and camera. The PTU8 card synchronizes the laser pulse and the camera, while the ethernet cord in the camera interface board connects the camera head to the computer.	45

Figure 2.13:	Plot of laser sheet thickness variation as a function of distance from waist diameter. The maximum thickness that the sheet reaches in the field of view (FOV), corresponding to the blue rectangle, is 1.11 mm.	48
Figure 2.14:	Setup of laser optics and experiment tank. Waterproof black adhesive vinyl lines the inside bottom and sides, as well as the outside wall of the tank. The matte black color absorbs laser light that would otherwise be reflected.	49
Figure 3.1:	Steady-state velocity field for an experiment with $S_{\delta f} = 0.12$, obtained from PIV measurements. The magnitude of the vectors are stretched by a factor of 7 for increased visibility.	59
Figure 3.2:	Mixed layer thickness, d_{mix} , normalized by tank depth vs. $S_{\delta f}$. For values of $S_{\delta f} > 0.42$, the depth of the mixed layer increases linearly with increasing $S_{\delta f}$. The least squares fit (dashed line) corresponds to $d_{mix} = 0.1875 \times S_{\delta f} - 0.0105$	59
Figure 3.3:	Steady-state velocity field for an experiment with $S_{\delta f} = 0.88$. The magnitude of the vectors are stretched by a factor of 7 for increased visibility.	60
Figure 3.4:	Plots of normalized interior density measured by the conductivity probe as a function of normalized depth. Because the conductivity probe could only measure the upper half of the domain, the profiles end just shy of the normalized half-depth of the tank.	62
Figure 3.5:	(a) Normalized interior density at $z \approx -0.5H$ as a function of $S_{\delta f}$ and (b) mean profiles of the interior vertical velocity, W_e	63
Figure 3.6:	(a) Profiles of the normalized buoyancy frequency obtained from SS measurements for various values of $S_{\delta f}$. (b) is a snapshot of the steady-state plume outflow with its corresponding $N^2(z)$ profile superposed on the dye image for an experiment with $S_{\delta f} = 0.86$	64
Figure 3.7:	Ri_B as defined in (3.5) plotted as a function of $S_{\delta f}$. The black circles and red squares correspond to experiments with and without regional mixing, respectively. The experiment closest to the threshold value of $S_{\delta f} \approx 0.42$ corresponds to $Ri_B \approx 4.50$	67
Figure 3.8:	(a) Scaling of the equilibrium mixed layer depth, d_{eq} , derived from the approximately linear relationship between the mixing depth, d_{mix} , and $S_{\delta f}$. (b) plots two mixing depth scalings relevant to buoyancy flux and mechanical energy systems.	70
Figure 3.9:	Simplified schematic of the experimental setup in figure 2.1. A line half-plume with specific buoyancy flux per unit spanwise width, B_0 , is introduced into a rectangular domain with aspect ratio $A = 0.5$	71

Figure 3.10:	Velocity field for an experiment where $S_{\delta f} = 1.25$, obtained from PIV measurements. The horizontal and vertical extent of the eddy, l_e and h_e , respectively, are depicted by corresponding arrows. An estimate of the value of h_e is used in parameterizing $k^*(z)$.	81
Figure 3.11:	Normalized buoyancy profiles vs. normalized depth for select values of $S_{\delta f}$; dashed lines indicate conductivity probe measurements, and solid lines are the solutions to the plume equations.	83
Figure 3.12:	Summary of key experimental quantities (circles) as well as corresponding least squares fits (dashed lines) and recycling box model predictions (solid lines). The subscript <i>norm</i> reiterates that the measured values are normalized by their theoretical analogues.	85
Figure 3.13:	(a) and (b) plot the solutions to the dimensionless boundary layer thickness for all experiments as a function of d_{mix} .	88
Figure 4.1:	(a) Dye visualization of the equilibrated flow field for an experiment where $S_{\delta f} = 0.17$. KMnO ₄ crystals are mixed into the dense source fluid in order to track the plume outflow. (b) plots the corresponding velocity map of the flow.	95
Figure 4.2:	(a) Velocity field for an experiment with $S_{\delta f} = 0.30$, where the buoyancy–driven cell is affected by the surface stress. The magnitude of the vectors are stretched by a factor of 7 for improved visibility, and the colormap corresponds to the velocity magnitude.	96
Figure 4.3:	(a) Dye visualization of an experiment with $S_{\delta f} = 0.30$ and $\rho_d = 1020 \text{ kg m}^{-3}$. This is compared to (b), a dye image of an experiment with $S_{\delta f} = 0.42$ and $\rho_d = 1029 \text{ kg m}^{-3}$.	96
Figure 4.4:	(a) Dye image of an experiment with $S_{\delta f} = 0.77$ where regional mixing is present near the surface. Plume evolution is monitored for 25 min, with the image taken at the end of the interval. (b) shows the plume evolution after 2 hrs for a flow where $S_{\delta f} = 1.21$.	98
Figure 4.5:	(a) and (b) plot the long–time velocity field for an experiment with $S_{\delta f} = 0.14$, obtained from PIV measurements. The time step between the images is 4 hrs. The magnitude of the vectors are stretched by a factor of 5 for improved visibility.	98
Figure 4.6:	Dye image of plume outflow for an experiment with $S_{\delta f} = 0.45$. The dye is solely added to the dense plume fluid, and can be seen in the thin boundary layer at the surface.	99
Figure 4.7:	Plots of normalized interior density measured by the conductivity probe as a function of normalized depth. Because the conductivity probe could only measure the upper half of the domain, the profiles end just shy of the normalized half–depth of the tank.	101

Figure 4.8:	(a) Normalized buoyancy frequency profiles as a function of depth for select $S_{\delta f}$ values. The profiles are obtained from SS images by horizontally averaging ρ_z outside the plume as well as any patches of turbulence.	102
Figure 4.9:	Horizontally averaged vertical profiles of u , the horizontal velocity, for an experiment with $S_{\delta f} = 0.30$. The cross and circle line markers correspond to profiles obtained from the first set and second set of data acquisition, respectively.	103
Figure 4.10:	(a) Normalized maximum velocity magnitude, $u_{max}^{-1}\sqrt{u^2 + w^2}$, obtained from PIV measurements as a function of $S_{\delta f}$. The vertical lines are associated with the spread between the two recorded data sets per each experiment. (b) maximum positive ψ_{max} in the flow.	104
Figure 4.11:	Rib as defined in eq. (3.5) plotted as a function of $S_{\delta f}$. The red squares correspond to experiments where no mixing is evident in the flow, and the black circles correspond to experiments with visible mixing.	105
Figure 4.12:	Normalized average horizontal surface velocity, obtained from PIV measurements by averaging $u(z)$ in a 3 cm interval approximately 1.5 cm below the surface.	107
Figure 4.13:	Boundary layer thickness scaled by (4.2) plotted as a function of $S_{\delta f}$. The vertical lines correspond to the spread between recorded data sets per each experiment.	107
Figure 4.14:	Plot of t^* as a function of $S_{\delta f}$. The vertical lines represent the spread in values between two recorded data sets.	109

LIST OF TABLES

Table 1.1:	Non-exhaustive list of relevant work pertaining to horizontal convection, sorted by publication year and alphabetically by the first author's last name. E = experimental, N = numerical, A = analytic.	18
Table 2.1:	Varying input parameters for synthetic schlieren processing.	33
Table 2.2:	Relevant specifications of the New Wave Research Solos 120 15Hz Nd:YAG laser used for PIV measurements.	43
Table 2.3:	Key characteristics of HighRes CCD sensor located inside the Image Compact camera used for PIV image recording.	50
Table 3.1:	Summary of relevant quantities for concurrent experiments.	57
Table 3.2:	Table summarizing asymptotic solutions to plume equations. For $S_{\delta f} < 0.42$, the quantities match exactly those predicted by the recycling box model of Hughes et al. (2007). For $S_{\delta f} > 0.42$, the solutions become functions of d_{mix}	84
Table 4.1:	Summary of experiments in which a surface stress is acting against a buoyancy driven circulation at the surface.	93

ACKNOWLEDGEMENTS

First and foremost, I'd like to thank my advisor, Stefan Llewellyn Smith, for being readily available for thoughtful discussion, for funding and advising me all of these years, and for allowing me to travel to universities and conference proceedings. Not only did I have the pleasure of broadening my knowledge through your guidance, but also of meeting many wonderful people through the opportunities with which you presented me. And thank you for introducing me to Andrew.

Secondly, I'd like to thank Myrl Hendershott, Geno Pawlak, Jim Rottman, and Kraig Winters for serving on my committee. I appreciate you making the time to meet with me, either individually or during my senate and follow-up presentations. Each of you at one time or another provided useful feedback and guidance when I required it. Thank you to Bill Young and Sarah Gille as well, who also each met with me on various occasions. Thank you Geno for entrusting me with your laser equipment.

Thank you Ross Griffiths and Kial Stewart. You took the time to carefully explain every angle of the experimental setup which ultimately became the framework of my thesis experiments. Thank you Ross for so openly welcoming me to the department. The knowledge I gained through conversation with the GFD group and shadowing Kial in lab proved invaluable in setting up my experiments back home and narrowing down a thesis topic. Also, thank you to Candida and Ross for housing me for one month, making me feel very much at home, and introducing me to Candida's homemade pavlova; it has since become my favorite dessert.

I couldn't have set up important components of my experiments without the help of Nick Busan, Tom Chalfant, and Mike Watson. Thank you for your willingness and promptness in helping me with various lab-related projects, like building a casing for my electroluminescent light sheet and a support for the linear actuator. I also greatly enjoyed our conversations. Thank you to Steve Roberts for fixing my light sheet when I thought all hope was lost, and Chris Cassidy for helping me cut a tank barrier. All five of you contributed greatly to my experimental setup, and never made me feel like I wasn't a priority. I would also like to thank Janet Meade and J.V. Agnew for placing all of my orders and reimbursements, and for all the friendly conversations.

I wouldn't have gained the confidence I now have in performing experiments if it

wasn't for my experience in Cambridge, and specifically if it wasn't for meeting Stuart Dalziel. I learned so much in such a short period of time while working in the GKB laboratory. Thank you Stuart for taking the time to explain lab techniques and DigiFlow macros. Thank you also to Paul Linden, for not only serving as my advisor during my time at DAMTP, but for always making yourself available to meet in San Diego, and never failing to provide useful discussion.

Thank you Javier Rodriguez-Rodriguez for the many coffee breaks at Cups during your summer visits. You are the jack of all trades in your ability to formulate an experiment out of an interesting problem as well as successfully describe it with a mathematical model. Your passion is inspiring, and advice invaluable in finishing this work.

Last but certainly not least on the academic spectrum, I'd like to thank the MAE administrative staff, specifically Charlotte Lauve, Linda McKamey and Michelle Vavra Cacho, some of whom have since left. You have made any and all administrative tasks painless. You were there for the students, and it truly showed.

Thank you Michael Gollner and Ryan Gehmlich for letting me borrow lab equipment, but more importantly for being my friends. Thank you to my family for supporting me through all of these years of school. Thank you Kim for literally putting clothes on my and Andrew's backs and food on our table. Your care packages and words of encouragement never fail to brighten my day. Thank you to my friends for the laughs and support throughout my time at UCSD. Tullo, you have kept me sane since second grade; I feel like I owe you my first born.

Lastly, I'd like to thank my rock, Andrew. You continue to inspire me with your efficiency, drive, and patience. Anything you set out to do, you succeed in, and it is such a privilege to watch. Thank you for listening to me the many times I needed to discuss my research with someone, and for always offering sage advice.

I'd like to also dedicate this thesis to Katie Osterday. We would have most likely been graduating around the same time, and celebrating together. Your contagious laughter that used to resonate throughout these buildings is extremely missed.

Parts of chapter 3 are currently being prepared for publication under the citation: Matusik, K. E. & Llewellyn Smith, S. G. "The response of surface buoyancy flux–driven convection to localized mechanical forcing on the same boundary". The thesis author is

the primary investigator and author of this paper. The work was funded by NSF Grant OCE1259580.

VITA

2008	B. S. in Chemical Engineering <i>cum laude</i> , University of California, San Diego
2008	Undergraduate Student Researcher, University of California, San Diego
2010	M. S. in Mechanical Engineering, University of California, San Diego
2012	David Crighton Research Fellow, University of Cambridge, UK
2012	Graduate Teaching Assistant, <i>MAE 105: Introduction to Mathematical Physics</i> , University of California, San Diego
2013	Graduate Teaching Assistant, <i>MAE 108: Probability and Statistical Methods for Mechanical and Environmental Engineering</i> , University of California, San Diego
2015	Ph. D. in Engineering Sciences (Mechanical Engineering), University of California, San Diego

PUBLICATIONS

Matusik, K.E. & Llewellyn Smith, S.G. “The response of surface buoyancy flux–driven convection to localized mechanical forcing on the same boundary”. 2015 (in preparation).

ABSTRACT OF THE DISSERTATION

The response of convection driven by surface buoyancy fluxes to surface mechanical forcing

by

Katarzyna Ewa Matusik

Doctor of Philosophy in Engineering Sciences (Mechanical Engineering)

University of California, San Diego, 2015

Professor Stefan Llewellyn Smith, Chair

Experiments have been performed to gain insight into the response of a surface buoyancy flux–driven circulation to localized input of mechanical energy. The mechanical energy is provided via a surface stress imposed along the same boundary as the buoyancy forcing. Both the case of the surface stress acting in the same direction as the sense of the circulation driven by the buoyancy forcing as well as against it are explored. The nondimensional ratio of mechanical to buoyancy forcing, $S_{\delta f}$, is used to distinguish between distinct regimes that exist for each experiment set, and is maintained at $\mathcal{O}(1)$.

In the case where surface buoyancy forcing and surface stress support a circulation in the same direction on the upper boundary, the overarching result is that the surface stress induces small-scale turbulence once the shear is strong enough to overturn

the local stratification, corresponding to the threshold of $S_{\delta f} > 0.42$. The experiments are compared to numerical results of the recycling box model of Hughes et al. (2007) with varying mixing in the vertical. Experimental measurements agree satisfactorily with theory, and outline the response of the system to various mixing depths.

If the stress is in competition with the buoyancy forcing on the upper boundary, experiments reveal a suite of regimes in $S_{\delta f}$ in which the flow response varies. Briefly, full-depth buoyancy–driven convection persists for $S_{\delta f} < 0.20$, where the surface stress acts passively on the underlying circulation. For $0.20 < S_{\delta f} < 0.50$, a competitive regime develops in which the flow periodically adjusts to the rivalry of the two forces by altering both the thickness of the boundary layer and the strength of the circulation. Once mixing develops for $S_{\delta f} \gtrsim 0.50$, the boundary layer flow competes strongly with the buoyancy–driven circulation, which is made shallow through an input of stabilizing buoyancy flux into the plume via mixing. For $S_{\delta f} > 0.87$, a two-cell circulation develops, featuring a shallow stress–driven cell overlying a deeper buoyancy–driven cell. The experiment results are applicable in the oceanographic context to imposed wind stress on the ocean surface simultaneously subject to surface buoyancy fluxes.

Chapter 1

Introduction

1.1 The meridional overturning circulation

It is generally acknowledged that the oceans are not merely stagnant pools of cold and salty water that lie beneath a surface trapped, mechanically–driven circulation. Rather, to first order, the zonally integrated oceans encompass a large–scale meridional overturning circulation, hereafter referred to as the MOC (Kuhlbrodt et al., 2007). The prevailing stratification includes a steep thermocline overlaying a relatively weak and stably stratified interior. Various closely coupled atmosphere–ocean processes are thought to be responsible for maintaining this nearly global stable stratification as well as driving the deep overturning circulation (Wunsch, 2005).

Broadly speaking, surface waters experience annual net heating at equatorial latitudes and net cooling at the poles. In order for Earth to remain in statistical thermal equilibrium, a net poleward transport of heat is required, and accordingly achieved through the circulation of surface waters, which is mainly driven by wind stress (Hughes and Griffiths, 2006). At polar latitudes, densified water masses sink along topography in the form of localized plumes (Munk, 1966; Killworth, 2001). The dense gravity currents entrain surrounding water upon downwelling, thus modifying the fluid properties before spreading laterally along the bottom boundary or at intermediate depths (Hughes and Griffiths, 2006). The circulation is closed via upwelling processes that transport abyssal waters to the ocean surface.

Figure 1.1 displays a highly idealized schematic of the global overturning circu-

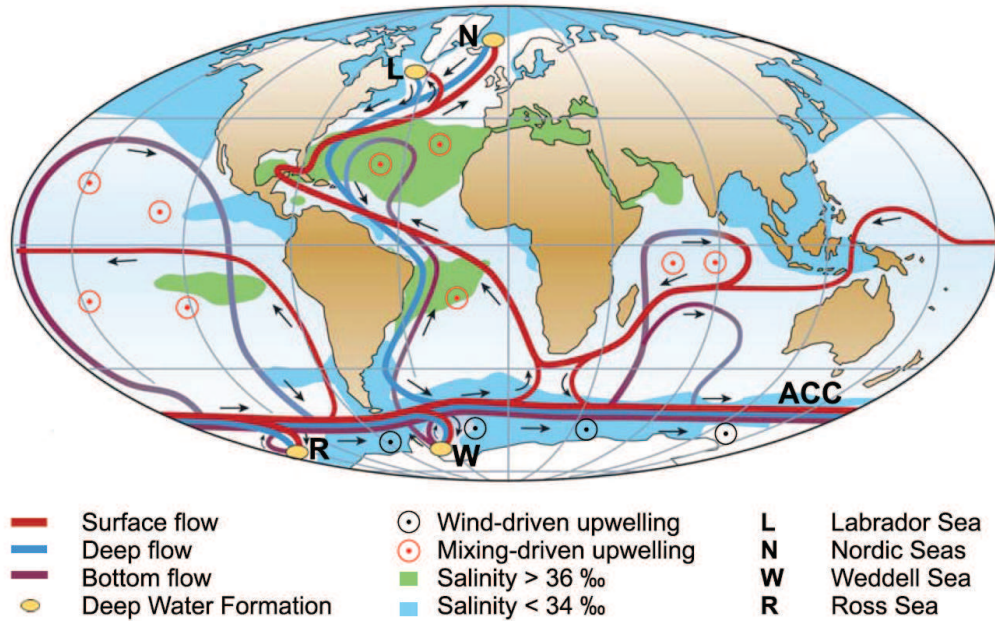


Figure 1.1: Schematic of the highly idealized global overturning circulation, obtained from Kuhlbrodt et al. (2007). Deep water formation occurs at high northern and southern latitudes, feeding the North Atlantic Bottom Deep (NADW) and the more dense Antarctic Bottom Water (AABW). These water masses sink as localized plumes, outflowing towards equatorial latitudes. The circulation is closed via two dominant mechanisms: mixing–driven upwelling that occurs over a broad region near equatorial latitudes, and wind–driven upwelling caused by strong westerly winds over the Southern Ocean.

lation (Kuhlbrodt et al., 2007). The system is composed of two main cells, one which includes the North Atlantic Deep Water (NADW), and an underlying abyssal circulation consisting of the Antarctic Bottom Water (AABW). At high northern latitudes, the NADW is mainly formed by winds both cooling the ocean surface and densifying the local waters through evaporative cooling. At high southern latitudes, similar mechanisms work to decrease the buoyancy of local water masses. Katabatic winds and sea ice formation result in intensely cooled and dense waters that form the AABW, which underflows the NADW. These areas of confined downwelling of dense waters are tightly coupled to the distribution of surface buoyancy fluxes created by the removal of both heat and freshwater (Kuhlbrodt et al., 2007).

With regard to the upper leg of the circulation, strong westerly winds over the Southern Ocean are responsible for the creation of a divergent velocity field on the ocean

surface, leading to upwelling of deep waters. Mixing across isopycnals likewise upwells fluid from below, albeit over a more broadly distributed region near equatorial latitudes. Surface currents then transport this relatively light water toward higher latitudes and close the circulation.

Presently, the main drivers of the MOC are thought to be surface buoyancy fluxes (e.g. Hughes and Griffiths, 2006) and surface wind stress (e.g. Toggweiler and Samuels, 1997). The former drive a flow by setting up pressure gradients due to horizontal variations in density. The latter establish zones where Ekman transport brings dense waters from below to the ocean surface. Various other processes also contribute to maintaining the MOC, primarily by inducing diapycnal mixing (Wunsch and Ferrari, 2004). Surface and internal gravity waves triggered by atmospheric winds and tides, as well as topography, result in localized regions of turbulence. It has also been theorized that the biosphere plays an active role in enhancing mixing (Dewar et al., 2006). Nevertheless, it is the interplay between wind–driven upwelling and surface buoyancy fluxes that primarily results in the mean MOC and the related abyssal stratification, whereby down-gradient transport of density is enhanced through mixing processes.

The MOC not only strongly sets the stratification and distribution of both heat and water masses in the oceans, but it also controls the global redistribution and storage of chemical species, like carbon dioxide (Kuhlbrodt et al., 2007). As such, the MOC plays a central role in the earth’s climate. A reorganization of this overturning, as might be induced by anthropogenic global warming, is likely to cause varying degrees of change to the marine ecosystem in the Atlantic Ocean (Schmittner, 2005) as well as to the global distributions of surface winds, rainfall, evaporation, and soil moisture (Vellinga and Wood, 2002).

1.2 Horizontal convection

The overturning circulation that results from a differential buoyancy or buoyancy flux imposed along a horizontal boundary is referred to as horizontal convection (Hughes and Griffiths, 2008). The study of this circulation is largely motivated by its relevance to the global ocean circulation, which has been acknowledged by the pioneering

work of Sandström (1908) and Rossby (1965), among others. Along with its relevance to the MOC, horizontal convection may also be exploited in industrial applications, such as modulating temperature conditions in buildings (Linden, 1999), as well as optimizing the large-scale manufacture of glass (Chiu-Webster et al., 2008).

Horizontal convection differs from the more commonly studied types of convection, such as the classical Rayleigh–Bénard or Grashof convections, in that only one of the buoyancy sources promotes fluid motion when applied at a boundary, and overturning may take place without the presence of an instability. The source responsible for setting fluid in motion is termed the destabilizing buoyancy source, and works to reduce or break down the stabilizing density gradient. On the other hand, the stabilizing buoyancy source strives to do the opposite by maintaining stable density gradients in the flow. To further clarify this nomenclature, consider a tank initially filled with freshwater, subject to heating on the left-hand half of the base and cooling on the right-hand half of the base such that the net input of buoyancy is zero. The heated section of the boundary warms surrounding fluid through the mechanisms of conduction and/or convection, rendering it less dense than the environment, and consequently promoting motion toward the upper boundary of the tank; in this context, the heat input is a destabilizing buoyancy source as it is responsible for creating the overturning. Simultaneously, the cooled base is working to maintain the stable density gradient in the tank, and is thus the stabilizing buoyancy source.

1.2.1 Governing parameters & equations

The relevant parameters which describe the steady-state circulation maintained by a horizontal buoyancy flux include the Rayleigh and flux Rayleigh number, respectively,

$$Ra_{\Delta b} = \frac{\Delta b L^3}{\nu \kappa} \quad \text{or} \quad Ra_B = \frac{BL^3}{\nu \kappa^2}, \quad (1.1)$$

the aspect ratio,

$$A = \frac{H}{L}, \quad (1.2)$$

and the Prandtl number (or the analogous Schmidt number for a solute),

$$Pr = \sigma = \frac{\nu}{\kappa}, \quad (1.3)$$

where Δb (m s⁻²) is the imposed specific buoyancy, B (m³s⁻³) is the imposed rate of supply of specific buoyancy per unit box width, H and L are the box height and length, respectively, ν is the kinematic viscosity of the fluid, and κ is the diffusivity of the stratifying species (Hughes and Griffiths, 2008). In this formulation, L has been used in place of H in the definition of $Ra_{\Delta b}$ and Ra_B on the grounds that it is the box length which characterizes the distance over which heat (or the stratifying species) must be transported in horizontal convection. The vorticity and density equations describing the two-dimensional (2D), steady-state flow in the Boussinesq approximation are

$$\frac{\partial(\psi, \nabla^2 \psi)}{\partial(x, z)} - \nu \nabla^4 \psi - b_x = 0, \quad (1.4)$$

$$\frac{\partial \psi}{\partial x} \frac{\partial b}{\partial z} - \frac{\partial \psi}{\partial z} \frac{\partial b}{\partial x} = \kappa \nabla^2 b, \quad (1.5)$$

for constant κ , where x and z are the horizontal and vertical coordinate, respectively, the density is given by $\rho = \rho_0(1 - g^{-1}b)$ where b is the buoyancy and ρ_0 is a reference density, and $\psi(x, z)$ is the streamfunction defining the velocity components $(u, w) = (-\psi_z, \psi_x)$. In the boundary layer, scaling arguments reveal that the main balance in (1.4) is between the diffusion and buoyancy terms for large Pr (Rossby, 1965). Thus, diffusion of the stratifying species through the boundary layer is balanced by buoyancy-driven advection of fluid in the plume. The mechanism of diffusion is essential in maintaining a horizontal circulation and evolving to an equilibrated state. If it were neglected, the tank would fill up with fluid of one density, since there would be no mechanism by which to transfer buoyancy out of the volume. Following the analysis of Rossby (1965) for the boundary layer region, appropriate scalings are

$$x \sim Lx^* \quad z \sim \delta_{bl} z^* \quad \psi \sim \psi_{bl} \psi^* \quad b \sim \Delta b_{bl} b^*, \quad (1.6)$$

where the subscript *bl* emphasizes that the scaling is valid in the boundary layer. Inside the boundary layer, vertical variations in the flow dominate those in the horizontal. Within this limit, the dimensionless forms of (1.4) and (1.5) are,

$$\frac{\nu \psi_{bl}}{\delta_{bl}^4} \{ \psi_{zzzz} \} \sim \frac{\Delta b_{bl}}{L} \{ b_x \}, \quad (1.7)$$

$$\frac{\psi_{bl} \Delta b_{bl}}{L \delta_{bl}} \left\{ \frac{\partial \psi}{\partial x} \frac{\partial b}{\partial z} - \frac{\partial \psi}{\partial z} \frac{\partial b}{\partial x} \right\} \sim \frac{\kappa \Delta b_{bl}}{\delta_{bl}^2} \{ b_{zz} \}, \quad (1.8)$$

where asterisks are dropped for clarity and nondimensional quantities are contained within the curly brackets. Equating coefficients, (1.8) results in the balance

$$\psi_{bl} \sim \frac{\kappa L}{\delta_{bl}}, \quad (1.9)$$

which may be substituted into (1.7) in order to obtain a scaling for the boundary layer thickness, δ_{bl} , given in terms of the Rayleigh number by

$$\frac{\delta_{bl}}{L} \sim Ra_{\Delta b}^{-1/5} \sim Ra_B^{-1/6}, \quad (1.10)$$

where the buoyancy flux B is scaled by $B \sim \kappa L \Delta b_z$. The volume transport per unit spanwise width (ψ_{bl}) then scales as

$$\frac{\psi_{bl}}{\kappa} \sim Ra_{\Delta b}^{1/5} \sim Ra_B^{1/6}. \quad (1.11)$$

The boundary layer scalings given in (1.10) and (1.11), first derived by Rossby (1965), are valid for large Pr and $A \sim \mathcal{O}(1)$. These predicted scalings have been found to be consistent with more recent experimental (e.g. Mullarney et al., 2004) and numerical works (e.g. Beardsley and Festa, 1972; Rossby, 1998; Hughes et al., 2007).

Hughes et al. (2007) derive similar scalings to that of Rossby (1965) by considering an inviscid model which describes a destabilizing buoyancy source in a confined space with a sink of buoyancy located on the same boundary. The addition of a sink to remove buoyancy at an equal rate at which it is supplied requires the advection of the interior density field to be set by vertical diffusion of the stratifying species out of the volume. The equations describing this “recycling box” model are derived from appropriate modifications to the plume equations of Baines and Turner (1969) characterizing the filling–box model by considering the steady–state version of the problem. The scalings for the boundary layer thickness and streamfunction in the case of a line half–plume are

$$\frac{\delta_{bl}}{L} = 2.06 \times 2^{-1/6} E^{-1/3} Pr^{-1/6} Ra_B^{-1/6}, \quad (1.12)$$

$$\frac{\psi_{bl}}{\kappa^*} = 1.83 \times 2^{1/6} E^{1/3} Pr^{1/6} Ra_B^{1/6}, \quad (1.13)$$

where κ^* is the diffusivity of the stratifying species. The scalings are valid in the presence of turbulent mixing, for which κ^* embodies a turbulent mixing coefficient. For the

scalings (1.12)–(1.13), the parameters Ra_B and Pr are defined with the turbulent mixing coefficient, κ^* , in place of the molecular value when appropriate. In this context, the boundary layer thickness is defined as the region of the flow which encompasses 95% of the top-to-bottom density difference in the domain. The entrainment constant, E , first introduced by Morton et al. (1956), relates the mean vertical velocity in the plume to the inflow velocity at the plume edge by the relation $U_e = EW_p$, where U_e is the horizontal inflow velocity from infinity and W_p is the plume centerline velocity. This empirical constant takes on a value of 0.1 when Gaussian profiles are employed (Baines and Turner, 1969). Hughes et al. (2007) also derive a scaling for the maximum streamfunction, which incorporates the effect of entrainment occurring outside of the boundary layer,

$$\frac{\psi_{max}}{\kappa^*} = 2E^{1/2} \left(\frac{H}{L}\right)^{1/2} Pr^{1/4} Ra_B^{1/4}. \quad (1.14)$$

The derivation of the recycling box model equations are described in further detail in § 3.4.1, as they form the theoretical base for part of the current work.

1.2.2 Relevant timescales

Several timescales arise in the adjustment process of horizontal convection experiments (Hughes and Griffiths, 2008). The overturning timescale, $\tau_\psi = a \psi_{max}^{-1}$, where a is the tank area, $L \times H$, is the duration of time required for the plume to advect surface waters through the full volume. Transient adjustment to steady state has been shown to occur on the order of this overturning timescale in experiments where convection is driven by a destabilizing source of salt (Stewart et al., 2012). Because ψ_{max} is not known *a priori*, a conservative estimate of its value is instead used. For a solute-driven circulation, the lower limit of ψ_{max} occurs for the case of a non-entraining plume, and is equal to the volumetric flow rate per spanwise width of the saline water source, Q_d . The “filling timescale”, $\tau_f = a Q_d^{-1}$, is the period of time required for the dense source input to replace all of the fluid in the experiment, and serves as a conservative upper bound on the time required for advective adjustment to equilibrium. All experiments considered in this work are allowed to run for at least $6 \times \tau_f$.

The short diffusive timescale, $\tau_h = \delta_{bl}^2 \kappa^{-1}$, estimates the time required for the

boundary layer to adjust to a boundary condition. Generally, the boundary layer thickness is $\mathcal{O}(\text{mm})$, while the lower limit of κ for salt is $\mathcal{O}(10^{-9}) \text{ m}^2 \text{ s}^{-1}$. Thus, for a solute–driven circulation, this timescale is reached in approximately one day, and is feasible to achieve during any given experiment.

The longest timescale to appear in the adjustment process is the long diffusive timescale, $\tau_H = H^2 \kappa^{-1}$, which serves as a measure of the time necessary for diffusion to act on the whole depth of the tank and thus fully adjust the interior density gradient. In experiments with differential heating, this timescale is achieved on the order of days (Coman et al., 2006). For a solute–driven circulation, the diffusive timescale is $\mathcal{O}(\text{yrs})$ due to the relatively small mass diffusivity of salt, and is therefore not achievable in an experimental setting. However, depending on the initial conditions of the experiment, it may not be an appropriate measure of the time required to obtain an equilibrated flow. The advecting plume is more efficient at transporting the imposed buoyancy flux into the tank interior, and therefore diffusion is not the sole mechanism acting to ventilate the domain. To validate this point, consider an experiment tank initially filled with freshwater, into which a dense plume is introduced on the surface near one endwall of the tank. During transient adjustment, the dense plume will penetrate the full depth of the tank from the onset, and act as the principal transporter of the density anomaly into the interior. If, however, the same experiment is initialized with dense water in the tank in lieu of freshwater, the saline water source will eventually develop a full–depth plume, but only once molecular diffusion has acted on the whole of the interior. In the latter case, diffusion is necessary to erode the stratification beyond the plume outflow. In both cases, the steady–state flow is identical, but the adjustment process is quite different, with the latter scenario requiring a longer timescale to reach an equilibrated state. In reality, the long diffusive timescale is a very conservative upper limit to reach equilibrium; even when the plume must wait for diffusion to erode the stagnant layer below it, the process is expedited by penetrative convection which works to increase the plume penetration depth at a faster rate than would otherwise be achieved via molecular diffusion (Vreugdenhil et al., 2015).

Various authors have reported both experimental and numerical work in which equilibration times are at least an order of magnitude less than those given by the long

diffusive timescale (e.g. Mullarney et al. 2004; Stewart et al. 2012; Hazewinkel et al. 2012; Barkan et al. 2013; Gayen et al. 2014). To explain this disparity in timescales, Griffiths et al. (2013) explored transient adjustment of horizontal convection following a perturbation to the boundary condition in the cases where convection is forced by either an imposed heat flux or a temperature difference at the boundary. For the configuration of an imposed heat flux, Q , through half of the base and a fixed cold temperature, T_c , over the cooling half (the more relevant configuration for the experiment setup presented in chapter 2) the authors find that an increase in Q causes the box to readjust to the new condition on the timescale given by

$$\tau_B \approx \frac{1.4\delta_{bl}H}{\kappa}. \quad (1.15)$$

Written in terms of the flux Rayleigh number and aspect ratio, this timescale is

$$\tau_B \approx \frac{2.06 \times 2^{5/6} E^{-1/3} H L P r^{-1/6} R a_B^{-1/6}}{\beta \kappa}, \quad (1.16)$$

where the constant β is equal to 1.4 from DNS simulations (Gayen et al., 2014). This timescale is determined by conductive heat loss across the boundary layer, and is approximately 4 times as long as the overturning timescale, τ_ψ , with more rapid adjustment expected for larger $R a_B$. An increase to T_c yields a readjustment time of the same order, because the perturbation has a duplicate overall effect as one created by an increase in the heat input. DNS simulations and thermally–driven convection experiments confirm exponential readjustment to a new equilibrium state, verifying that the evolution is governed by mechanisms acting through the thin boundary layer with no significant dependence on the role of diffusion through the full domain.

In the case where Q is decreased (or T_c decreased), convection becomes limited to a shallow cell of height $H - d$, where d is the height of the stagnant fluid. The temperature evolution in the stagnant fluid is then expected to be modeled by conduction through the layer, with a timescale for readjustment on the order of

$$\tau_d = \frac{4d^2}{\pi^2 \kappa}. \quad (1.17)$$

DNS simulations find that the timescale to reestablish equilibrium is approximately 1–1.3 times longer when Q is decreased as opposed to increased. For a decrease in T_c ,

readjustment is estimated to take 3.4 times longer than required for an increase in T_c . In this sense, diffusion in the interior only plays a substantial role in reaching an equilibrium state by reestablishing deep circulation when the applied perturbation leads to a temporary shutdown of the plume, i.e. in the case of net cooling.

More recent experiments by Vreugdenhil et al. (2015), utilizing the setup of Stewart et al. (2012), explored the resulting circulation following an increase in mechanical forcing, achieved by grid mixing, through the upper half of the domain. The mechanical forcing is increased by an order of magnitude, leading to a net flux of buoyancy into the plume. The authors find that the buoyancy–driven circulation will re-equilibrate to this buoyancy input in approximately $2\tau_B$, or on the order of 17 hrs. The authors note the presence of penetrative convection at the base of the plume, which expedites the process of reestablishing a full–depth circulation.

1.2.3 Previous experimental work

Laboratory work designed to investigate the flow features of horizontal convection dates back to the experiments of Sandström (1908). Sandström positioned two flat copper coils, one carrying heated water and the other carrying cooled water, at different heights and at opposite ends of a long, narrow tank filled with ambient water, and observed the developed flow field. He concluded that a sustained circulation was only possible when the heated coil was placed at a level below the cooled coil, a statement that later became known as Sandström’s principle or Sandström’s theorem (Jeffreys, 1925). His findings sparked a series of numerical and laboratory work that discounted the theorem by proving that heating and cooling at the same level does in fact support a circulation in the box when in steady state (e.g. Rossby, 1965, 1998; Mularney et al., 2004; Wang and Huang, 2005; Coman et al., 2006; Stewart et al., 2012). Specifically, the work of Coman et al. (2006) recreates the Sandström experimental setup, and proves the existence of a substantial, persistent circulation for all configurations of the copper coils. It has now been established that Sandström may have misinterpreted his experiments as showing a vanishing flow on account of the order-of-magnitude reduction in velocities from an earlier transient period. Moreover, the thermodynamic analysis of his work neglected diffusion (Defant, 1961), which is essential if heat is to enter or leave

the fluid at the boundary or sources (Coman et al., 2006).

Experimental work which explores horizontal convection forced by differential heating at a boundary reveals qualitatively similar flow features to those exhibited by the MOC (e.g. Rossby, 1965; Mullarney et al., 2004; Wang and Huang, 2005). Specifically, the thermally equilibrated flow develops a thin boundary layer adjacent to the forcing boundary. The boundary layer fluid supplies a narrow vertical plume located against an endwall, transporting fluid to the opposite boundary, at which point it horizontally outflows into the interior. The convective cell is closed via a relatively slow vertical flow through the box interior in the direction of the forcing boundary with entrainment present at all depths. Apart from the steep density gradient in the boundary layer, the stratification in the interior is relatively weak and stable. The convective cell is highly asymmetric because the advecting plume is more efficient than down-gradient diffusion at transporting density anomalies into the box interior (Rossby, 1965). As supported mathematically in Paparella and Young (2002), because there can be no net vertical buoyancy flux through any arbitrary level when the system is in equilibrium, the advective buoyancy transport is confined to a narrow plume, whereas the remainder of the volume is stabilized via diffusion.



Figure 1.2: Photograph of dye tracer transport in horizontal convection forced at the bottom boundary, taken from the experiments of Mullarney et al. (2004). A uniform heat flux per unit area is imposed on the left-hand half of the tank base, and a uniform temperature of 16°C is imposed on the right-hand side of the tank. The plume is observed to be turbulent in steady state.

Figure 1.2 shows the left-hand side of a thermally equilibrated horizontal convection experiment, taken from Mullarney et al. (2004). The rectangular tank in which the convection takes place is narrow, with $A = 0.16$. The lower boundary is forced

by a uniform heat flux imposed on the left-hand side of the tank and a constant temperature of 16°C on the right-hand side. The range of Rayleigh numbers explored is $6.5 \times 10^{12} \leq Ra_B \leq 6.84 \times 10^{14}$, where Ra_B is based on the applied input heat flux. Tracer dye is injected and subsequently advected by the convection. The thermally equilibrated flow field is shown to develop a stably stratified boundary layer above the forcing base which feeds into an entraining endwall plume. This upwelling plume is strongly confined to the wall, and found to be turbulent, producing an eddying horizontal outflow into the tank. The flow recirculates to the forcing boundary via broad downwelling in the interior. The authors note two important findings from the experiments: the plume is turbulent for Ra_B in excess of 10^{12} , and a convective mixed layer (CML) is responsible for eroding the stable temperature gradient above the heated part of the base, which subsequently feeds into the plume. Thus, all fluid fluxing out of the boundary layer toward the destabilizing source must first enter the CML before interacting with the plume.

The majority of laboratory experiments which simulate horizontal convection have been carried out with heat as the stratifying species, in which either a gradient (e.g. piecewise, linear, etc.) of constant temperature, a heat flux, or a hybrid thereof, is imposed at a single horizontal boundary. Using heat to drive the circulation maintains $Pr \sim \mathcal{O}(1)$, a value relevant to the oceans. It also has the benefit of not introducing spurious dynamics that may arise when a sink is added to the experimental setup for the purpose of maintaining a zero net volume flux. Moreover, due to the greater diffusion coefficient of heat, these experiments may be run over a long diffusive timescale, τ_H , which is not feasible when a stratifying species such as salt is used to generate the buoyancy flux. However, salt–water experiments are easier to insulate, so that environmental effects are minimized, and higher Ra_B and Pr regimes may be achieved due to the smaller value of κ for salt.

Experiments driven by solutal buoyancy fluxes were first reported in Pierce and Rhines (1996), utilizing the setup shown in figure 1.3. An array of sources and sinks at the surface of the tank actively pump water into and out of the system, respectively, in order to maintain a zero net volume flux. The authors argue that the volume flux has a negligible effect on the overall flow dynamics if it is small compared to the overturning

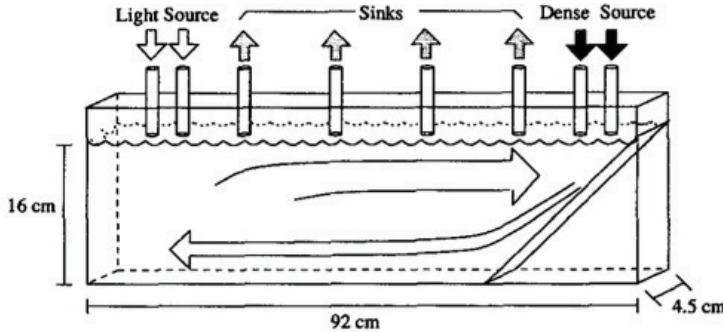


Figure 1.3: Schematic of the experimental setup of Pierce and Rhines (1996). The authors explored the effect of a sloping endwall on the entrainment dynamics of the plume. Dense and fresh water are pumped into the system at equal rates, with volume input compensated by four sinks distributed uniformly along the surface boundary between the sources.

transport in the interior. More precisely, if the average residence time of a parcel of fluid in comparison to the average overturning timescale is large, so that the water recirculates many times before it is replaced, then the source volume flux is expected to have a negligible effect on the flow pattern. Although the experiments of Pierce and Rhines (1996) did not reportedly achieve a stationary state, a full-depth asymmetric circulation below a thin boundary layer was observed, characteristic of that seen in thermally–driven horizontal convection experiments. Experiments by Whitehead and Wang (2008), aimed at exploring the effects of external mechanical forcing on a convective circulation, integrated a spillway into the experimental setup to remedy the obligatory flux of volume into the tank. Because the density of the fluid exiting the tank must be at the mean density of the saline and freshwater sources when the flow has reached a steady state, both of these configurations unavoidably impose constraints on the density field near the sink region.

More recent experimental work by Stewart et al. (2012) examines the overturning circulation maintained by a solutal surface buoyancy forcing in the presence of turbulent mixing. The experimental setup rectifies the issue of imposing a mean density condition at an arbitrary level in the tank by instead imposing a boundary condition of freshwater on the upper surface, which is free to adjust accordingly to the solute–driven

circulation. In steady state, the vertical transport of salt into this freshwater layer must equal that which is introduced into the tank, so that salinity is only constrained at the source and at the surface, where the two must equal. All experiments performed in this work are based on the setup used in Stewart et al. (2012), which is schematized in figure 2.1. It should be noted that this class of experiments deviates from the pure horizontal convection model in that it requires a volume source and corresponding sink in the flow to establish a zero net volume flux, places buoyancy flux constraints, and sets the maximum density in the system. However, experiments show both qualitative and quantitative similarities between solutal surface buoyancy–driven convection and pure horizontal convection models, and therefore prove to be useful in comparing the respective convective circulations, as well as the theoretical predictions of Hughes et al. (2007).

1.2.4 Previous numerical work

The qualitative flow features observed in the thermally–driven experiments of Mullarney et al. (2004) are in agreement with results of 2D numerical work carried out at relatively lower Ra , at most $\mathcal{O}(10^8)$, for which the plume is laminar (e.g. Beardsley and Festa, 1972; Rossby, 1998; Mullarney et al., 2004). Gayen et al. (2012) present three–dimensional (3D) direct numerical simulations (DNS) of horizontal convection for $Ra \approx \mathcal{O}(10^{12})$, forced by heating applied over half of the base and cooling over the other half. The solutions are consistent with the experiments of Mullarney et al. (2004), in that they reveal a turbulent endwall plume as well as the persistence of a CML which supports streamwise roll instability. The authors also show that almost all irreversible mixing at large Ra occurs in the unstable boundary layer.

More recent work by Gayen et al. (2014) explores the flow’s transition to turbulence through DNS and large–eddy simulation (LES) modeling of horizontal convection over a relatively large Ra and Pr parameter space. The authors find that at low Ra ($\sim 10^8$), the thermal boundary layer may be characterized by a balance between viscosity and buoyancy, whereas inertia and buoyancy dominate for flows in which $Ra \geq 10^{11} - 10^{12}$, corresponding with the transition from laminar to turbulent flow.

1.3 The effect of surface stress

Whether surface buoyancy fluxes alone can sustain the MOC and, by extension, the interior ocean stratification, has been a topic of some debate since the work of Sandström (1908). A wide array of literature (e.g. Wunsch and Ferrari, 2004; Johnson et al., 2007) suggests that surface buoyancy forcing, whether through heating and cooling or evaporative and precipitative processes, contributes a negligible amount of energy input into the general circulation. Wunsch and Ferrari (2004) argue that the resupply of potential energy (PE), which is vital in maintaining the abyssal stratification below the thermocline, must come from the conversion of kinetic energy (KE). In horizontal convection, the rate of transformation of PE into KE is directly proportional to the diffusivity, κ , which is taken to be molecular, and consequently very small (Paparella and Young, 2002; Winters and Young, 2009). Paparella and Young (2002) prove mathematically that horizontal convection is non-turbulent in the bulk, and is therefore unable to provide the estimated vertical mixing required to sustain the observed ocean stratification. The only two sources capable of this energy conversion on a large enough scale are the wind stress and tidal flow, and thus it is argued that the circulation must be mechanically controlled (Wunsch and Ferrari, 2004). With regard to wind stress, the winds supply KE by inducing large-scale motion of the water masses, particularly in the Southern Ocean. The resulting divergence of the velocity field generates upwelling from below, tilting isopycnals and thus producing available potential energy (APE) in the system.

More recent work contends that surface buoyancy fluxes should not be dismissed in the energy budget. Hughes et al. (2009) argue that the amount of APE is dynamically more relevant than PE. The APE is defined as the difference between the total PE, and the background potential energy, BPE, of the system. The BPE is defined as,

$$E_b = \int (H - z_*) b \, dV \quad (1.18)$$

where b is the buoyancy, and z_* is the reference height of each parcel of fluid at which it contains a minimum potential energy state (Winters and Young, 2009). Through an energetic analysis, Hughes et al. (2009) show that in steady state, irreversible mixing dissipates APE at the same rate at which it is generated by surface buoyancy forcing. As

APE is also generated by external sources, such as winds and tides, the authors conclude that both the buoyancy flux and wind stress contribute to the overall circulation. More recent numerical work on solely buoyancy–driven convection shows that the total irreversible mixing is exactly equal to the generation of APE through buoyancy forcing, and one order of magnitude larger than viscous dissipation in the system (Scotti and White 2011; Gayen et al. 2012), validating the energy cycle of Hughes et al. (2009). The model output of Gayen et al. (2012) reveals that in an equilibrated flow, the magnitude of the circulation and the rates of APE generation, irreversible mixing, and viscous dissipation all increase with increasing Ra , rather than approach zero (Paparella and Young, 2002).

Other research likewise aims to reconcile the apparent dichotomy between surface buoyancy forcing and mechanical forcing in contributing to the equilibrated circulation by arguing that both participate in maintaining the overturning. Tailleux and Rouleau (2010) suggest that mechanical forcing enhances horizontal convection by increasing the amount of turbulent mixing. Kuhlbrodt et al. (2007) view the coupled system as a pump–and–valve process, where wind–driven upwelling is the pump and surface buoyancy forces are the valve.

There exists some numerical work which investigates the flow resulting from horizontal convection in the presence of an imposed surface stress. Beardsley and Festa (1972) numerically solved horizontal convection forced by a non–uniform temperature difference and an opposing constant stress for $Ra \sim O(10^4)$. The authors reported the development of a two–cell structure in steady state, and observed that for low stresses, work was being done against the system by slowing down the thermal circulation. For higher stresses, thermal circulation ceased to exist so that the stress no longer needed to oppose the convection, consequently increasing KE in the system. Ilicak and Vallis (2012) implemented a non–hydrostatic Boussinesq model, where the stress is achieved via a periodic vorticity field on the surface. In the stressed case, a deep eddying flow is maintained in steady state, with its strength proportional to that of the forcing. The authors find that with increased stress, the thermocline deepens considerably and the maximum streamfunction is increased relative to the zero–stress case.

Hazewinkel et al. (2012) considered a 2D non–rotating Boussinesq fluid subject to a monotonically decreasing surface buoyancy forcing and a sinusoidal surface

stress. The stress drives a circulation in the opposite direction to the clockwise circulation forced by the buoyancy. Numerical simulations up to $Ra \sim 10^8$ reveal the existence of a competitive forcing regime where a two-cell circulation develops: a shallow, mechanically–driven cell, and a deeper, buoyancy–driven cell. The authors assess that in order for the surface stress to be competitive with buoyancy forcing, its magnitude must be comparable to the stress across Rossby’s boundary layer in the purely buoyancy–driven flow (see § 1.2.1),

$$\tau_{max} = \frac{\nu U_s}{\delta_{bl}}, \quad (1.19)$$

where τ_{max} (m^2s^{-2}) is the maximum surface stress, and U_s (m s^{-1}) is the horizontal velocity in the boundary layer. This scaling for the boundary layer thickness may be combined with (1.7) and (1.10) to obtain

$$S_{\delta f} = \frac{\sigma S}{Ra_B^{1/2}} \quad \text{where} \quad S = \frac{\tau_{max} L^2}{\nu^2}. \quad (1.20)$$

The parameter S is a measure of the strength of the surface mechanical forcing, and $S_{\delta f}$ provides a ratio of mechanical to buoyancy forcing; if $S_{\delta f} \gg 1$, one can expect the circulation to be strongly mechanically–forced. If, however, $S_{\delta f} \ll 1$, then the flow is expected to be buoyancy–driven.

In general, there is limited knowledge in regards to the scalings and dynamics that occur for Ra and Ra_B in regimes where the plume is turbulent, which are computationally expensive to simulate, and no experiments have been attempted to examine this coupled system. For this reason, laboratory experiments are implemented in this study to offer insight into the resulting flow structure and stratification expected in a system in which a surface stress is superposed on a buoyancy–driven circulation in the limit where $Ra_B > 10^{12}$.

Table 1.1 is a condensed (non–exhaustive) list of numerical, analytical and experimental work aimed at exploring horizontal convection with and without additional forcing or conditions. While no experimental work exists that explores the equilibrated flow features of a coupled surface stress and buoyancy flux–driven system, there is some literature investigating the effects of mechanical forcing imposed on buoyancy–driven convection (e.g. Whitehead and Wang, 2008; Stewart et al., 2012). The mechanical

Table 1.1: Non-exhaustive list of relevant work pertaining to horizontal convection, sorted by publication year and alphabetically by the first author's last name. E = experimental, N = numerical, A = analytic.

Author & year	Type of work	Forcing	Additional conditions
Sandström (1908)	E	Heat	—
Rossby (1965)	E	Heat	—
Beardsley and Festa (1972)	N	Heat	Surface stress
Killworth and Manins (1980)	A	Heat	—
Pierce and Rhines (1996)	E	Salt	Bottom topography
Pierce and Rhines (1997)	N	Salt	Rotation
Toggweiler and Samuels (1997)	N	Heat	No vertical mixing
Rossby (1998)	N	Heat	—
Vallis (2000)	N & A	Heat	Surface stress, geometry
Paparella and Young (2002)	N	Heat	—
Mullarney et al. (2004)	E & N	Heat	—
Wang and Huang (2005)	E	Heat	Bottom topography
Coman et al. (2006)	E	Heat	—
Hughes and Griffiths (2006)	N	Heat	Sloping boundary
Nycander et al. (2007)	N	Heat	Surface stress
Hughes et al. (2007)	N	Heat	—
Mullarney et al. (2007)	E	Heat	Surface freshwater input
Chiu-Webster et al. (2008)	A	Heat	—
Whitehead and Wang (2008)	E	Salt	Mechanical stirring
Tailleux and Rouleau (2010)	N	Heat	Mechanical stirring
Scotti and White (2011)	N	Heat	—
Hazewinkel et al. (2012)	N	Heat	Surface stress
Ilicak and Vallis (2012)	N	Heat	Surface stress
Stewart et al. (2012)	E	Salt	Mechanical stirring
Barkan et al. (2013)	N	Heat	Rotation
Gayen et al. (2012)	N	Heat	—
Griffiths et al. (2013)	E & N	Heat	Transient adjustment
Gayen et al. (2014)	N	Heat	—
Barkan et al. (2015)	N	Heat	Rotation & surface stress
Vreugdenhil et al. (2015)	E & N	Salt	Mechanical stirring

forcing, supplied in the form of grid mixing, generates small-scale turbulence which is found to deepen the thermocline, thicken the boundary layer, and decrease the overall top-to-bottom density difference in the equilibrated flow.

1.4 Motivation and thesis layout

The present study is inspired by the two dominant drivers of the MOC, and specifically by a desire to better understand the interaction between mechanical and buoyancy forcing simultaneously acting on a system. To this end, a simplified, 2D, non-rotating model of convection maintained by surface buoyancy forcing and surface stress is explored experimentally. In the oceans, a zonal wind stress drives a meridional Ekman flow on account of the earth's rotation. Acknowledging that the full effects of Ekman transport cannot be simulated without including the Coriolis force, only the component of the transport that acts in the same direction as the buoyancy-driven circulation is modeled. Thus, in the experimental setup discussed in chapter 2, a stress is imposed parallel to the north-south buoyancy gradient to simulate convection coupled with mechanical forcing along the surface layer for the cases where the mechanical forcing acts together with, or against, the flow established by the buoyancy flux at the surface.

Chapter 2 discusses the two experimental configurations which have been implemented to gain insight into the coupled mechanical and buoyancy-driven system. The quantitative tools, including the synthetic schlieren technique, conductivity probe measurements, and particle image velocimetry, are explained in detail. A brief overview of preliminary experiments exploring sink location on the resulting buoyancy-driven circulation is also discussed. Chapter 3 reviews the first set of experiments, in which a mechanical forcing in the form of a surface stress is superposed on a buoyancy-driven convective cell, such that both forcings support a flow in the same direction on the upper boundary. Chapter 4 discusses the opposite case, in which the surface stress is competitive with the sense of the buoyancy-driven circulation. Final thoughts as well as a note about potential future work is presented in chapter 5.

Chapter 2

The experiments

The motivation behind this experimental study is to better understand the effects of mechanical and buoyancy forcing acting simultaneously on a non-rotating system. The experimental setup is based on work by Stewart et al. (2012), and is pictured in figure 2.1. A total of 45 experiments are carried out for two dense source configurations, indicated by the dashed lines (red and black) branching from the main saline source tube. The dense water source tubing may be re-positioned to create a line half-plume against either tank endwall, providing the flexibility of establishing a buoyancy flux that sustains a clockwise or anticlockwise convective cell. A layer of freshwater flowing along the upper boundary sets the surface stress on the resulting circulation. The direction of the freshwater flow is always from right to left. Thus, adjustment of the dense source configuration allows the buoyancy forcing to act in opposition to, or in the same direction as, the stress forcing at the surface.

The first 30 experiments use a saline source that enters the working volume on the right-hand side (red dashed line), resulting in a buoyancy-forced clockwise circulation that drives the convection in opposition to the direction of the surface stress. The last 15 experiments are performed with the saline source on the left-hand side of the tank (black dashed line); in this case, the mechanical forcing created by the surface stress acts in the same direction as the counterclockwise overturning circulation driven by the buoyancy flux.

The experiment apparatus is presented in § 2.1, with an appended note in regard to the mechanical forcing in § 2.1.1. A review of experiments designed to investigate

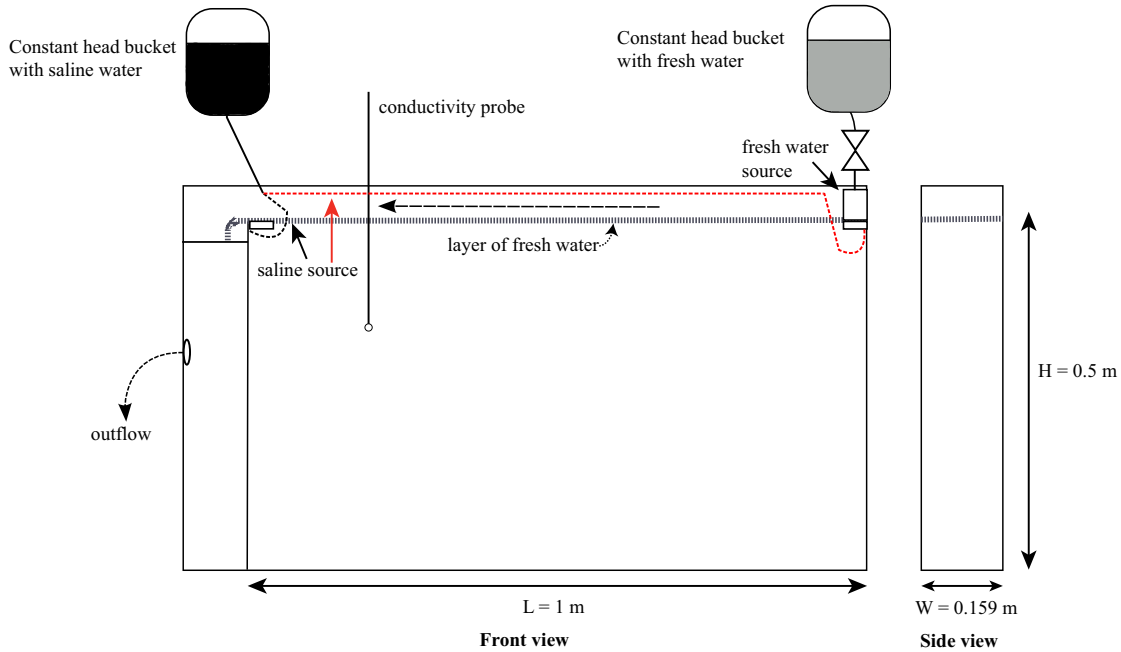


Figure 2.1: Schematic of experimental setup used for all experiments. Dense and fresh water enter the tank from constant head buckets. The freshwater feeds into the tank on the right-hand side, and flows along the surface of the working volume from right to left; its flow rate is adjusted via a needle valve downstream of the constant head bucket. The dense source tubing may be re-positioned to feed dense fluid on either the right-hand or left-hand endwall (tubing configuration indicated with red and black dashed lines, respectively) to create a buoyancy–driven circulation that flows in either the same direction as or opposite to the stress–driven flow at the surface boundary.

the effects of the experiment architecture on the solutal buoyancy–driven circulation is discussed in § 2.1.2. The techniques used to acquire quantitative data of the flow properties for all experiments are described in detail in §§ 2.2 to 2.4. The synthetic schlieren technique (Dalziel et al., 2000) and conductivity probe measurements provide information regarding the structure of the interior vertical density gradient, as well as the boundary–layer thickness. Particle image velocimetry is used to obtain spatially–averaged velocity measurements and related flow properties, including the maximum streamfunction and magnitude of the velocity field. Finally, the procedure for running experiments and data acquisition is discussed in § 2.5.

2.1 Apparatus

An acrylic tank with dimensions $L \times W \times H$ of $1.2 \times 0.159 \times 0.6 \text{ m}^3$ is used for all experiments. In order to maintain a zero net flux of volume, a spillway is integrated on the left-hand side of the tank. The volume in which the experiment takes place is to the right of the vertical partition that separates the spillway from the experiment, setting the aspect ratio to $A = 0.5$, and an adjusted L and H of 1.0 m and 0.5 m, respectively. The overflow ejects into a sump basin, and is pumped into a nearby sink via a sump pump.

Fresh de-ionized water at $\rho_f = 998 \text{ kg m}^{-3}$ plumbed from the filtered main water supply fills a 0.208 m^3 high-density polyethylene (HDPE) drum fitted with a float valve. A water pump (EHEIM model 1262) transports the freshwater into a constant head bucket, from which a portion enters the experiment while the rest recirculates to the drum. The purpose of the constant head bucket is to maintain a gravity-fed, constant flow rate of water into the experiment by setting the height of the water column in the bucket and recirculating the overflow. The freshwater that feeds into the tank flows through Teflon tubing from the constant head bucket into a polystyrene container that is fitted with a porous base, ensuring that the water enters the tank uniformly and with negligible momentum. A Swagelok needle valve (PN SS-4GUF8) is installed downstream of the constant head bucket to allow adjustment of the flow rate of freshwater into the tank. Because bubble formation on the walls of the tubing became a common issue during experiments, two purge lines are installed downstream of the needle valve in order to allow trapped air to escape. The “working volume”, or volume in which the experiment takes place, is defined by the horizontal extent of the tank to the right of the vertical partition and by the vertical distance from below the freshwater surface layer to the base of the tank.

Saline water at a density $\rho_d \approx 1010 - 1030 \text{ kg m}^{-3}$ is housed in a 0.568 m^3 HDPE drum, and is likewise pumped into a constant head bucket before feeding into the experiment tank through a stainless steel tube at a fixed volume flux per unit width of $Q_d = 16.77 \text{ mm}^2 \text{ s}^{-1}$. The salt water is prepared a day before each experiment by mixing de-ionized water and high-grade evaporated salt (Brenntag PN 766002) using an industrial mixer (Mixer Direct PN ECM033EDD-001) until all of the salt has dissolved,

and then allowing it to equilibrate for at least 12 hrs. The tubing is positioned such that the dense water is directed into the bottom corner of an acrylic plate inside the tank, causing the inflow to spread out into a full-width line source with negligible momentum flux. The acrylic plate also prohibits any dense water from escaping into the overflow. The dense water source forms a sinking, fully turbulent endwall half-plume on the right-hand (or left-hand) side of the tank, which gives rise to a buoyancy–driven clockwise (or counterclockwise) circulation. In steady state, the vertical transport of salt out of the tank must equal that which is introduced through the saline source. Thus, the salinity is only constrained at the surface and at the source, where it must equal the input salinity for each experiment.

All experiments are performed in a laboratory with temperature held constant at $22 \pm 1^\circ\text{C}$. To further inhibit temperature fluctuations, the experiment tank sits on 10 cm of polystyrene insulation and is covered with 38 mm of polystyrene insulation on all sides when no data is being recorded, excluding the surface. For flow visualization, potassium permanganate (KMnO_4) is mixed into the drum housing the dense water. To illuminate the flow, four fluorescent tube lamps are mounted behind the tank. A rectangular piece of white polystyrene serves as a uniform backdrop for visualizing the advancement of the plume.

2.1.1 Mechanical forcing

The freshwater layer at the free surface has a two-fold purpose in the experiments. For one, it maintains an upper boundary condition of constant density. During each experiment, the vertical volume flux of freshwater into the working volume, which lies below this upper freshwater boundary, is free to adjust as required to maintain a steady-state convection. The advantage of using the current method for maintaining a zero net volume flux is that it eliminates the question of where to place a sink in the experiment, which would constrain the density of fluid near it to necessarily be at the mean density of the input sources in a steady-state flow, as discussed in §§ 1.2.3 and 2.1.2. Rather, in the current setup, the freshwater layer takes on the role of a surface boundary condition.

The second purpose of the freshwater layer is to impose a surface stress on the

underlying buoyancy–driven circulation. The freshwater flow rate per unit spanwise width, Q_f , is regulated via a needle valve in order to vary the magnitude of shear stress on the surface of the working volume by increasing or decreasing the input volumetric flow rate. The direction of the resulting stress is fixed, and directed from right to left, for all experiments. It is worth noting that creating a surface stress by using a constant throughput of freshwater permits interfacial instabilities to form, ultimately allowing the freshwater layer to partake in the circulation. This flow is expected to be unlike one which is forced purely by a surface stress generated by a conveyor belt, for example, which would not introduce excess buoyancy into the volume.

2.1.2 The effect of sink location

In order to better understand the effect of sink location on a solutal buoyancy–driven circulation, preliminary experiments were performed in which the sink location was varied between three different positions for two aspect ratios, $A = 0.08$ and $A = 1$. The general setup mimics that of Pierce and Rhines (1996), and is schematized in figure 2.2. Saline water at $\rho_d = 1035 \text{ kg m}^{-3}$ is prepared in a large tank and set out to degas and equilibrate to room temperature overnight. The dense and freshwater sources are placed in the left and right corners of the tank, respectively. Both sources are constructed of plastic tubing that spans the width of the tank, each containing a row of small perforations to force the fluid to enter uniformly in the spanwise direction. The sources are wrapped in porous material in order to minimize vertical momentum upon entering the experiment. The sinks are placed midway between the two sources, at the surface, middle, and bottom of the tank, with sink depth varying per experiment. All sources and sinks are controlled via a Watson Marlow peristaltic pump (Model 505U).

Potassium permanganate (KMnO_4) is used as a proxy for salt (4 g KMnO_4 per 100 mol NaCl). In order to calibrate the dye concentration with light attenuation, measured amounts of KMnO_4 are mixed into a known volume of water in the tank until a homogeneous color is achieved. The tank is illuminated from behind with an electroluminescent light sheet, and 5 s of images at 12Hz are recorded with a JAI 1.4 MP progressive scan CCD camera (model CV–M4⁺CL). The image set is averaged, and the mean intensity within the tank region is quantified using DigiFlow software (Dalziel

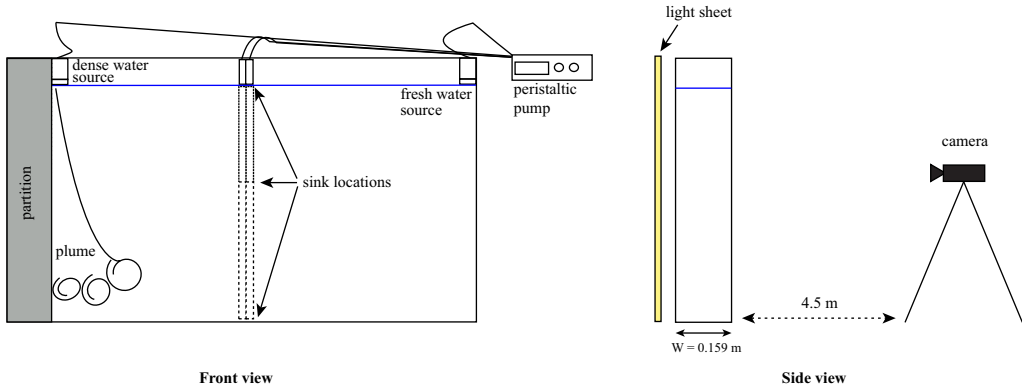


Figure 2.2: Schematic of experimental setup to investigate the effect of sink location on a solutal buoyancy–driven circulation. A watertight acrylic partition is used to adjust the aspect ratio of the volume. Dense and fresh water are fed via a peristaltic pump into perforated plastic tubing spanning the tank width. Water is removed at the same rate as it is supplied through two small tubes, with sink location varying between experiments. The sinks are always placed together in the center of the tank, at either the bottom, middle, or surface of the volume. The equilibrated density field is recovered from recorded images of dye concentration, which serves as a proxy for salt.

Research Partners, 2008). A calibration curve such as the one shown in figure 2.3 is constructed by repeating this procedure for increasing dye concentrations.

The experiments are initialized with clear freshwater in the tank, and the saline source is dyed to a known concentration. An equilibrated state is determined to be reached when the outflow density is equal to the average density input into the tank, such that there is zero net flux of salt in the system. Discrete samples of outflow density are measured using an Anton Paar DMA5000 density meter, accurate to 0.005 kg m^{-3} , in order to track the evolution to equilibrium. Once this state is reached, dye images are recorded and subsequently converted into density values by recovering the dye concentration required to achieve the recorded intensity; this value is then used to calculate the density at any given pixel by noting that the maximum source density corresponds to the maximum dye concentration and freshwater corresponds to no dye. In general terms, if the maximum density is $\rho_d \text{ kg m}^{-3}$ for a volume of $V \text{ m}^3$, the required amount of salt is found from a MATLAB script relating density and mass of salt, and equal to $X_{NaCl} \text{ g}$

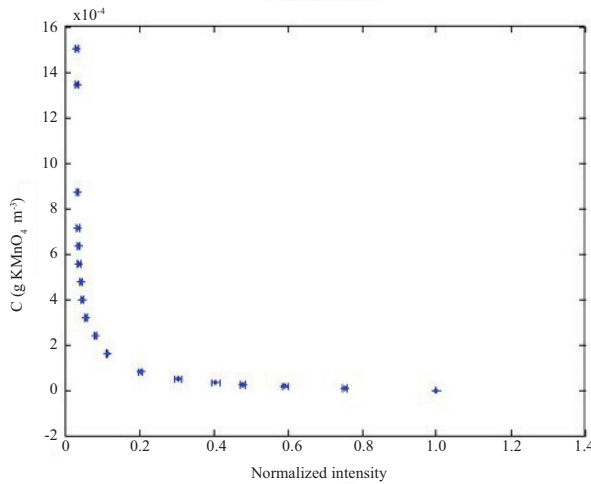


Figure 2.3: Calibration curve used to recover the spatially-averaged (in the spanwise direction) density field. A normalized intensity of 0 corresponds to black, and 1 corresponds to a saturated image. It is desirable to remain in the linear section of the curve ($\sim 0.2 - 1.0$), where a small change in intensity will not yield high uncertainty in the dye concentration.

NaCl . This is converted to dye concentration using

$$\frac{X_{\text{KMnO}_4} \text{ g } \text{KMnO}_4}{V \text{ m}^3} = X_{\text{NaCl}} \text{ g } \text{NaCl} \times \frac{1 \text{ mol NaCl}}{58.443 \text{ g NaCl}} \times \frac{4 \text{ g } \text{KMnO}_4}{100 \text{ mol NaCl}}. \quad (2.1)$$

Therefore, X_{KMnO_4} g of KMnO_4 are added to the fluid of volume V , with the resulting concentration corresponding to a density of $\rho_d \text{ kg m}^{-3}$. Once the intensity map is recorded for an experiment, the corresponding concentration of KMnO_4 is found from the calibration curve to be $C_{(i,j)\text{KMnO}_4}$, and the density $\rho_{i,j}$ at each pixel point (i, j) is then recovered through the relation,

$$\frac{X_{\text{KMnO}_4} \text{ g } \text{KMnO}_4}{\rho_d \text{ kg m}^{-3}} = \frac{C_{(i,j)\text{KMnO}_4} \text{ g m}^{-3} \text{ KMnO}_4 \times V \text{ m}^3}{\rho_{(i,j)} \text{ kg m}^{-3}}. \quad (2.2)$$

Figures 2.4 and 2.5 display a sample of the steady-state density field perturbations from the mean density ($\approx 1017 \text{ kg m}^{-3}$) for the two aspect ratios considered.

At either aspect ratio, it is clear that the resulting stratification is significantly affected by the sink location. By definition, when the system is in steady state, the average salinity of the fluid pumped out of the tank is equal to the average salinity of the fluid pumped into it, so that the density of the water at the sink location is automatically

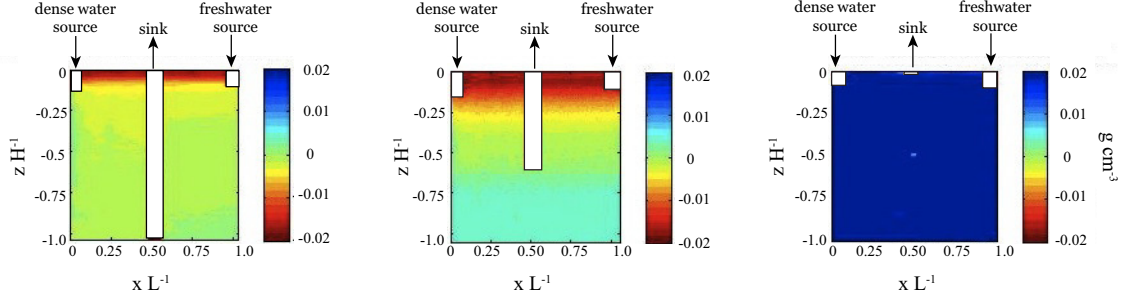


Figure 2.4: Steady-state maps of the density perturbation for $A = 1$. For each experiment, the tank is initially filled with freshwater, and the saline source density is $\rho_d = 1035 \text{ kg m}^{-3}$. The saline and freshwater sources are located on the surface in the left and right corners of the tank, respectively. The sink is located in the center of the volume, at the bottom, middle, and surface of the tank (from left to right) for each experiment. The sink and sources have been digitally masked out with white rectangular overlays.

set to be at the mean density; this introduces a spurious condition at the sink location. In the cases where the sink is located in the middle and at the bottom of the domain, a boundary layer develops at the surface. When the sink location is at the surface, as in Pierce and Rhines (1996), the boundary-layer thickness is set by the penetration depth of the sink rather than the dynamics of the circulation. Moreover, the sink preferentially removes freshwater in this configuration, which naturally flows along the surface and thus remains in the vicinity of the sink. The setup is therefore forcing the saline and freshwater sources to contribute unequal amounts to the circulation via this artificial condition. In all experiments, the boundary-layer thickness does not seem to be set by the diffusive–buoyant balance in the boundary layer, but rather by the external location of the sinks.

Furthermore, because the interior density structure is altered for different sink configurations, the plume penetration depth, specific buoyancy flux, and maximum streamfunction, among other key characteristics of the flow, are likewise set externally. As an example, in the case where the sink is at the bottom of the domain, the fluid surrounding it must be at the mean density in steady state. Since the stratification is preferentially stable (there are no other mechanisms acting on the system which may

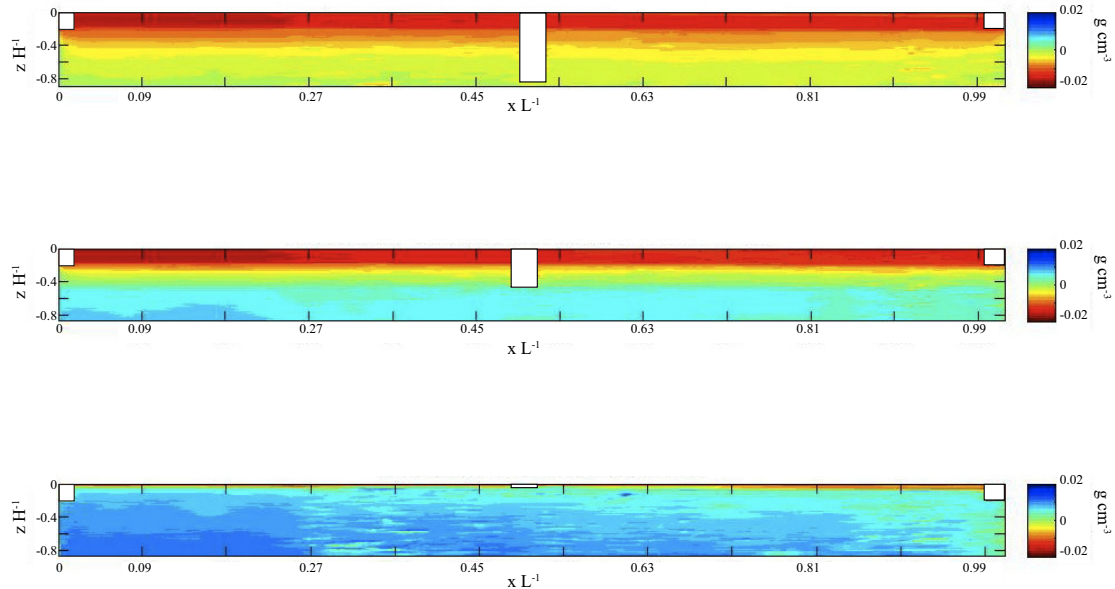


Figure 2.5: Steady-state maps of the density perturbation for $A = 0.08$. For each experiment, the tank is initially filled with freshwater, and the saline source density is $\rho_d = 1035 \text{ kg m}^{-3}$. The saline and freshwater sources are located on the surface in the left and right corners of the tank, respectively. The sink is located in the center of the volume, at the bottom, middle, and surface of the tank (from top to bottom) for each experiment. The sink and sources have been digitally masked out with white rectangular overlays.

lead one to believe otherwise), the densest water in the interior is located at the bottom of the domain, with its density at the mean density of the sources. Therefore, the dense line half-plume is perpetually entering a relatively fresher environment, consequently always sinking to the base, and its specific buoyancy flux never tending to zero. This result is very much at odds with the theory of Hughes et al. (2007), as well as horizontal convection experiments in which the circulation is forced either by differential heating or a solutal buoyancy flux imposed on a boundary (Mullarney et al., 2004; Stewart et al., 2012).

This set of preliminary experiments exploring variable sink location verifies that sink position is indeed important when considering a solute-driven circulation, and a

more accurate experimental setup is necessary in order to capture the true qualitative and quantitative features of horizontal convection. Specifically, a setup is desired in which diffusion, rather than a forced sink condition, acts as the transporter of salt out of the system to maintain zero net buoyancy flux, such as the configuration of Stewart et al. (2012).

2.2 Synthetic schlieren (SS)

The synthetic schlieren (SS) technique obtains a visualization of the established density perturbations, as well as spatially-averaged quantitative whole-field density maps (Dalziel et al., 2000). Synthetic schlieren makes use of the bending of light rays as they pass through a density stratification, in conjunction with the one-to-one relationship between refractive index and density fluctuations. In fact, for salt water, the relationship between the density and refractive index is approximately linear, and given by,

$$\nabla n = \frac{dn}{d\rho} \nabla \rho = \beta \frac{n_0}{\rho_0} \nabla \rho, \quad \text{with } \beta = \frac{\rho_0}{n_0} \frac{dn}{d\rho} \approx 0.184, \quad (2.3)$$

where n is the refractive index, n_0 is the nominal refractive index of the medium ($n_0 = 1.3332$ for water), and ρ_0 is the nominal reference density, taken to be 1000 kg m^{-3} in the synthetic schlieren algorithm. The most advanced of the synthetic schlieren algorithms is pattern matching refractometry, which has its roots in particle image velocimetry. The method involves an illuminated mask with a strong pattern of randomly spaced dots placed behind the experiment. Once a flow is introduced into the experiment, any change in the density structure manifests itself as an apparent shift in the location of the dots on the textured mask, due to the bending of light rays by refractive index perturbations. These variations in the refractive index field, as observed by the camera, are measured relative to a background image taken before any density anomalies are introduced into the tank. In terms of experiment coordinates, the apparent displacements of the dots relative to the background image are

$$\Delta\xi = -\frac{1}{2}W \left(W + 2\frac{n_0}{n_{air}}B_l + 2\frac{n_0}{n_{wall}}T \right) \frac{\beta}{\rho_0} \frac{\partial \rho'}{\partial x}, \quad (2.4)$$

$$\Delta\zeta = -\frac{1}{2}W \left(W + 2\frac{n_0}{n_{air}}B_l + 2\frac{n_0}{n_{wall}}T \right) \frac{\beta}{\rho_0} \frac{\partial\rho'}{\partial z}, \quad (2.5)$$

where W is the tank width, B_l is the distance from the mask to the outside tank wall, T is the tank wall thickness, and ρ' are the density fluctuations within the fluid. In this formulation, x is the direction along the tank, and z is the vertical direction. It should be noted that the displacements $\Delta\xi$ and $\Delta\zeta$ are relative to the *world* coordinates of the mask, where the coordinate system is generally defined at the mid-plane of the experiment. The above displacements are relevant for a *thin* experiment, i.e. $WL_m^{-1} \ll 1$, where L_m is the distance between the textured mask and the camera; in all performed experiments, $WL_m^{-1} = 0.035 \ll 1$, and thus the thin approximation is valid. Once the apparent displacements are recorded, (2.4) and (2.5) may be inverted to determine the perturbation density gradient, and subsequently integrated to recover the density perturbation field. Spatial averaging over 15×15 pixels² is inevitable because the technique relies on “interrogation windows” of a specified pixel area. The pattern within a given interrogation window is optimally matched between the current and background images using cross-correlation functions that optimize the intensity mapping between the frames. Each interrogation window results in a displacement vector which is converted to a density gradient through (2.4)–(2.5).

2.2.1 Setup

A mask consisting of a random distribution of dots is generated using the Post-Script file provided in the DigiFlow User Guide (Dalziel Research Partners, 2008). The mask should be locally unique, and is thus created by randomly perturbing a regular grid of dots of a specified size. The mean spacing between the dot centers is set to 2 mm, with a relative size of the dots to their mean spacing as 0.25, and a scale for randomness of 0.6. The resulting mask contains a random array of white dots with diameter 1 mm on a black background. When determining dot size, the general guideline is one to two pixels per dot, or close to the limit of the camera resolution. The pattern is printed on multiple transparency sheets, and three sheets are overlaid and glued together using photo mount spray adhesive. Tiling of the transparency sheets ensures a high contrast between the black dots and bright background light. The transparencies are taped onto

an $172.72 \times 60.96 \text{ cm}^2$ electroluminescent light sheet (Electric Vinyl, Inc.), which is sandwiched between a wooden frame and a perspex sheet. The mask is displaced 58.42 cm behind the tank. Because the method is very sensitive to thermal noise, black tarp runs from the experiment tank to the camera in order to block out convection induced by laboratory vents and the heat generated from the PC. A photograph of the setup is shown

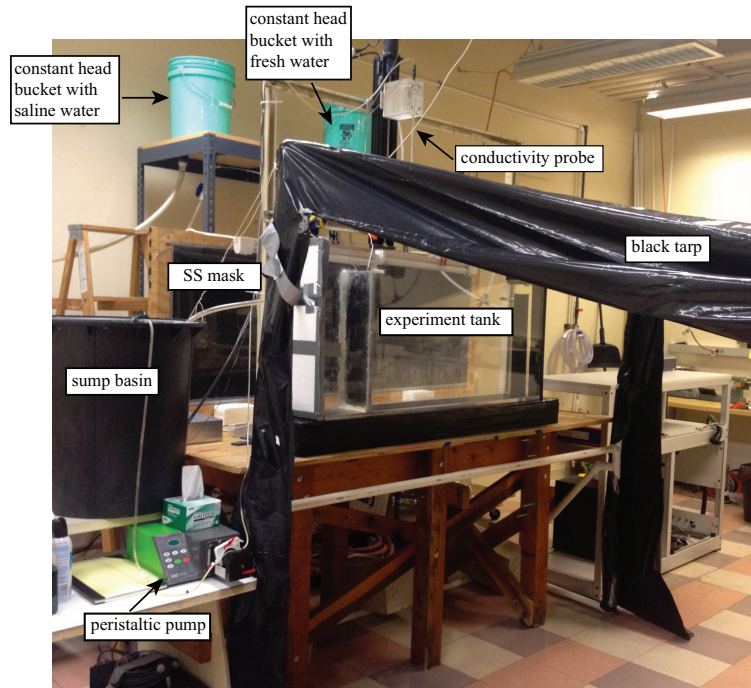


Figure 2.6: Photograph of the synthetic schlieren setup. The SS mask sits 58.42 cm behind the tank wall, housed between a wooden frame and a perspex sheet. During data collection, the laboratory lights are turned off and the electroluminescent light sheet behind the mask is switched on, creating a high contrast between the black pattern and bright light. The black tarp is unfolded, so that the distance from the tank to the camera is isolated on all sides from any convection in the environment. The thermal noise in the laboratory is particularly problematic close to the camera, where sensitivity is the highest (Dalziel et al., 2000).

in figure 2.6, with relevant experimental components labeled. The camera (not shown) is located 405.45 cm from the front of the tank in order to reduce parallax. Images are recorded using a JAI 1.4 MP progressive scan CCD camera (model CV-M4⁺CL) fitted with an Edmund Optics 6X manual zoom video lens, 12.5–75 mm FL and f/1.2–16C (PN 53–153). The images are captured with a frame grabber card (BitFlow R3-PCI-

CL13) and processed using DigiFlow software.

2.2.2 DigiFlow processing

The DigiFlow *Pattern Matching* dialog is utilized to process synthetic schlieren images. In general, the DigiFlow 2014a algorithm is selected, with both resolution and accuracy set to *Best*. The fluid medium is specified as *Water_Salt*, the tank wall as *Acrylic*, and the flow geometry *3D*. The coordinate system is defined at the front of the tank, a valid approximation in the limit $WB_l^{-1} \ll 1$; in the current setup, $WB_l^{-1} = 0.29$ (Dalziel Research Partners, 2008). The required input lengths are as follows: camera to texture, 483.08 cm; experiment to texture, 57.15 cm; experiment thickness, 16.83 cm; wall thickness, 1.83 cm.

In order to estimate the error associated with synthetic schlieren image processing, a range of input parameters was explored. The control case *A* provides the default parameter settings; successive cases hold all parameters constant except those specified in table 2.1. The maximum pixel displacements, *xmaxshift* and *yminshift*, in both the *x*- and *y*-direction are set to 30 in *Case A*. These values represent the maximum apparent displacement in the mask between the background and experiment images. The discard limit, set to 0.4, is responsible for setting the relative size of the mismatch above which a pixel will be removed on account of the pattern not being resolved; the smaller the value, the more pixels are discarded. The interrogation window is 15×15 pixels²; increasing the size of this region increases accuracy, but at the expense of both the spatial resolution and computation speed. Generally, the interrogation window is free to adjust automatically in order to produce more reliable data. The interrogation window size is linked to the *x*- and *y*-spacing subgroup, which controls the spacing between the points where pattern matching takes place. The normalized absolute difference measure is minimized to search for the apparent shift; this function is defined as

$$f = \frac{|A_i - B_i|}{\sqrt{(\sum |A_i|)(\sum |B_i|)}}, \quad (2.6)$$

where A_i and B_i refer to the background and current image, respectively. In order to improve this estimate, a *square* peak fitting transform is employed, which transforms the absolute difference measure f prior to performing a bi-quadratic least squares pro-

cedure. The pattern matching algorithm also offers minimization of a square, power, or correlation function, as specified in the User Guide (Dalziel Research Partners, 2008). In order to improve accuracy and resolution, 4 levels of sub-pixel treatment with a cubic fit are used, and data points are interpolated with a cubic function. Distorted passes improve the accuracy for small interrogation window spacing by utilizing DigiFlow's image distortion technology in order to enhance the spatial resolution. Reverse passes likewise increase accuracy and resolution. A summary of all DigiFlow realizations and corresponding parameter changes are given in table 2.1.

Table 2.1: Varying input parameters for synthetic schlieren processing. X/Y MS refers to the X/Y max shift, DL is the discard limit, SP is the sub-pixel pass, DP is the distorted pass, RP is reverse pass, and IW is interrogation window size; all numeric quantities are in pixel units. IF refers to the function used to interpolate fields, and PFT is the peak fitting transform.

Case	X/Y MS	X/Y space	DL	SP	DP	RP	IW	IF	PFT
A	30	8	0.4	4	6	None	[15,15]	Cubic	Square
B	50	8	0.4	4	6	None	[15,15]	Cubic	Square
C	50	8	0.6	4	6	None	[15,15]	Cubic	Square
D	30	8	0.4	2	3	None	[15,15]	Cubic	Square
E	30	8	0.4	4	6	None	[30,30]	Cubic	Square
F	30	8	0.4	4	6	1	[15,15]	Cubic	Square
G	30	8	0.4	4	6	None	[15,15]	B-spline	Square
H	30	16	0.4	4	6	None	[15,15]	Cubic	Square
I	30	8	0.4	4	6	None	[15,15]	Cubic	Log
J	5	8	0.4	4	6	None	[15,15]	Cubic	Square

Running synthetic schlieren processing for various parameter ranges not only provides an estimate of the error, but also some insight into the sensitivity of the solution to parameter modifications. The x - and y -gradient of the density field are saved for each parameter space, along with a quality file that provides information about the state of the pattern matching. Because DigiFlow finds the constant of integration for the density perturbation field by forcing the spatial mean density perturbation to vanish, which is not valid for these experiments, a MATLAB algorithm is attempted to calculate the whole-field density perturbations. An average x - and y -gradient image is obtained by calculating the arithmetic mean of the case outputs given in table 2.1 for each frame, and an estimate of the error is obtained from the standard deviation.

2.2.3 MATLAB processing

A weighted least squares method is attempted in order to calculate the spatially-averaged density field. The known values include $\partial\rho'/\partial x$ and $\partial\rho'/\partial z$ at each resolved point in the tank, as well as the density values measured by the conductivity probe (see §2.3), rendering the system overdetermined. The input gradient images are a result of averaging 10 DigiFlow synthetic schlieren realizations discussed in §2.2.2, from which the standard deviation is also calculated. A vector of coordinate locations of the conductivity probe for each experiment determines which column of the data matrix will correspond to the known density values. The known density values are converted into perturbation densities to coincide with the gradient inputs,

$$\rho' = \rho_{probe} - \rho_{base}, \quad (2.7)$$

where ρ_{base} is the density of freshwater, 998.23 kg m^{-3} .

The least squares method may be used to solve the general equation

$$\mathbf{E}\mathbf{x} = \mathbf{y}, \quad (2.8)$$

where \mathbf{x} is the parameter of interest, namely the density at each resolved point in the tank, \mathbf{y} is the vector of knowns, comprised of the density gradient fields as well as the conductivity profile densities, and \mathbf{E} is a sparse matrix with appropriate coefficients that make use of finite difference methods to estimate the density values from the input derivatives.

The derivative of the density at row index i with grid spacing Δx using finite difference methods is defined as,

$$\begin{aligned} \text{Central : } & \left(\frac{\partial \rho'}{\partial x} \right)_i = \frac{\rho'_{i+1} - \rho'_{i-1}}{2\Delta x}, \\ \text{Forward : } & \left(\frac{\partial \rho'}{\partial x} \right)_i = \frac{-3\rho'_i + 4\rho'_{i+1} - \rho'_{i+2}}{2\Delta x}, \\ \text{Backward : } & \left(\frac{\partial \rho'}{\partial x} \right)_i = \frac{\rho'_{i-2} - 4\rho'_{i-1} + 3\rho'_i}{2\Delta x}. \end{aligned} \quad (2.9)$$

The truncation error of these finite difference approximations is $\mathcal{O}(\Delta x^2)$. The forward and backward difference methods are used for the first matrix column and last matrix column, respectively, and all other derivatives are estimated with the central difference method. This technique is extended to estimate density derivatives in the z -direction. A diagonal weight matrix is built from an estimate of the conductivity probe's density output errors, as well as the standard deviation values resulting from averaging 10 DigiFlow realizations. The weight matrix \mathbf{w} is comprised of the reciprocal of the variance for each measurement,

$$\mathbf{w} = \frac{1}{\sigma_i^2}. \quad (2.10)$$

Incorporating \mathbf{w} into the original system given in (2.8), the equation to solve becomes

$$\mathbf{E}'^T \mathbf{E}' \mathbf{x} = \mathbf{E}'^T \mathbf{y}', \quad (2.11)$$

where $\mathbf{E}' = \mathbf{w}\mathbf{E}$ and $\mathbf{y}' = \mathbf{w}\mathbf{y}$, and the superscript T denotes the transpose of the matrix. The system is solved for \mathbf{x} by taking the inverse of $\mathbf{E}'^T \mathbf{E}'$,

$$\mathbf{x} = (\mathbf{E}'^T \mathbf{E}')^{-1} \mathbf{E}'^T \mathbf{y}'. \quad (2.12)$$

In MATLAB, this is done using the iterative generalized minimum residual method, *GMRES*. An incomplete LU factorization is used as a preconditioner for the solver in an attempt to decrease the condition number of the matrix.

Unfortunately, the system is extremely sensitive to any turbulence in the flow, and consequently most of the resulting density fields contained unrealistic density values in spite of the inclusion of spatial variance. Consequently, only the vertical density gradient obtained from averaging 10 DigiFlow realizations (see § 2.2.2) is used for subsequent analyses, noting that because the background density field is a constant value of $\rho_{base} = \rho_f$, the density perturbation gradient output of DigiFlow is simply equal to the density gradient,

$$\frac{\partial \rho}{\partial z} = \frac{\partial \rho'}{\partial z} + \frac{\partial \rho_{base}}{\partial z} = \frac{\partial \rho'}{\partial z}. \quad (2.13)$$

Once again, on account of the existing turbulent regions in the flow field, a mean interior vertical density gradient is calculated for all experiments by only considering the interior of the tank, outside any patches of mixing. The resulting density gradient is matched by that obtained from the conductivity probe measurement to correct for any constant

shifts induced by exterior factors, such as the light sheet's intensity fluctuations, as one example.

2.3 Conductivity probe

The density profile of the thin boundary layer at the surface cannot be resolved using the current synthetic schlieren setup because of poor resolution in regions of high density gradients. Therefore, in order to resolve the thin upper boundary layer, a conductivity probe was installed at $L_c = 27.62$ cm from the left-hand side of the tank, and at $D_c = 4.79$ cm from the front of the tank. The probe was designed and constructed at the Department of Applied Mathematics and Theoretical Physics (DAMTP) at the University of Cambridge.

Because salt ionizes in water, it is possible to quantify the mixture's conductivity, which is directly related to the concentration of salt. The conductivity of an electrolytic solution may be determined by measuring the AC resistance of the fluid between two electrodes. For this specific probe, the fluid is siphoned through an inner tube, and the resistance comes from the pinhole in the nylon tip of the probe (Kanda, 2002). The conductivity meter then converts the probe resistance into a DC voltage, which may be transformed into a density value. The response time of the probe is < 200 ms, with an output resolution of approximately 4 mV, requiring a 12 bit A/D converter. Further information in regards to the probe and its internal Cambridge circuit design may be found in Kanda (2002).

2.3.1 Probe traverse

The conductivity probe is mounted on a Velmex Inc. BiSlide positioning slide, measuring 10 threads in $^{-1}$ (<http://www.velmex.com>). A Velmex VP9000 controller (SN 0599382) regulates a Warner Electric Slo-Syn stepping motor (Model M062-LS-550) capable of moving 200 steps rev $^{-1}$. The step resolution of the motor is 2.5×10^{-4} in step $^{-1}$. The VP9000 controller communicates with a PC through an RS-232 serial port, with required settings of 9600 baud rate, 7 data, 2 stop bits, even parity, and no flow control. The VP9000 is remotely controlled by sending commands (ASCII characters)

through the RS–232 interface, which have been integrated into a LabVIEW code (National Instruments). A list of available commands may be found in the VP9000 Series User’s Guide (Velmex Inc., 1996).

2.3.2 Data acquisition

In order to acquire a voltage signal from the conductivity probe, a small volume of fluid must be continuously siphoned through the inner tube. During data acquisition, pumping is achieved with a Watson Marlow peristaltic pump (Model 505U). The pumping rate is set to 10 RPM, or approximately $2.18 \text{ mm}^3 \text{ s}^{-1}$, a flow rate small enough to have no apparent effect on the dynamics of the circulation. The output DC voltage of the conductivity meter is transferred to a National Instruments myDAQ device (SN 173D1D9). The output signal feeds into the analog input channels of the instrument, with a range of $\pm 10 \text{ V}$. The ADC resolution is 16 bits with a maximum sampling rate of 200 kS s^{-1} (kilo-sample s^{-1}) (National Instruments Inc., 2011). The LabVIEW subroutine *Control Main.vi* is used to traverse the conductivity probe through the boundary layer and intermittently collect data points. The control panel of the program is shown in figure 2.7. The *Init* button puts the VP9000 on-line, and initializes the motor settings. The *Calibrate (Pre)* button redirects to *Probe_poly_calib.vi*, the program responsible for obtaining the relation between density and voltage. Once the calibration has been carried out, the probe is ready to traverse the tank depth. The *Home* button positions the probe immediately above the surface of the water. The motor speed and desired position may be specified in distance units of steps, with corresponding speed and depth displayed in mm. The motor is set into motion by pressing the *Move* button.

The script traverses the probe to a specified depth at an approximate speed of 0.10 mm s^{-1} . The maximum depth that the probe is able to penetrate the flow is approximately 23 cm from the surface; thus, almost half of the depth may be profiled. The motor is programmed to move 16 steps, or 0.1016 mm, then echo its position to the host, which is stored into an array. At each 0.1016 mm interval, 4k points are sampled at 10 kHz. If the current depth < specified depth, the script will signal the motor to move and repeat the cycle of data collection. Once the specified depth is reached, the probe position and corresponding voltage output arrays are saved in a .csv file. The panel displays

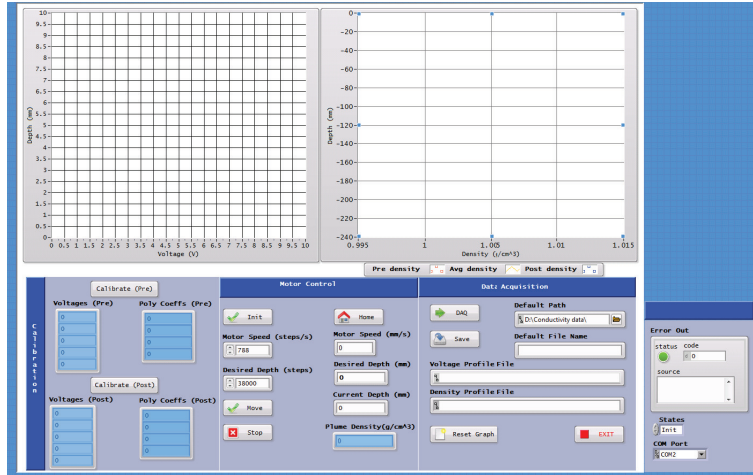


Figure 2.7: A snapshot of the LabVIEW Main Control panel used to traverse the conductivity probe, which integrates a calibration scheme into the data acquisition. The panel plots the conductivity probe’s voltage output as a function of depth in real time. After the profile has been recorded and both calibrations performed, the panel also displays three output density profiles, using each calibration as well as the average of the two. This is done to ensure that there is no significant discrepancy between the calibrations taken before and after the probe traversal. Typically, the curves lay on top of each other, and the average of the two is used in subsequent analyses.

a real-time graph of the depth vs. voltage output data. Once a post-run calibration curve is obtained, the panel also displays three depth vs. density profiles, in which the first calibration fit, the second calibration fit, and a mean of the two, are used to obtain the density profiles. In general, the average of the two calibration curves is stored into an array for later use. The resulting voltage and density profiles are saved within the path *D:\Conductivity data\profiles* under a specified file name, which automatically appends the current date and time. The probe travels back to the surface at 5 mm s^{-1} so as not to introduce any spurious fluctuations into the flow field.

2.3.3 Calibration

In order to convert the voltage outputs into density values, a third-order polynomial fit is obtained from two separate calibrations, taken before and after the conductivity probe has finished profiling. The choice for a third-order polynomial fit was motivated by the fact that it is used in the conductivity-density calibration in the probe

manual (Kanda, 2002), and affirmed by the fact that it consistently yielded R^2 values of ≥ 0.99 .

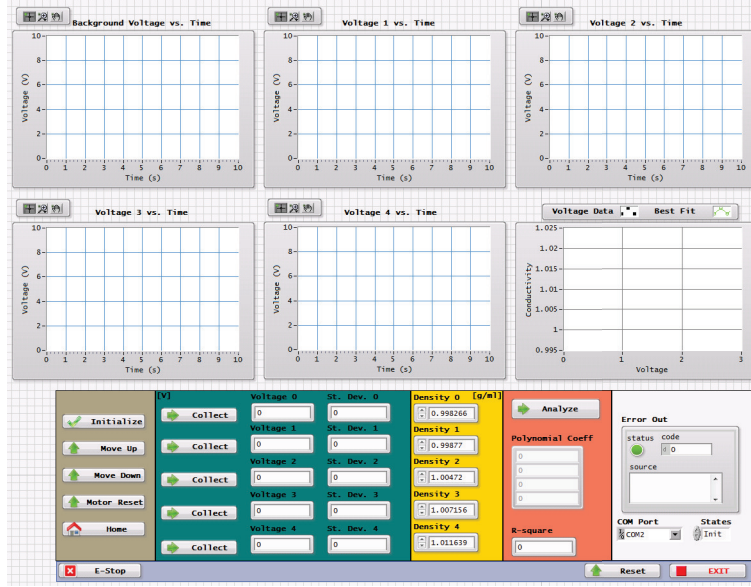


Figure 2.8: A snapshot of the LabVIEW Calibration panel used to calibrate the conductivity probe. The density of five standards are measured and inputted into the program manually. The voltage output of each standard is collected by averaging 4 k points at 10 kHz for 24 s, with real time voltage readings shown in the corresponding plot window. After all five voltage values of the standards are recovered, a third-order polynomial is fit to the data, with relevant values displayed on the panel.

The calibration functions are determined by measuring the voltage output and density of five standard solutions and fitting a curve to this data set. The densities of the standards are chosen such that the first standard is freshwater, the last standard is slightly more dense than the densest water in the experiment, and the middle three standards fall within the intermediate range of freshwater and the densest standard. This ensures that the conductivity probe has been calibrated for the full density range that is expected in the experiment, allowing interpolation of all possible density values. The density of each standard is measured with an Anton Paar DMA5000 density meter, accurate to 0.005 kg m^{-3} , which has previously been calibrated with ultra pure water liquid density standard (SN 05/2012), as per the instruction handbook (Anton Paar GmbH, 2002). The density meter output for the standard with a specified density of $998.20 \pm 0.02 \text{ kg m}^{-3}$

at 20 °C was measured to be 998.205 kg m⁻³, which is within the published accuracy of the instrument (calibrated on 25 Oct 2013, 10:45 AM).

The measured density values are plotted against the measured voltage outputs of the five standards. The LabVIEW code used for calibration is *Probe_poly_calib.vi*, as depicted in figure 2.8. The script's basic function is to obtain an average voltage reading per standard solution, and subsequently fit a curve to obtain the density as a function of voltage. Each voltage value is acquired by sampling 4k points at 10 kHz for 24 seconds, and outputting the mean value as well as the standard deviation. The standard deviation tends to be within the expected range of ±4 mV (Kanda, 2002). Once all five standards have been measured along with their densities and corresponding output voltages, the data set is fitted to a third-order polynomial using the method of least squares and SVG algorithm built into LabVIEW. Pre- and post- calibration ensures that there is no significant electrical drift during the 38 min that it takes for the probe to reach its maximum depth in the tank. Generally, both curves tend to overlay, and an average of the two curves is used for the final density profile.

2.3.4 Adjustment for temperature variation

The enthalpy of solution for NaCl in water is +3.88 kJ mol⁻¹ at STP (Parker, 1965), and therefore the process of dissolving the salt should necessitate the absorption of heat from the surroundings. Temperature data from experiments shows that there exists a modest temperature gradient in the tank, either on account of the solute dissolution, or because of ambient conditions. Regardless, the conductivity, being sensitive to temperature, is calibrated to take into consideration any temperature fluctuations. To this end, seven beakers are filled with 500 ml of water at varying densities. A Type-K thermocouple is inserted into the center of the beaker at mid-depth, and situated next to the conductivity probe. Each individual beaker is placed on a Thermo Scientific heat plate, and temperature and corresponding conductivity are recorded for the range of 21–28°C. The data points for seven density values are plotted in figure 2.9, and verify that there exists a positive linear relationship between the conductivity probe output and water temperature. Moreover, the slope of this line is a function of density, as evidenced in figure 2.10. Therefore, as the density of water is increased, the response of the con-

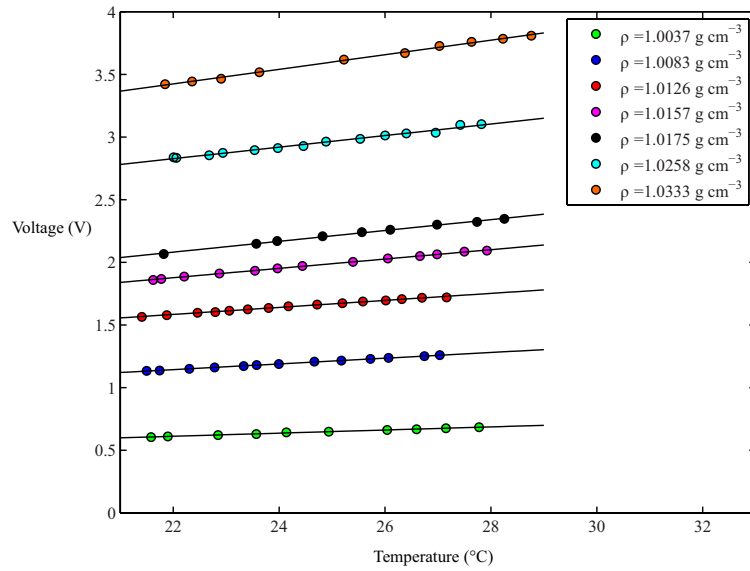


Figure 2.9: Plot of voltage output from conductivity probe vs. temperature for seven densities. The voltage output linearly increases with increasing fluid temperature. The rate of voltage increase as a function of temperature is also a function of the density of the fluid.

ductivity probe output to the water temperature is amplified. The calibration for water temperature must then take into account the density of the fluid in the experiment. This is done by finding the corresponding voltage vs. temperature slope based on the initial dense source density. For each experiment, a linear temperature profile in the tank is assumed from two temperature data points that are continuously recorded at the water surface and the tank base (see §2.3.5). The raw voltage data of the conductivity probe output is shifted according to the drift created by this spatial temperature variation, and thereafter converted into a density profile to be used in subsequent analyses.

2.3.5 Thermocouple measurement

In order to ensure that each experiment is not significantly affected by temperature anomalies in the fluid, two Type-K thermocouples are placed inside the tank (Omega Inc., Model: TT-K-30-SLE). The first thermocouple is located in the bottom left corner, and the second thermocouple is located in the far right corner, approximately 10 cm below the surface. A third thermocouple is used to record the ambient

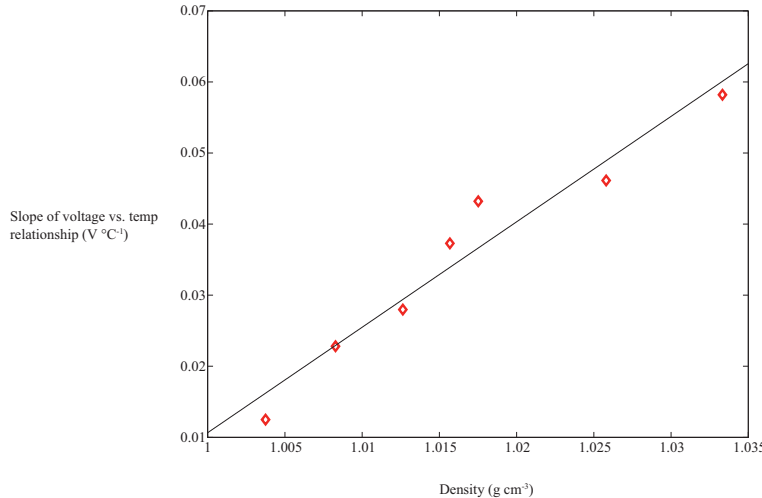


Figure 2.10: Slope values corresponding to the relationship between the conductivity probe’s voltage output and the temperature of the water plotted against density. For denser solutions, the voltage output of the conductivity probe is more sensitive to temperature differences in the tank. Specifically, the voltage will increase at a greater rate per degree for a denser solution. The conductivity profiles are shifted accordingly to correct for this dependency.

temperature of the lab. The thermocouple wires feed into a Measurement Computing DAQ USB–TC device, and profiles are recorded via TracerDAQ software at 0.1 Hz (<http://www.mccdaq.com>). The analog input channels are calibrated with *InstaCal*, a calibration and test program, provided by Measurement Computing. The output data is saved as a *.csv* file.

2.4 Particle image velocimetry (PIV)

Particle Image Velocimetry (PIV) is an optical method for obtaining instantaneous, spatially-averaged velocity measurements by tracking the movement of “interrogation windows” of tracer particles that have been seeded in the flow of interest. The setup is composed of a CCD camera, a laser, a synchronizer to act as the external trigger for control of the camera and laser, and seeding particles. Each component of the system that is utilized in the experiments is described in detail in § 2.4.1 to § 2.4.8.

2.4.1 The laser

A New Wave Research Solo 120 15Hz Nd:YAG laser (SN 25125) is used for carrying out PIV measurements. The Solo 120 encloses a dual flash lamp-pumped Nd:YAG rod head to generate radiation at 1064 nm.

Table 2.2: Relevant specifications of the New Wave Research Solos 120 15Hz Nd:YAG laser used for PIV measurements.

Solo 120	
Energy	120 mJ
Stability ¹	$\pm 4\%$
Pulse Width ²	3-5 ns
Beam divergence ³	< 2 mrad
Beam pointing ⁴	< 100 μ rad
Jitter	± 0.5 ns
Beam diameter	4.5 mm

1. Pulse-to-pulse for 98% of shots after 30 min warm-up
2. Full width half maximum
3. Full angle for 86% of the energy, $1/e^2$ point
4. Full angle for 86% of the energy, $1/e^2$ point

The system is relatively insensitive to vibrations and temperature fluctuations on account of the resonator's mechanical isolation. The second harmonic at 532 nm is generated by means of a KTP crystal, producing green light with photons of twice the energy. The laser system is fired externally with a pulse generator. Table 2.2 lists relevant specifications for the laser at 532 nm, as documented in the Solo PIV Nd:YAG Laser Operator's Manual (New Wave Research, 2002).

The laser BNC cable setup is shown in figure 2.11; also shown is the main umbilical and the secondary umbilical connection. In order to start the laser, the cooling system must first be filled with de-ionized water, as per the user manual instructions. The main power switch is turned to the ON position, the power supply key is turned to the ON position, and the START/STDBY button is pressed until the LASER EMISSION LED is on. In order to control the laser externally, once the LED stops flashing, both the Q-SWITCH and FLASHLAMP should be set to *external*, then the POWER



Figure 2.11: Photograph of BNC connections on the back of the laser power supply, as necessary for operation of the Nd:YAG laser.

switched to *high*, and each laser emission button pressed once.

2.4.2 Computer wiring

The software installed for external synching of the camera and laser, as well as for image acquisition, is DaVis *ver. 6.2* by LAVISION. The software is installed with a Dongle (SN DH6E6) that plugs into the printer port of the computer, and is in essence the licensing of the software. Two 32-bit PCI cards with corresponding drivers are installed in the computer: the Programmable Timing Unit (PTU8) board and the camera interface board. A photograph of the hardware cabling is shown in figure 2.12. The PTU8 board contains two ribbon cables, one for connection of PTU Port A (camera) and PTU Port B (laser). The camera interface board panel contains an RJ45 (ethernet) socket, which connects the camera head and the PCI board. A High Density Dsub26 socket houses a cable with a BNC end connection, which joins the PCI board to the PTU8 ribbon cable designated for the camera. The ethernet cable is a 14ft CAT 6 RJ45 cable; a high quality ethernet cable is necessary for the system to work properly.

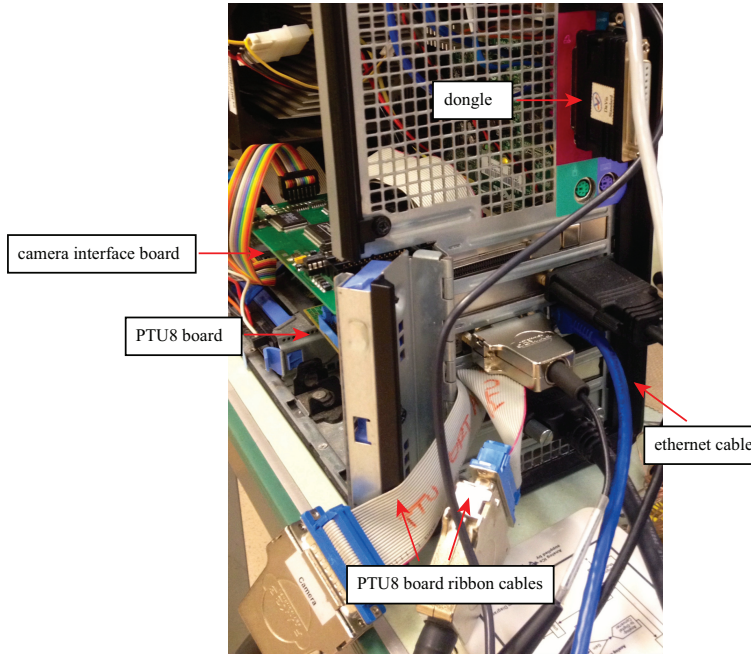


Figure 2.12: Photograph of computer wiring for the laser and camera. The PTU8 card synchronizes the laser pulse and the camera, while the ethernet cord in the camera interface board connects the camera head to the computer.

2.4.3 DaVis 6.2 software

DaVis 6.2 Imaging software is used for image acquisition. As a reference for future users of the laser and software, key features of the setup process which are not documented in the relevant user manual are as follows:

1. Under the Devices/Hardware Setup/General tab, the *PTU-controlled laser/light source* box should be checked, with the double-pulse Nd:YAG (PIV) laser selected, along with its PCI slot location.
2. Under Devices/Hardware Setup/Camera 1 tab, Camera 1 should be selected as *Imager Compact/Falcon*, the CCD exposure should be set to *automatic* and the *Programmable Timing Unit (PTU)/sequencer* box should be checked, *version PTU 8.x*.
3. Under Devices/Hardware Setup/Sequencer/PTU 1 tab, the mode should be selected as *image/burst* with internal rate generation, and the frequency of the cam-

era may be modified in the *frequency* box. The maximum frequency of the Imager Compact is 10 Hz.

4. Under Devices/Hardware Setup/PTU Laser Control tab, the *Laser 1 active* box should be checked, and the laser should be switched to *On*. Maximum power is 200, and the laser can shoot at a maximum of 15 Hz.
5. Under Devices/Hardware Setup/PTU Laser control/Setup tab, the *laser/trigger delay* should be set to a value between -25 and -28 μ s. This delay ensures that the laser will not fire too closely to the end of the camera exposure, so that no missing frames occur. This value may be adjusted if missing frames intermittently occur in the image buffer.
6. Under AcqSetup/Camera Parameter tab, the *Camera 1* box should be checked, and *single frame/single exposure (laser 1)* may be selected as long as the flow is slow enough where a 10 Hz acquisition rate is sufficient. The CCD exposure time is set to 1000 μ s, and the PTU is set to *internal rate generation*.
7. Under AcqSetup/Acquisition Timing tab, the *standard.acq* file is loaded.
8. In order to record images into the RAM, the Acquisition/Sequence/Summing tab is used, where a buffer may be specified for each image, and the number of desired images is specified.

Recorded images are saved as *.tif* files and exported into Fiji for post-processing (see § 2.4.7).

2.4.4 Laser sheet optics

To create the desired laser sheet size for the experiment, the Nd:YAG laser passes through a series of optics to decrease beam diameter and diverge the beam into a thin sheet of the required height. The laser head is displaced 156 cm from the side of the tank. The beam first enters a compound lens designed to reduce the beam diameter, and consequently the sheet thickness, in the vicinity of the experiment. In order to achieve a focal length that will maximally reduce sheet thickness at the mid-length point of the

experiment tank, a system consisting of one plano-concave lens and one plano-convex lens is arranged on a common axis. Invoking the thin lens approximation, which ignores optical effects due to the thickness of the lenses, the back focal length equation (*BFL*) for a two-lens arrangement is

$$BFL = \frac{f_2(d - f_1)}{d - (f_1 + f_2)}, \quad (2.14)$$

where f_1 and f_2 are the focal lengths of the two lenses, and d is the separation distance between the lenses in air. The first lens is a plano-convex lens with $f_1 = 100$ mm, and the second lens is a plano-concave lens with $f_2 = -100$ mm. Both lenses are ordered through Thor Labs, and manufactured with N-BK7 glass with an anti-reflective (AR) coating for 350–700 nm. A $d = 5$ mm brass spacer separates the two lenses, resulting in a *BFL* of 190 cm. The distance from the last lens in the two-lens system to the midpoint of the tank is 189.7 cm, thus coinciding with the *BFL*.

In order to gauge how much the beam diverges over the tank area, its diameter is assumed to have an ideal Gaussian intensity profile, with beam diameter defined as the diameter at which the beam intensity has fallen to $1/e^2$ (13.5%) of its peak value (Hecht, 2002). The radius of the beam at distance z may be calculated from

$$w(z) = w_o \left[1 + \left(\frac{\lambda z}{\pi w_o^2} \right)^2 \right]^{1/2}, \quad (2.15)$$

where w_o is the beam waist radius of the $1/e^2$ irradiance contour at the plane where the wavefront is flat, $w(z)$ is the radius of the $1/e^2$ contour after the wave has propagated a distance z , and λ is the wavelength of the laser light.

The focused spot radius at the focal point is given by,

$$w_f(z) = \frac{\lambda f}{\pi w_o}, \quad (2.16)$$

where f is the focal length. Considering an initial beam radius of $w_o = 2$ mm, the radius at the focal point created by the compound lens is $w_f = 0.16$ mm. Thus, the thickness of the sheet at the midpoint of the tank is $d_f = 0.32$ mm. Utilizing (2.16), at the outer edges of the tank, the sheet will reach a maximum thickness of 1.11 mm. The sheet thickness as a function of distance from the waist radius is shown in figure 2.13, where the blue box depicts the field of view (FOV) of the experiment.

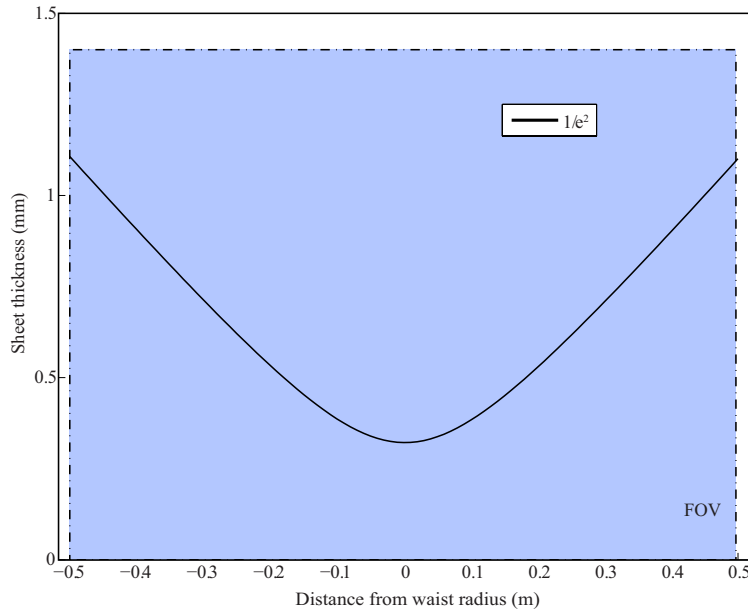


Figure 2.13: Plot of laser sheet thickness variation as a function of distance from waist diameter. The maximum thickness that the sheet reaches in the field of view (FOV), corresponding to the blue rectangle, is 1.11 mm.

In order to create the laser sheet, a 30° full fan angle laser line generator lens from Edmund Optics (with Vis- 0° coating, providing optimized transmission for 425–675 nm, reducing average reflection to 0.4% and 0.75%, respectively) is mounted downstream of the compound lens. The height of the laser sheet is calculated by,

$$x = 2 L_L \tan\left(\frac{\theta}{2}\right), \quad (2.17)$$

where x is the line height, L_L is the working distance, and θ is the full fan angle of the lens (Edmund Optics, 2013). At a distance of $L_L = 126$ cm from the lens to the side of the tank, with $\theta = 30^\circ$, a sheet of height $x = 67.5$ cm is generated, sufficient to illuminate the area of interest, which is 50 cm.

2.4.5 Setup

In order to reduce any reflection of laser light from the environment, the bottom and sides of the tank are fitted with matte black waterproof adhesive vinyl. A picture of the laser optics setup as well as the tank are shown in figure 2.14. The laser is operated

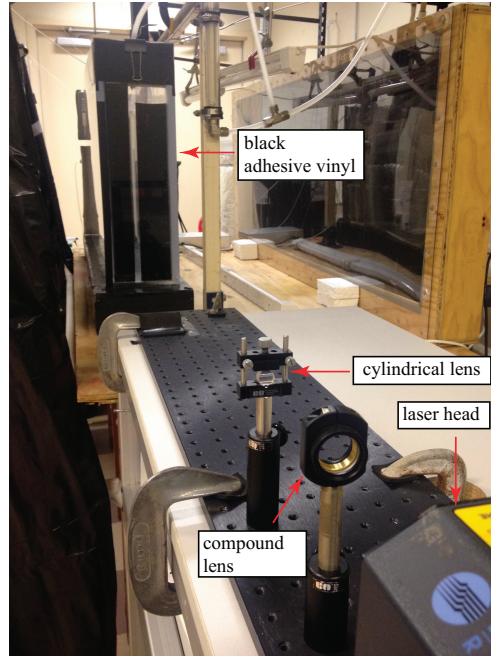


Figure 2.14: Setup of laser optics and experiment tank. Waterproof black adhesive vinyl lines the inside bottom and sides, as well as the outside wall of the tank. The matte black color absorbs laser light that would otherwise be reflected.

remotely from the PC, and data acquisition is achieved via DaVis, where at most 200 single-frame/single-exposure images may be saved to the cache before transferring to the hard drive. The PTU8 board runs internally at a fixed laser frequency of up to 15 Hz, which may be defined by the user. Before acquiring data, a background image is taken, to be later subtracted from the series of PIV images. Background image subtraction corrects for a dark current background created by the inevitable heating of the CCD chip (LaVision, 2004). The camera used for recording PIV images is an Imager Compact with a HighRes CCD sensor. Key characteristics of the sensor are given in table 2.3. The Imager Compact camera is fitted with a Cosmicar TV zoom lens 12.5–75 mm f/1.8. In order to reduce parallax, the camera is displaced approximately 4 m from the mid-length of the tank. The f-stop used for PIV recording is f/2.8.

Table 2.3: Key characteristics of HighRes CCD sensor located inside the Image Compact camera used for PIV image recording.

HiRes CCD sensor	
Number of pixels (H × V)	1360 × 1024
Pixel size	4.65 × 4.65 μm ²
Sensor format	1/2"
Scan area	6.3 × 4.7 mm ²

2.4.6 Seeding particles

The seeding particles used for PIV are Potters Industries Conduct-o-fil silver-coated hollow glass spheres (PN SH400S20), with an average diameter of 13 μm and average density of 1.6 g cm⁻³. In order to ensure that the particles faithfully follow the flow field, the Stokes number (Stk) must be considered. The settling, or terminal, velocity \mathbf{u}_g of a sphere falling through a fluid is given by Stokes' drag law (Raffel et al., 1998),

$$\mathbf{u}_g = \frac{d_p^2(\rho_p - \rho)}{18\mu} \mathbf{g}, \quad (2.18)$$

where \mathbf{g} is the gravitational acceleration, d_p and ρ_p are the diameter and density of the particle, respectively, ρ is the density of the working fluid, and μ is its dynamic viscosity. The Stokes number is then a ratio of the characteristic timescale of a particle, u_g/g , and the characteristic timescale of the flow d/U_o ,

$$\text{Stk} = \frac{U_o u_g}{d g}, \quad (2.19)$$

where U_o is the velocity of the flow, and d is the characteristic dimension of the flow. In order for the particles to act as passive tracers in the flow field, the advective motion of the fluid must be much greater than that of the particles. When $\text{Stk} \ll 1$, the particles will advect with the flow streamlines; conversely, if $\text{Stk} \gg 1$, the particles may detach from the flow and continue along their initial trajectory. Conservatively, taking ρ and μ to be properties of freshwater at 20°C, the settling velocity of the hollow glass spheres is 5.51×10^{-5} m/s. Thus, even if the flow maintained velocities on the order of 1 m s⁻¹ (typical flow velocities are $\mathcal{O}(\text{cm s}^{-1})$), with $d = 50$ cm (the height of the tank), Stk would be $1.12 \times 10^{-5} \ll 1$. The flow does not exhibit large enough velocities or abrupt acceleration/deceleration which could cause the particles to detach from the flow

on account of drag. If the fluid is at a density greater than that of freshwater, u_g would be even smaller, requiring larger flow velocities to bring St_k towards unity. Alternatively, as long as the flow maintains velocities where $U_o > u_g$, the particles will not settle out of the flow field. Therefore, the hollow glass spheres are expected to provide flow tracer fidelity as long as the flow velocities remain larger than the settling velocity of the particles. In practice, a subset of the performed experiments did experience a shutdown of the plume, below which the particles, if any, are expected to settle out of the flow field; the velocity measurements in these stagnant regions are not used, and assumed to be close to zero.

2.4.7 Digital image processing

After PIV images are captured and saved onto the hard drive, the sequences are pre-processed using standard techniques in order to facilitate calculation of the velocity field. Image restoration and enhancement are carried out using Fiji Open Source image processing package (Schindelin et al., 2012). First, the image brightness/contrast is automatically optimized based on the intensity histogram of the region of interest. A 3×3 or 5×5 pixels² median filter is applied to the resulting stack of images in order to reduce shot noise (Adrian and Westerweel, 2011). The filtered image series is then subtracted from the original image series in order to correct for any background intensity variations due to laser reflections, salt and pepper noise from the CCD, etc... Finally, the image histogram is equalized to account for any overly bright spots that may bias processing.

2.4.8 PIV processing

The digitally restored and enhanced PIV images are processed in PIVlab *ver. 1.35*, a time-resolved digital PIV tool for MATLAB (Thielicke and Stadhuis, 2014). Before any calculations are carried out, a region of interest (ROI) is specified, followed by masking of no-flow regions that protrude into the ROI. The implemented cross-correlation algorithm is a direct Fourier transform correlation with multiple passes and deforming windows, known as *FFT window deformation*. This algorithm analyzes the

data in three passes, with the interrogation window area sequentially decreasing from 128×128 to 64×64 to 32×32 pixels², each with 50% overlap. This procedure results in a high vector resolution, signal-to-noise ratio, and dynamic velocity range. Between the passes, missing velocity information is interpolated with a spline curve; this is not done after the final pass. Sub-pixel precision is achieved by fitting the intensity distribution of the correlation matrix with a 2D Gaussian function (Thielicke, 2014). The resulting velocity field is converted into real-world units by inputting a reference distance and time step. Finally, data validation is performed in which outliers are removed by setting limits on the mean velocity and employing a standard deviation filter. The resulting velocity fields are slightly smoothed before calculation of derivatives.

2.5 Experiment procedure

From start to finish, the general procedure for each experiment spans a total of three days. First, dense water is mixed and allowed to equilibrate for at least 12 hrs prior to starting the experiment. The experiment tank is also filled with fresh deionized water at this time, and likewise allowed to sit overnight to degas and equilibrate. The next day, before the experiment is started, the density of the saline water is measured. The freshwater pump is turned on, and the flow rate is given a few minutes to stabilize. Once the flow rate of freshwater is constant, it is measured using a 1000 cm³ graduated cylinder and stopwatch. A background synthetic schlieren image is obtained by recording the tank for 5 s at 12 Hz with the SS mask switched on, and saving a time average of the recorded sequence. The TracerDAQ temperature recording software is initialized, and the dense water pump is turned on. After the constant head bucket is full and the dense water flow has stabilized, the rate of the outflow is measured and recorded. The experiment is covered with insulation, and allowed to run for at least 6 filling cycles. The time of one filling cycle ranges between 7.36–8.28 hrs, depending on the dense water flow rate. In the interim, the outflow flow rate and density are measured and recorded, and the calibration standard densities are measured.

Conservatively, the timescale for equilibrium is given by the filling timescale, τ_f , previously defined in § 1.2.2. This filling timescale has been shown to provide a

cautious upper limit on the time required to reach equilibrium (Stewart et al., 2012). All experiments are run for at least $6 \times \tau_f$ before the first set of data collection. Equilibrium is verified when the overflow salinity has asymptotically approached the mean salinity in the system, and the density profile obtained by the conductivity probe remains unchanged between data sets. The overflow volumetric flow rate per spanwise width is given by

$$Q_0 = Q_d + Q_f, \quad (2.20)$$

where the subscripts d and f correspond to the dense and freshwater source properties, respectively, so that the equilibrium salinity may be represented by source values which are known *a priori* for each experiment

$$S_0 = \frac{Q_d S_d + Q_f S_f}{Q_0} = \frac{Q_d S_d}{Q_d + Q_f}, \quad (2.21)$$

and S_f has been taken to necessarily equal 0.

Approximately 12 hrs before data are recorded, seeding particles are mixed into the dense water tank. Typically, the concentration of seeding particles in the dense water is 4.4 g m^{-3} . Experiments have shown that seeding only the dense water source is enough to create a homogeneous dispersion of seeding particles in the ROI by the time data recording takes place. The first set of data are collected at least 48 hrs into the experiment. The first collection process is as follows:

1. Measure outflow flow rate and density
2. Run calibration on conductivity probe
3. Take conductivity profile (approximately 38 min)
4. Run second calibration on conductivity probe
5. Record synthetic schlieren for 300 frames at 1 Hz
6. Record PIV images; 200 images each at 1 Hz, 5 Hz, and 10 Hz

The second set of data are collected approximately 4 hrs after the first set, or half a filling time cycle apart. The procedure is as follows:

1. Measure outflow flow rate and density
2. Record PIV images; 200 images each at 1 Hz, 5 Hz, and 10 Hz
3. Record synthetic schlieren for 300 frames at 1 Hz
4. Run calibration on conductivity probe
5. Take conductivity profile (approximately 38 min)
6. While conductivity profile is being recorded, add $\sim 0.024 \text{ kg m}^{-3}$ KMnO₄ to the dense water source and record flow for approximately 25–30 min at 0.2 Hz
7. Run second calibration on conductivity probe
8. Turn off freshwater and measure dense water flow rate

The dye visualization may only be recorded for the last set on account of KMnO₄ creating nonuniform illumination in the tank, which would interfere with PIV recording. The dye is only added to the dense source to isolate the progression of the plume outflow.

Chapter 3

Experiments with concurrent mechanical and buoyancy forcing imposed on the surface

A total of 15 experiments have been carried out in which the surface stress is applied in the same direction as the flow driven by surface buoyancy fluxes. The setup is schematized in figure 2.1, and corresponds to the black dashed line for the dense source tubing position. In this configuration, the salty plume drives a counterclockwise circulation, with flow moving from right to left at the upper boundary. The surface stress is likewise imposed from right to left, so that it acts in the same direction as the convecting cell. The freshwater volumetric flow rate is varied between $Q_f = 19.74 - 253.67 \text{ mm}^2 \text{ s}^{-1}$. A summary of the experiments and relevant quantities are presented in table 3.1.

Fluid attributes are calculated using a MATLAB package which contains thermophysical properties of seawater (web.mit.edu/seawater/) with validation of property values given in Sharqawy et al. (2010). Where appropriate, properties are defined using the mean of the recorded top and bottom temperatures in the tank (see § 2.3.5), and the mean density for each experiment. Because the freshwater flow rate is determined using a graduated cylinder and stopwatch, these measurements are subject to systematic error, particularly when measuring relatively large flow rates. The mean of all recorded measurements per experiment is thus used for the final freshwater flow rate. The specific

buoyancy flux is calculated using

$$B_0 = g\beta(S_d - S_f)Q_d, \quad (3.1)$$

where β is the coefficient of expansion for salt, equal to 0.69, S_d is the salinity of the dense water source, S_f is the salinity of the freshwater source ($S_f = 0$), and Q_d is the dense water flow rate per spanwise width, held constant at $16.77 \text{ mm}^2 \text{ s}^{-1}$. The value of B_0 varies between $(2.01 - 5.57) \times 10^{-6} \text{ m}^3 \text{ s}^{-3}$ for the set of experiments. Using molecular values of the diffusivities, $v = 9.35 \times 10^{-7} \text{ m}^2 \text{ s}^{-1}$ and $\kappa = 1.38 \times 10^{-9} \text{ m}^2 \text{ s}^{-1}$, *a priori* calculations of the Rayleigh and Prandtl numbers are $Rab = (1.13 - 3.13) \times 10^{18}$ and $Pr = 678$, respectively.

To estimate the magnitude of τ_{max} , this quantity is parameterized by

$$\tau_{max} = v \frac{\partial u}{\partial z} \approx \frac{vU_{max}}{\delta_f} \approx \frac{vQ_f}{\delta_f^2}, \quad (3.2)$$

where $U_{max} \approx Q_f \delta_f^{-1}$, and δ_f is the thickness of the freshwater layer on the surface of the experiment, obtained from SS images taken before any density anomalies are introduced into the working volume. A parameterization of the shear stress is necessary because PIV measurements of the velocities near the boundary layer are unreliable on account of high density gradients in the region. Generally, the thickness of the freshwater layer varied less than the pixel resolution of approximately 0.83 mm, and an average value was used where applicable. The nondimensional parameter S_{δ_f} is in the range 0.12–1.27, remaining $\mathcal{O}(1)$ for the experiment set. Uncertainties in the freshwater flow rate and layer thickness introduce a maximum error of 20% in calculated S_{δ_f} values.

The boundary layer thickness is defined as the depth at which the upper flow contains 95% of the maximum density anomaly within the domain. The density difference used in calculating this value is taken between the density measured at the full extent of the conductivity probe's traverse, $z \approx -0.5H$, and the density at the interface of the freshwater and working volume. For experiments that exhibit no turbulent mixing (see § 3.1), the interfacial density is that of freshwater, which consistently flushes the upper boundary. Once turbulence is present, the freshwater layer increases in density immediately upon entering the working volume due to interfacial mixing near the freshwater source. Consequently, the interfacial density is no longer that of freshwater. The

Table 3.1: Summary of relevant quantities for concurrent experiments. The quantity u_f is the horizontal velocity in the freshwater layer, calculated by normalizing Q_f with the thickness of the freshwater layer it produces before any density anomalies are introduced into the working volume. For Exps 1–6, the turbulent mixing coefficient, $\kappa^*(z)$, is uniform in the volume, and taken to equal $2.67 \times 10^{-9} \text{ m}^2 \text{ s}^{-1}$ (Stewart et al., 2012). For Exps 7–16, the value listed in the table only encompasses the diffusivity in the upper region where mixing is present; below this region, it takes on the molecular value, $\kappa^* = 1.38 \times 10^{-9} \text{ m}^2 \text{ s}^{-1}$. $\Delta\rho_{max}$ is the maximum density difference between the source and sink. $\delta_{0.95}$ is the thickness of the boundary layer responsible for containing 95% of the maximum density difference in the working domain. ψ_{max} is the maximum streamfunction estimated from PIV measurements. Horizontal lines indicate experiments with poor PIV quality for which a reliable measure of ψ_{max} could not be achieved. Experiments with no streamfunction measurement are also outlier points and are not included in the analysis.

Exp #	u_f (mm s $^{-1}$)	$\kappa^*(z)$ (m 2 s $^{-1}$)	$\Delta\rho_{max}$ kg m $^{-3}$	S_{δ_f}	$\delta_{0.95}$ (mm)	ψ_{max} (mm 2 s $^{-1}$)
1	2.66	2.67×10^{-9}	33.24	0.12	2.44	247
2	2.18	2.67×10^{-9}	13.17	0.16	2.64	80
3	3.08	2.67×10^{-9}	23.42	0.17	4.17	—
4	6.25	2.67×10^{-9}	32.87	0.29	3.56	214
5	6.13	2.67×10^{-9}	23.03	0.34	5.99	—
6	5.38	2.67×10^{-9}	13.16	0.40	4.57	89
7	9.18	1.48×10^{-6}	33.07	0.42	41.05	898
8	10.47	3.50×10^{-6}	22.76	0.58	143.97	1241
9	13.18	3.85×10^{-6}	32.81	0.60	70.10	1499
10	9.88	6.43×10^{-6}	13.19	0.73	76.50	—
11	15.93	1.04×10^{-5}	22.87	0.88	204.83	1544
12	18.61	1.49×10^{-5}	23.55	1.01	173.33	2025
13	15.87	2.26×10^{-5}	13.02	1.19	149.35	2003
14	16.92	2.73×10^{-5}	12.81	1.27	167.74	2164
15	28.03	2.73×10^{-5}	32.60	1.28	103.73	2378

maximum streamfunction, ψ_{max} , is calculated from PIV measurements. Typically, data recorded at 10 Hz for 20 sec is temporally averaged to resolve eddying structures in the flow. The resulting velocity fields are 2D spatially averaged mappings over 32×32 pixel 2 windows, corresponding to a resolution of approximately 1.46 cm in world coordinates in either direction. A MATLAB script which integrates the velocity matrices using Simpson rule summation (Pankratov, 1994) is implemented to calculate ψ_{max} . X

and y integration constants are computed from the non-forced boundary and away from the plume, respectively. The first few cm from the surface of the streamfunction are omitted when calculating ψ_{max} so that the data is not skewed by the freshwater flow rate.

Qualitative and quantitative results of the experiments are presented in §§ 3.1 and 3.2, followed by a discussion on relevant instability criterion and equilibration timescales in § 3.3. The governing physics of the flow is presented in § 3.4, as well as comparison of theory and experiments in § 3.5. Further discussion is presented in § 3.6. Finally, results are summarized in § 3.7, and potential implications of the current results on large bodies of water subject to oscillatory mechanical forcing over relatively long timescales is considered.

3.1 Qualitative results

For small values of $S_{\delta f}$, the steady-state circulation exhibits qualitative flow features similar to those observed in experiments in which horizontal convection is driven by differential heating (e.g. Mullarney et al. 2004) as well as by solutal buoyancy forcing (Stewart et al. 2012). Specifically, a turbulent plume descends the full depth of the tank along the left-hand wall, detraining into the interior upon reaching the bottom boundary. Upstream of the region of outflow, the plume is narrow in that it does not encompass more than 20% of the tank length. The eddying outflow is distributed along the whole length of the tank base, and the circulation is closed via widespread upwelling throughout the interior back to the surface with marked entrainment into the plume at all heights. Figure 3.1 shows a typical velocity field for low values of $S_{\delta f}$, exposing the eddying plume outflow into the tank interior, a broad upwelling region, as well as the global asymmetric nature of the circulation.

For experiments in which $S_{\delta f} > 0.42$, stabilizing effects near the freshwater inlet are no longer able to dampen out shear-induced perturbations, resulting in a localized region of mixing that increases in depth linearly with increasing $S_{\delta f}$, as shown in figure 3.2. Internal waves are visible at the interfacial layer between the convective cell and underlying quiescent region. The gradually increasing turbulent diffusivity in the upper

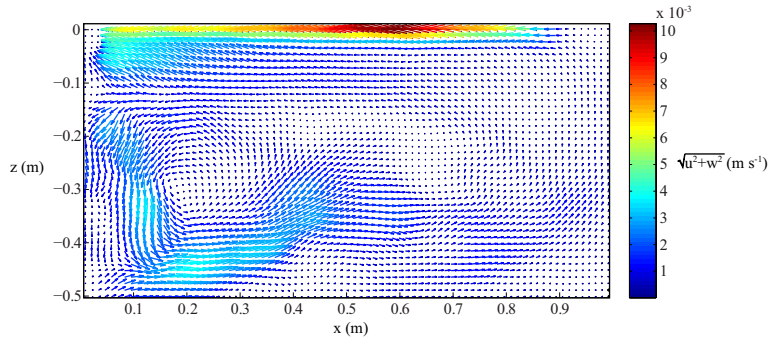


Figure 3.1: Steady-state velocity field for an experiment with $S_{\delta f} = 0.12$, obtained from PIV measurements. The magnitude of the vectors are stretched by a factor of 7 for increased visibility. The colormap represents the velocity magnitude, which is at a maximum near the tank surface where the surface stress is imposed.

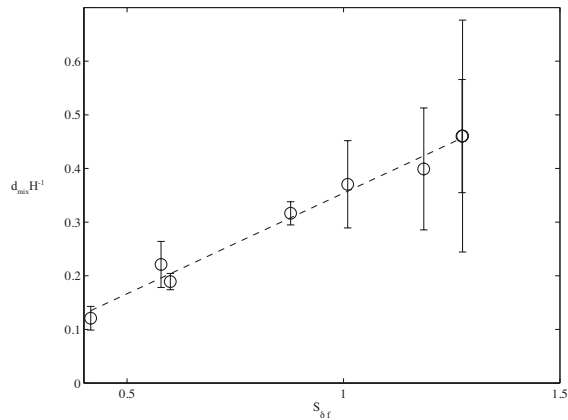


Figure 3.2: Mixed layer thickness, d_{mix} , normalized by tank depth vs. $S_{\delta f}$. For values of $S_{\delta f} > 0.42$, the depth of the mixed layer increases linearly with increasing $S_{\delta f}$. The least-squares fit (dashed line) corresponds to $d_{mix} = 0.1875 \times S_{\delta f} - 0.0105$. Estimates of the mixed layer thickness by means of various methods, including PIV data, SS data, and dye visualization data, are used to calculate the magnitude of the error bars.

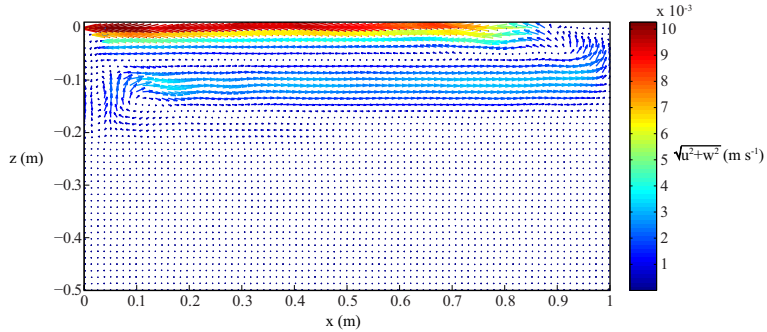


Figure 3.3: Steady-state velocity field for an experiment with $S_{\delta f} = 0.88$. The magnitude of the vectors are stretched by a factor of 7 for increased visibility. The colormap represents the velocity magnitude, which is a maximum near the tank surface where the stress is forced.

region of the flow creates a persistent perturbation in the form of a net buoyancy flux input that renders the plume too weak to penetrate the full volume, instead forcing it to detrain in the interior at partial depth. The result is a shallow convecting cell overlying a stagnant region, with the minimum detrainment depth set by d_{mix} . In all experiments that exhibit a partial-depth circulation, a laminar sublayer develops along the left-hand wall. The sublayer admits a pathway for dense fluid to reach the bottom boundary, sustaining the density of the fluid in the layer below the plume outflow. Evidence of this sublayer in stratification profiles are presented in § 3.2. Figure 3.3 is a typical velocity field for experiments with $S_{\delta f} > 0.42$, displaying a plume that detrains into the interior at an intermediate depth, overlying a relatively stationary fluid layer. In contrast to the observed circulation for $S_{\delta f} < 0.42$, the flow field exhibits a higher degree of symmetry. The interior vertical velocity of the plume effluent is confined to a region of upwelling near the boundary opposite the one at which the plume is forced, as opposed to the broadly distributed interior upwelling characteristic of experiments with $S_{\delta f} < 0.42$.

3.2 Quantitative results

Figure 3.4 plots interior density profiles obtained from conductivity probe measurements extending to approximately the mid-depth of the tank, normalized by the maximum density difference between the dense and freshwater source. The normalized

density is defined as

$$\rho_n(z) = \frac{\rho(z) - \rho_f}{\rho_d - \rho_f}. \quad (3.3)$$

The origin of all profiles is taken to be at the interface between the upper freshwater layer and the working volume. On account of mixing with the upper freshwater layer, the density of the upper layer is not at the density of freshwater near the overflow, where the conductivity probe is mounted; as a consequence, the profiles do not start at zero. The dashed and solid lines in figures 3.4(a) to 3.4(c) correspond to two separate runs recorded per experiment. Comparison of the synchrony of the two separate data sets serves as an indication of the acquirement of an equilibrated flow. To elaborate, if the two profiles match identically, it is a strong indication that the flow has reached a steady state in which the density field is no longer evolving. The profiles suggest that as the initial density of the plume is increased, the flow is relatively more unsteady. The mismatch between measured profiles may be a result of temporal intermittency, which is expected to occur in an eddying flow. Further evidence of these dynamic fluctuations is present in profiles at $S_{\delta f} = 0.28$ and 0.42 in figure 3.4(c). The inverted shapes suggest an unstable stratification, which cannot be maintained. It is therefore inferred that for a subset of explored flow fields, measurements are recorded too close to the vicinity of the plume, and the frequency of sampling per point is too short, causing the recorded data to be affected by turbulent eddies near the plume's edge. The chaotic behavior picked up in the conductivity measurements may only be an issue for higher density plumes, as evidenced by figure 3.4, for which the flow may be more resistant to the effects of the surface shear.

Figure 3.4(c) indicates a step in the density profiles of $S_{\delta f} = 0.42$ and $S_{\delta f} = 0.60$. This discontinuity is associated with a steep density gradient between the stagnant layer and upper circulating cell, which becomes large for shallow mixing depths. If d_{mix} is small, the range of densities mixed by small-scale turbulence is limited. Consequently, the plume entrains relatively fresher water near the surface, and is unable to penetrate past the denser interior fluid established during its initial descent. The resulting density gradient between the two layers is large and sharp enough to manifest itself as a step in the density profile.

Figure 3.4(d) shows a cumulative plot of the average normalized interior den-

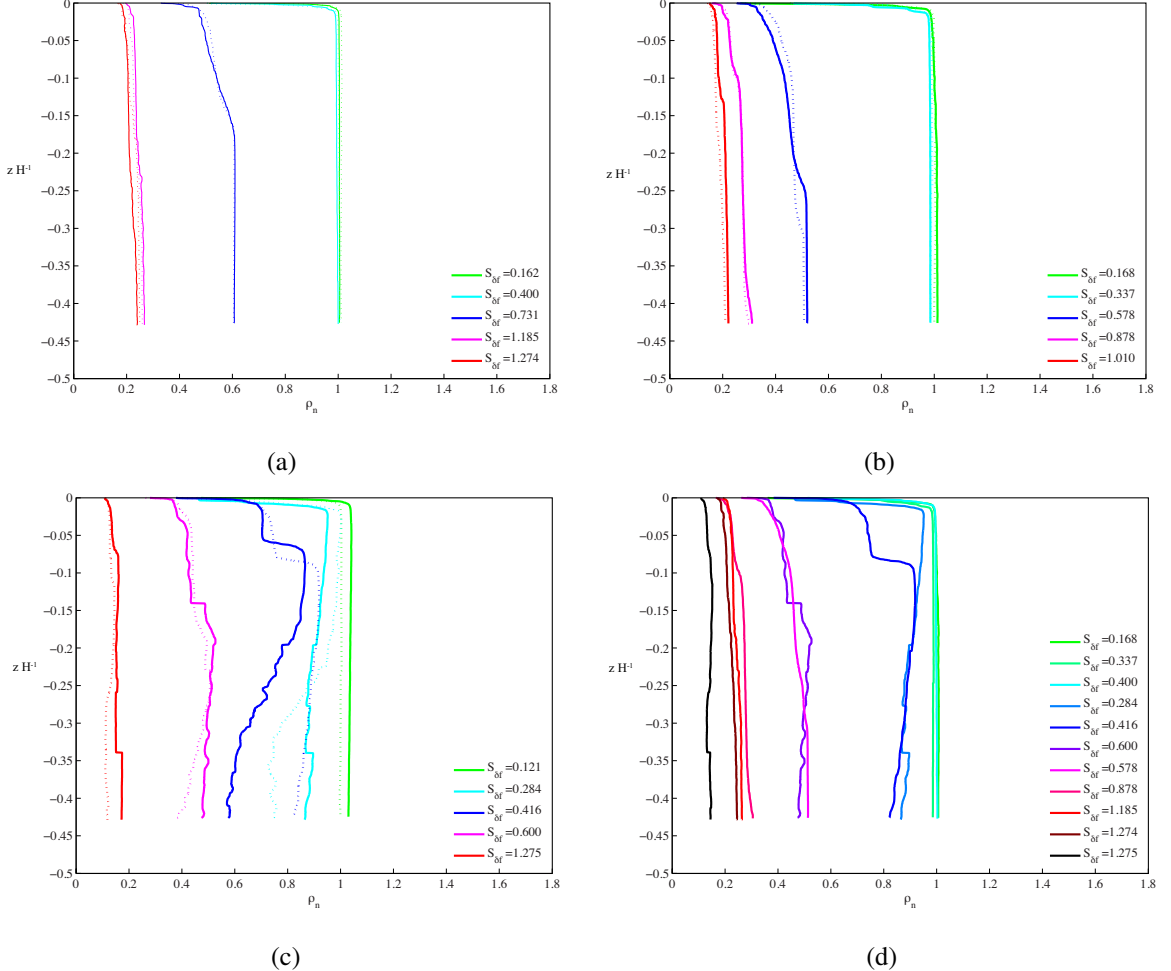


Figure 3.4: Plots of normalized interior density measured by the conductivity probe as a function of normalized depth. Because the conductivity probe could only measure the upper half of the domain, the profiles end just shy of the normalized half-depth of the tank. (a) – (c) plot profiles recorded during the first set (solid lines) and second set (dashed lines) of data acquisition. (a) and (b) plot experiments where the initial density of the plume is approximately 1010 kg m^{-3} and 1020 kg m^{-3} , respectively. All experiments show close agreement between the two sets of data collection (recorded approximately half a filling timescale apart, i.e. ~ 4 hrs), indicative of the flow reaching an equilibrated state. (c) plots the normalized profiles for an initial plume density of 1030 kg m^{-3} . The two sets of profiles per experiment are less well aligned, indicating a noisier circulation. (d) is a cumulative plot of the average normalized density profiles in (a)–(c).

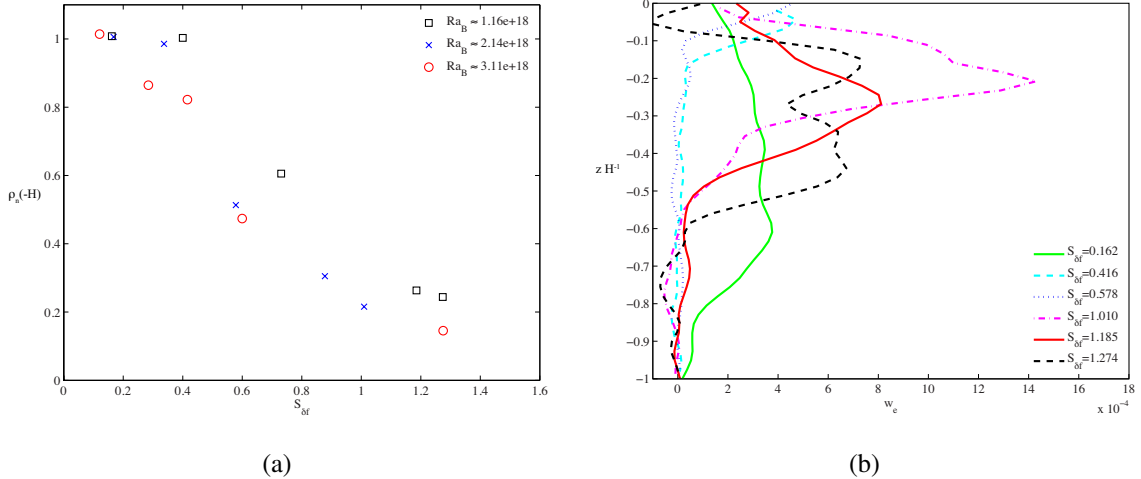


Figure 3.5: (a) Normalized interior density at $z \approx -0.5H$ as a function of $S_{\delta f}$ and (b) mean profiles of the interior vertical velocity, W_e . Each marker symbol in (a) corresponds to a different average value of Ra_B as indicated in the legend. Profiles in (b) are obtained by horizontally averaging W_e outside the plume region in PIV measurements.

sity profiles for select experiments. In the limit that $S_{\delta f} < 0.42$, the interior density structure is in agreement with previously observed profiles (e.g. Mullarney et al. 2004; Stewart et al. 2012). More specifically, the interior density field features a relatively thin boundary layer at the forcing boundary overlying a weakly stratified interior which is at a density close to the dense water source. As $S_{\delta f}$ is increased past 0.42, turbulence incorporates freshwater into the domain, thickening the boundary layer and freshening the interior at all depths.

Figure 3.5(a) plots the normalized interior “bottom” density in the environment, measured at the maximum extent of the conductivity probe’s reach, $z \approx -0.5H$, as a function of $S_{\delta f}$. Because the conductivity probe cannot sample the full depth of the volume, the density at half-depth is used as a surrogate of the bottom density, noting that the interior density profile is not expected to change significantly at depth. In hindsight, the half-depth measurement is a more accurate quantifier of the interior density on account of the laminar sublayer supplying the base of the domain with dense fluid independent of the overlying interior density. The normalized density decreases monotonically with increasing stress for fixed Ra_B , indicating that the environment is becoming fresher. Additionally, the interior normalized density decreases with increasing Ra_B , at fixed $S_{\delta f}$.

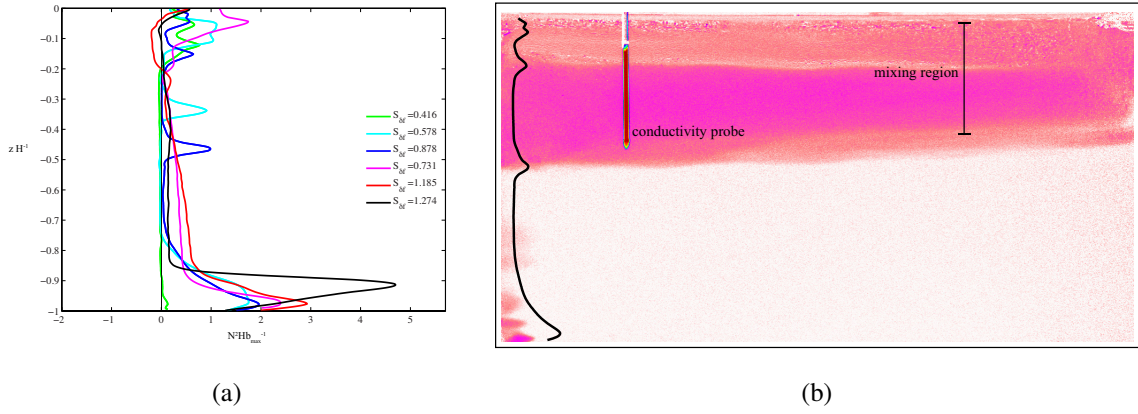


Figure 3.6: (a) Profiles of the normalized buoyancy frequency obtained from SS measurements for various values of $S_{\delta f}$. (b) is a snapshot of the steady-state plume outflow with its corresponding $N^2(z)$ profile superposed on the dye image for an experiment with $S_{\delta f} = 0.86$. The profile correlates well with regions of pronounced density change. The laminar sublayer is evident at the bottom boundary. The bottom stratification in (a) is likewise indicative of a laminar sublayer supplying dense fluid to the base of the tank.

Figure 3.5(b) plots profiles of the horizontally averaged interior upwelling velocity, W_e , outside of the plume region for select experiments. The profile shapes are qualitatively similar to those reported in Hughes et al. (2007), obtained from numerical simulations by Mullarney et al. (2004). For experiments with $S_{\delta f} < 0.42$, the average interior velocity profile is nonzero for the full extent of the domain (barring the boundaries), with maximum velocities of approximately 0.4 mm s^{-1} . For experiments with $S_{\delta f} > 0.42$, the velocity profiles tend toward 0 at varying depths, revealing relatively stagnant regions below corresponding detrainment levels. Maximum vertical velocities vary between $0.6\text{--}1.5 \text{ mm s}^{-1}$. All profiles support the general trend of increasing W_e with depth due to entrainment into the plume. For $S_{\delta f} > 0.42$, the interior vertical velocities in the experiments are generally larger than those observed for full-depth convective cells (e.g. Mullarney et al. 2004; Stewart et al. 2012), but occur over a smaller region as upwelling becomes more confined. For experiments with $S_{\delta f} < 0.42$, the plume is assumed to be narrow and the length of the interior region over which upwelling occurs is approximated as a constant equal to the length of the tank, L , in the plume equations. Because this is no longer true for experiments with $S_{\delta f} > 0.42$, fluxes are compared in lieu of velocity values in § 3.5.

Qualitative and quantitative data both corroborate the development of a laminar sublayer against the endwall adjacent to the plume. Dense fluid near the tank base is evident in profiles of the buoyancy frequency, $N^2(z) = -g\rho_0^{-1}\rho_z$, obtained from synthetic schlieren measurements by averaging the vertical density gradient outside of the plume and mixing regions. Figure 3.6(a) displays these horizontally averaged interior profiles of $N^2(z)$ normalized by the maximum buoyancy. The buoyancy frequency at the bottom boundary is invariably stable and increases with $S_{\delta f}$, in agreement with freshening interior waters as $S_{\delta f}$ is increased. Figure 3.6(b) is a snapshot of the steady-state plume outflow with its corresponding $N^2(z)$ profile superposed on the dye image. Undulations in the $N^2(z)$ profile correlate well with pronounced regions of strong density gradient; small finger-like intrusions of dyed fluid expose the laminar sublayer at the tank bottom against the endwall. Discrete density measurements of fluid taken from the left-hand corner of the tank confirm that the average density within the sublayer is approximately 99% of the dense plume source introduced into the tank. The implications of the laminar sublayer are further investigated in § 3.6.

3.3 Stability and adjustment

The surface shear imposed by the layer of freshwater excites instabilities if it can overcome the suppressing effects of the vertical stratification beneath it. Some insight into the threshold for instability may be obtained by considering the gradient Richardson number between the freshwater layer and underlying circulation,

$$Ri = \frac{N^2}{u_z^2}. \quad (3.4)$$

For continuously stratified parallel flows, the system is expected to be unstable to Kelvin–Helmholtz wave formation if there exists a critical value of Ri somewhere in the flow such that $Ri_c < 0.25$. Alternatively, turbulent flow is expected to become stable at a different critical point, namely when $RiT > 1$ (Stull, 1988). While this does not always apply to all distributions of $u(z)$ and $N(z)$, these threshold values still remain a useful measure by which to predict instability of a stratified shear layer (Kundu et al., 2012). In the present experiments, the region near the freshwater source is unstable from the onset

of the experiment, and only becomes stable once a vertical stratification develops that is strong enough to inhibit growing modes. Thus, the sought after value of Ri is expected to be closer to Ri_T . Although profiles of $N^2(z)$ are readily available from conductivity probe measurements, the vertical gradient of the horizontal velocity near the interface of the freshwater layer and underlying circulation is too steep to be resolved by the PIV configuration. Therefore, a parameterization of Ri , or the bulk Richardson number, Ri_B , is used instead, and defined as

$$Ri_B = \frac{-g\Delta\rho\Delta z}{\rho_0 U_{max}^2}, \quad (3.5)$$

where $\Delta\rho$ is the density difference between the upper and lower layer over the thickness Δz , and the lower layer is assumed to be stationary relative to the fast-moving freshwater layer so that the vertical gradient of the horizontal velocity is parameterized by $u_z \sim \Delta u \Delta z^{-1} \sim U_{max} \Delta z^{-1}$. Because the critical Ri values of 0.25 and 1 only apply when local gradients are considered, the thresholds are used with caution. However, critical values of Ri_B are expected to approach Ri_c and Ri_T in the limit $\Delta z \rightarrow 0$. Figure 3.7 shows a plot of Ri_B as a function of $S_{\delta f}$, calculated using values obtained during the experiment (i.e. not *a priori*) with $\Delta z = 2.03$ mm. The red squares correspond to experiments where no mixing is detectable, whereas the black circles correspond to experiments in which regional mixing develops. The experiment closest to the threshold value of $S_{\delta f} \approx 0.42$ corresponds to $Ri_B \approx 4.50$; experiments with $S_{\delta f}$ values beyond this point maintain $Ri_B < 0.78$. The important point to note is that figure 3.7 suggests a threshold value for Ri_B around $S_{\delta f} \approx 0.42$ that approximately agrees with the threshold at which mixing is present in the flow.

Regional mixing near the freshwater inlet introduces a sustained perturbation in the form of a buoyancy flux input. As the region of mixing deepens, it continually freshens the water available for entrainment, resulting in a weakened plume that detains into the interior at partial depth. This flux of buoyancy continues until an equilibrium depth is reached. The resulting flow consists of an upper circulating cell overlying a relatively stagnant layer of denser water.

Transient adjustment arguments of Griffiths et al. (2013) suggest that this form of perturbation will fully equilibrate on a timescale proportional to the time required for conduction to act through the stagnant layer of thickness d (see § 1.2.2). Using molecu-

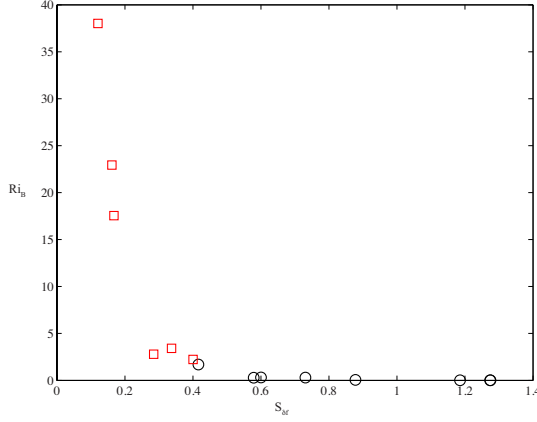


Figure 3.7: Ri_B as defined in (3.5) plotted as a function of $S_{\delta f}$. The black circles and red squares correspond to experiments with and without regional mixing, respectively. The experiment closest to the threshold value of $S_{\delta f} \approx 0.42$ corresponds to $Ri_B \approx 4.50$; experiments with $S_{\delta f}$ values beyond this point maintain $Ri_B < 0.78$.

lar diffusivity through this layer, with the maximum thickness of the stagnant layer taken to be $d = 0.43$ m (the deepest stagnant layer observed within the experiment set), the equilibrium timescale is approximately $\tau_d = 1.7$ yrs, which is unattainable in the laboratory. Considering the shallowest stagnant layer, this timescale is still approximately 630 hrs. Based on these estimates, the perturbation induced by regional turbulence is expected to produce a quasi steady-state partial-depth circulation, persisting on relatively long timescales which depend on molecular diffusion to erode the stagnant layer. While this timescale may be realized in a thermally–driven convection experiment, it is nonviable for one that is salt–driven.

Vreugdenhil et al. (2015) study equilibration timescales using the same configuration of Stewart et al. (2012) and of the current study. The authors find that an equilibrated circulation will adjust to mixing in the upper half of the flow at a timescale equal to approximately $2(\tau_B/2) = \tau_B$ (see § 1.2.2 for the definition of τ_B), where the timescale of Griffiths et al. (2013) is a factor of 2 smaller since the freshwater layer acts along the whole boundary rather than half as in the thermally–forced experiments. The observed timescale is contingent on the presence of penetrative convection at the base of the plume which expedites the equilibration process, ensuring a steady–state flow is reached well before τ_d . This case is the most relevant to the current set of experiments since it explores a convective flow in which mixing is consistently applied to only the

upper region of the volume from the onset of the experiment. However, two important distinctions exist between the experiments of Vreugdenhil et al. (2015) and the present study that put into question τ_B as the appropriate timescale for equilibrium adjustment. With regional mixing near the freshwater source, the circulation is continually subject to an input of relatively high buoyancy flux, whereas with grid mixing, the apparatus only passes through the freshwater layer intermittently and over short intervals. In the current case, this results in fresher water masses that may develop a larger density difference between the circulating flow and underlying quiescent layer, such that penetrative convection is weakened or completely inhibited. In fact, qualitative movies of the long-time plume evolution generally show no signs of penetrative convection at the plume base. Secondly, in the present experiments, the depth of mixing is itself a function of time, in contrast to grid mixing which is supplied evenly through a predetermined depth. Here, the region of mixing near the freshwater source mixes with fluid at its boundary, increasing in depth until it reaches d_{mix} . Therefore, the plume is continually undergoing a perturbation in the form of a net buoyancy flux input, as increased diffusion is removing more and more salt out of the system. The timescale for the mixed layer to fully develop appended with the timescale to adjust to a net buoyancy flux input, τ_B , may be longer than the maximum \sim 53 hrs allocated to each experiment.

Intuitively, once the equilibrium mixing depth is reached, one would expect diffusion to act on the interface between the stagnant layer and upper circulation. The process would be similar to that involved in the evolution of the mixing depth, albeit slower since turbulent motions are expected to decay with distance from the freshwater layer. To elaborate further on adjustment toward equilibration, if the circulation has reached d_{mix} and the plume detains at intermediate depth, diffusion must consistently act on the quiescent layer, with its main function being to smear out the sharp interface. As this occurs, salt from the bottom layer will diffuse into the upper circulation, which will be compensated for by an increase in diffusion at the upper boundary as the system adjusts toward a steady state. The plume is now able to penetrate a small fraction deeper into the domain. The process continues until the stagnant layer is completely removed. The steady-state flow is expected to feature a full-depth plume with its input buoyancy flux exactly matched by diffusion of buoyancy through the upper boundary out of the

volume. One is led to again acknowledge that because the system cannot be run for a full τ_d to ensure equilibration, a partial-depth circulation may be a long-lasting transient state for the system that relies on κ_{mol} to remove stratification beyond the plume outflow. The laminar sublayer could in theory maintain a zero net buoyancy flux in the system by matching the buoyancy input through advection in the sublayer with diffusion at the interface of the circulation and stagnant layer. However, at present, there is no a definite way to check that this is indeed the case. The profiles in figure 3.4 suggest that some experiments may have in fact reached a well-developed equilibrium state, but on the other hand, the density difference required to permit a full-depth sinking plume may not be within the resolution of the probe. Therefore, to remain conservative, all observed partial-depth circulations are considered quasi steady-state flows which evolve on protracted timescales that cannot be verified with the current experiment configuration.

The input of mechanical energy by the surface stress creates turbulent motion which works to transport buoyancy downward a finite distance, consequently thickening the boundary layer. On the other hand, the imposed buoyancy flux is working to reduce the boundary layer thickness. Thus, a steady-state depth, d_{eq} , is expected to exist where the two forces balance. Noting that the depth of mixing is linearly proportional to $S_{\delta f}$, the relationship dictates that

$$d_{eq} = a \frac{U_{max} v^{1/2} L^{1/2}}{B_0^{1/2}}, \quad (3.6)$$

where a is a constant, approximately equal to 19. A plot of the scaled and actual mixing depths is shown in figure 3.8(a). The mixing depth scaling in (3.6) is compared to the Monin–Obukhov length, relevant to flows where both buoyancy and mechanical forcing are imposed on a flow. This length scale is given by

$$d_{mo} = a_{mo} \frac{u_*^3 L}{B_0}, \quad (3.7)$$

where a_{mo} is a constant equal to approximately 200, and u_* is the friction velocity, defined as $u_* = \sqrt{\tau_{max}}$ using the definition of τ_{max} in (3.2). A modification to the Monin–Obukhov length scale is proposed by Hopfinger and Linden (1982), who take into consideration the decay of turbulent kinetic energy with distance from the source of turbulence for the case of zero-mean-shear turbulence superposed on a stabilizing

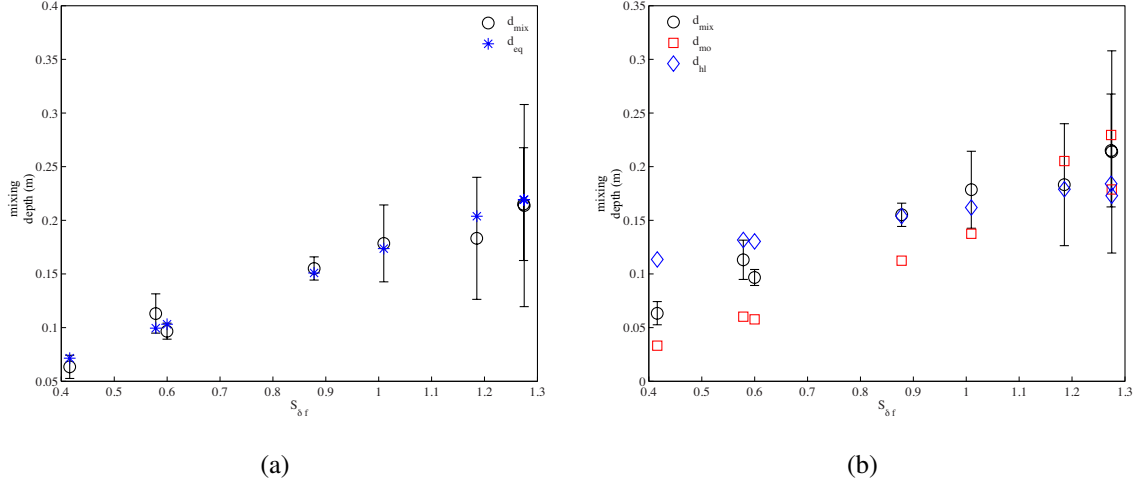


Figure 3.8: (a) Scaling of the equilibrium mixed layer depth, d_{eq} , derived from the approximately linear relationship between the mixing depth, d_{mix} , and $S_{\delta f}$. (b) plots two mixing depth scalings relevant to buoyancy flux and mechanical energy systems. The Monin–Obukhov length scale, d_{mo} , and a modified length scale by Hopfinger and Linden (1982), d_{hl} , which incorporates the decay of kinetic energy from the source.

buoyancy flux. The authors propose the scaling

$$d_{hl} = \left[\frac{u_*^3 L}{B_0} \right]^{1/4}, \quad (3.8)$$

for the mixed layer depth. Figure 3.8(b) plots d_{mo} and d_{hl} for comparison. The scaling of Hopfinger and Linden (1982) seems more relevant due to the fact that turbulent motions are expected to decay away from the trigger, which lives at the interface of the freshwater layer and circulation. Moreover, it offers slightly more accurate correlation with experiment measurements compared to d_{mo} .

The scaling for d_{hl} can be recast in terms of U_{max} ,

$$d_{hl} = \frac{\nu^{3/8} U_{max}^{3/8} L^{1/4}}{\delta_f^{3/4} B_0^{1/4}} \sim \frac{\nu^{3/8} U_{max}^{3/8}}{B_0^{1/4}}, \quad (3.9)$$

which suggests a relatively weaker function of B_0 than (3.6). There is not a wide enough range of data to verify which scaling more accurately describes the equilibrium depth. However, the notion that the measured depths are explained well by either scaling suggests that the equilibrium depth is in fact attained for each experiment.

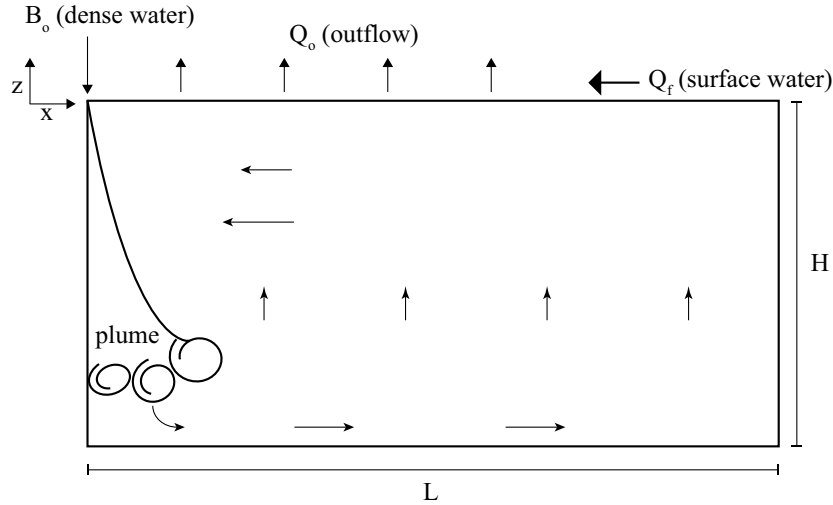


Figure 3.9: Simplified schematic of the experimental setup in figure 2.1. A line half-plume with specific buoyancy flux per unit spanwise width, B_0 , is introduced into a rectangular domain with aspect ratio $A = 0.5$. The outflow is assumed to span the whole length of the tank, ejecting fluid at a rate Q_o . The surface is forced via a horizontal throughput of waters at a rate Q_f .

3.4 Governing Physics

An idealized schematic of the experimental setup presented in chapter 2 is shown in figure 3.9. The vertical coordinate z is taken to be 0 at the plume origin and increasing upwards. The model is simplified to comprise of a line half-plume with specific buoyancy flux per unit spanwise width, B_0 , entering a rectangular domain along the left-hand endwall. The ejection of buoyancy from the interior is idealized to occur uniformly over the full length of the tank since the whole surface boundary is free to respond to the mechanism of diffusion. A flow is forced at the top boundary from right to left via a horizontal throughput of surface waters. Experiments reveal that the main, and potentially only, role of the imposed surface stress is to induce small-scale turbulence at the upper boundary, extending to d_{mix} . The theoretically relevant consequence of τ_{max} is then to create a spatially nonuniform diffusivity in the domain, which is a function of $S_{\delta f}$.

Velocity profiles as well as horizontal density gradient measurements support a largely one-dimensional structure of the flow and density field, respectively, in the

interior. Thus, a model in which the plume outflow is assumed to rapidly distribute in the horizontal is expected to provide an accurate approximation of the system (Manins 1979; Hughes et al. 2007). Analogous to the models of Hughes et al. (2007) and Baines and Turner (1969), the plume outflow is not explicitly modeled. Rather, the solutions are expected to verify that the fluid density in the plume matches that of the interior at the level of detrainment.

The governing model used for comparison with experiments is adopted from Hughes et al. (2007), who derive the "recycling box" model for horizontal convection by altering the filling–box flow equations of Baines and Turner (1969) to take into consideration an advection–diffusion balance of the density field in the interior of the domain. The model allows for a spatially varying turbulent diffusivity, which is necessary to correctly represent the developed region of mixing for experiments where $S_{\delta f} > 0.42$.

3.4.1 Derivation of the recycling box model equations

The inviscid plume equations for a line half–plume that sinks against a vertical boundary can be derived from the steady–state equations for mass, momentum, and density in the Boussinesq approximation,

$$\frac{\partial u}{\partial x} + \frac{\partial w}{\partial z} = 0, \quad (3.10)$$

$$u \frac{\partial u}{\partial x} + w \frac{\partial u}{\partial z} = -\frac{1}{\rho_0} \frac{\partial p}{\partial x}, \quad (3.11)$$

$$u \frac{\partial w}{\partial x} + w \frac{\partial w}{\partial z} = -\frac{1}{\rho_0} \frac{\partial p}{\partial z} - \frac{\rho}{\rho_0} g, \quad (3.12)$$

$$u \frac{\partial \rho}{\partial x} + w \frac{\partial \rho}{\partial z} = 0. \quad (3.13)$$

Following Hughes et al. (2007) and Baines and Turner (1969), the profiles of the mean vertical velocity, $\bar{W}(x, z)$ and density anomaly, $\rho_e(z) - \bar{\rho}(x, z)$ are assumed to be equal in width and approximated by a Gaussian distribution,

$$\bar{W}(x, z) = W_p(z) \exp \left[\frac{-x^2}{R^2(z)} \right], \quad (3.14)$$

$$\rho_e(z) - \bar{\rho}(x, z) = (\rho_e(z) - \rho_p(z)) \exp \left[\frac{-x^2}{R^2(z)} \right], \quad (3.15)$$

where W_p and $\rho_e - \rho_p$ are the mean vertical velocity and density anomaly on the plume axis, respectively, R is the plume thickness, x is the distance from the plume axis, and z is taken to be 0 at the plume origin and decreasing in the direction of flow in the plume. The subscripts p and e refer to parameters associated with the plume and environment, respectively.

In a turbulent plume, each variable may be decomposed into a mean and fluctuating component, e.g. $\rho = \bar{\rho} + \rho'$, where the overbar represents a temporal average. Experimental measurements have shown that the fluctuating and mean components scale comparably (Batchelor et al., 2000). Therefore, the variables in (3.10) – (3.13) may be replaced by their mean values, and the overbar dropped for clarity in deriving the plume equations. In the following derivations, the integral of the Gaussian profile (or its square) from (3.14)–(3.15) on a semi-infinite plane is commonly used, with exact solutions given by

$$\int_0^\infty \exp\left[\frac{-x^2}{R^2(z)}\right] dx = \frac{R\sqrt{\pi}}{2}, \quad (3.16)$$

$$\int_0^\infty \exp\left[\frac{-2x^2}{R^2(z)}\right] dx = \frac{R\sqrt{\pi}}{2\sqrt{2}}. \quad (3.17)$$

Integrating (3.10) in the horizontal plane across the plume,

$$\int_0^\infty \frac{\partial u}{\partial x} dx + \int_0^\infty \frac{\partial w}{\partial z} dx = u\Big|_0^\infty + \frac{d}{dz} \int_0^\infty w dx = 0. \quad (3.18)$$

Therefore,

$$\frac{d}{dz}[\sqrt{\pi}RW_p] = 2[u(0) - u(\infty)]. \quad (3.19)$$

The horizontal velocity at ∞ is equal to the entrainment velocity, U_e , into the plume. The entrainment constant, E , first introduced by Morton et al. (1956), relates the mean vertical velocity in the plume to this inflow velocity at the plume edge by the relation $U_e = EW_p$, in which E takes on a value of 0.1 when Gaussian profiles are employed (Baines and Turner, 1969). The horizontal velocity at $x = 0$ is equal to 0 due to no slip boundaries. The equation then becomes

$$\frac{d}{dz}[\sqrt{\pi}RW_p] = 2EW_p. \quad (3.20)$$

Integrating (3.12) across the plume,

$$\int_0^\infty \frac{\partial(uw)}{\partial x} dx + \frac{d}{dz} \int_0^\infty \frac{1}{2}w^2 dx = -\frac{1}{\rho_0} \int_0^\infty \frac{\partial p}{\partial z} dx - \int_0^\infty \frac{\rho_p}{\rho_0} g dx. \quad (3.21)$$

Outside the plume, $\rho = \rho_e(z)$ and $w = 0$; (3.12) then shows that the hydrostatic relation is obtained in the ambient,

$$\frac{\partial p}{\partial z} = -g\rho_e. \quad (3.22)$$

If the plume is assumed to be narrow relative to the domain, $p = p(z)$. To prove that this is indeed the case, (3.11) and (3.12) are nondimensionalized using

$$u \sim Uu^*, x \sim bx^*, z \sim Zz^*, w \sim \frac{UZ}{b}w^*, \quad (3.23)$$

where the scaling for w is derived from (3.10). Dropping asterisks for clarity, the components of the pressure gradient then scale like

$$\frac{U^2\rho_o}{b} \sim \frac{\partial p}{\partial x}, \quad (3.24)$$

$$U^2 \left(\frac{z}{b}\right)^2 \rho_o \sim \frac{\partial p}{\partial z}. \quad (3.25)$$

The ratio z/b is very large since $b \ll z$, so that the pressure term can be approximated as $p = p(z)$. Using this result, (3.21) may be re-written as,

$$[uw]_0^\infty + \frac{d}{dz} \int_0^\infty \frac{1}{2}w^2 dx = \frac{g}{\rho_0} \int_0^\infty \rho_e - \rho_p dx. \quad (3.26)$$

The first term on the left-hand side equates to 0 since $u = w = 0$ at $x = 0$ and $w = 0$ as $x \rightarrow \infty$. Substituting in the assumed profiles for the vertical velocity and density anomaly, the final equation describing conservation of momentum in the plume is

$$\frac{d}{dz} \left[\frac{RW_p^2}{\sqrt{2}} \right] = R \frac{g(\rho_e - \rho_p)}{\rho_0}. \quad (3.27)$$

Finally, as shown in Batchelor et al. (2000), conservation of buoyancy in the plume may be derived by taking the derivative of the buoyancy flux, B , which is defined as

$$B = \int_0^\infty wg \frac{\rho_e - \rho_p}{\rho_0} dx. \quad (3.28)$$

Therefore,

$$\frac{dB}{dz} = \frac{g}{\rho_0} \int_0^\infty \left[\frac{\partial w}{\partial z} (\rho_e - \rho_p) + w \frac{\partial(\rho_e - \rho_p)}{\partial z} \right] dx. \quad (3.29)$$

From continuity, $w_z = -u_x$, so that

$$\frac{dB}{dz} = \frac{g}{\rho_0} \int_0^\infty \left[-\frac{\partial u}{\partial x} (\rho_e - \rho_p) + w \frac{d\rho_e}{dz} - w \frac{\partial \rho_p}{\partial z} \right] dx. \quad (3.30)$$

In the plume, (3.13) gives $u\rho_x = -w\rho_z$, which results in

$$\frac{dB}{dz} = \frac{g}{\rho_o} \int_0^\infty \left[-\frac{\partial u}{\partial x}(\rho_e - \rho_p) + w \frac{d\rho_e}{dz} - u \frac{\partial(\rho_e - \rho_p)}{\partial x} \right] dx, \quad (3.31)$$

where ρ_e has been added to the last term on the right-hand side to create a total derivative, noting that it is solely a function of z . The first and last terms may then be combined and integrated to give

$$\frac{dB}{dz} = -\frac{g}{\rho_o} [u(\rho_e - \rho_p)] \Big|_0^\infty + \frac{g}{\rho_o} \frac{d\rho_e}{dz} \left(\int_0^\infty w dx \right). \quad (3.32)$$

Since $u = 0$ at $x = 0$ due to no slip boundaries and ρ_p approaches ρ_e as $x \rightarrow \infty$, the first term on the right-hand side equates to 0. Substituting in appropriate Gaussian profiles for B and w , the final equation describing conservation of buoyancy within the plume is

$$\frac{d}{dz} \left[\frac{RW_p(\rho_e - \rho_p)}{\sqrt{2\rho_0}} \right] = RW_p \frac{d}{dz} \left[\frac{g(\rho_e - \rho_0)}{\rho_0} \right], \quad (3.33)$$

where ρ_0 has been added to the last term on the right-hand side to match the plume equations of Hughes et al. (2007), noting that ρ_0 is not a function of z .

Because the plume exists in a confined space, two more equations are written to describe the interior flow. Conservation of volume is expressed as

$$\frac{\sqrt{\pi}}{2} RW_p = -LW_e, \quad (3.34)$$

where L is the box length and W_e is the interior vertical velocity. Generally, the length of the interior upwelling region varies with depth on account of the plume's increasing thickness. For the present analysis, it is assumed that the plume is narrow so that any vertical variation in the length of the outflow, $L(z)$, is neglected.

Classically, the interior density, ρ_e , has been taken to evolve in time and advection of the density field, ignoring any mixing or diffusion of the stratifying species (Baines and Turner, 1969). However, for the flow under consideration, advection of the density field by the plume must be balanced by vertical diffusion throughout the interior. If diffusion were neglected in the system, a steady-state flow would not be achievable, and the interior would eventually fill up with fluid at the plume density, thus expunging the initial buoyancy flux necessary to drive the circulation. The requisite equation describing the interior density field presented in Hughes et al. (2007) is therefore

$$W_e \frac{d\rho_e}{dz} = \frac{d}{dz} \left[\kappa^*(z) \frac{d\rho_e}{dz} \right]. \quad (3.35)$$

Here, $\kappa^*(z)$ is the diffusivity of the stratifying species, which can vary spatially within the domain. When mixing is present, $\kappa^*(z)$ takes on the role of a turbulent mixing coefficient, embodying any localized mixing in the flow that manifests itself as small-scale turbulence induced by an external mechanical forcing.

Boundary conditions

In practice, the line half-plume has a finite input of mass equal to Q_d through the stainless steel tubing; any initial momentum is assumed to be dissipated before entering the working volume. For the purpose of solving the equations, the input is assumed to be that of a pure plume driven solely by a buoyancy flux B_0 . A virtual source correction, discussed in § 3.4.3, is applied to the solutions in order to correct for the finite mass flux (Stewart et al., 2012).

The boundary conditions for the initial volume and momentum are therefore

$$(RW_p) \Big|_{z=0} = 0, \quad (3.36)$$

$$(RW_p^2) \Big|_{z=0} = 0. \quad (3.37)$$

The final boundary condition given in Hughes et al. (2007) asserts that the specific buoyancy flux at $z = 0$ must be equal to the diffusion of buoyancy out of the domain at the same level, ensuring that there is zero net input of buoyancy into the system. Assuming that experiments with a partial-depth circulation are indeed in a quasi steady-state, the flow is expected to evolve to the steady-state boundary condition,

$$B_0 = \frac{\sqrt{\pi}}{2\sqrt{2}} \left[\frac{RW_p g(\rho_e - \rho_p)}{\rho_0} \right] \Big|_{z=0} = -\frac{gL\kappa^*(0)}{\rho_0} \frac{d\rho_e(0)}{dz}. \quad (3.38)$$

3.4.2 Nondimensionalization

Following the nondimensionalization of Hughes et al. (2007), the dimensionless variables ζ, r, b_p, b_e, w_p , and w_e represent the vertical coordinate, the plume thickness, the specific buoyancy on the plume axis, the interior specific buoyancy, the vertical velocity of the plume, and the interior vertical velocity, respectively. The dimensionless

variables are then given by

$$z = 2^{-1/6} E^{-1/3} B_0^{-1/6} (\kappa^* L)^{1/2} \zeta, \quad (3.39)$$

$$R = 2^{5/6} E^{2/3} \pi^{-1/2} B_0^{-1/6} (\kappa^* L)^{1/2} r, \quad (3.40)$$

$$\frac{g(\rho_e - \rho_p)}{\rho_0} = 2^{1/3} E^{-1/3} B_0^{5/6} (\kappa^* L)^{-1/2} b_p, \quad (3.41)$$

$$\frac{g(\rho_e - \rho_0)}{\rho_0} = 2^{-1/6} E^{-1/3} B_0^{5/6} (\kappa^* L)^{-1/2} b_e, \quad (3.42)$$

$$W_p = 2^{1/3} B_0^{1/3} E^{-1/3} w_p, \quad (3.43)$$

$$W_e = 2^{1/6} E^{1/3} B_0^{1/6} \kappa^{*1/2} L^{-1/2} w_e, \quad (3.44)$$

Nondimensionalizing (3.20), (3.27), and (3.33) using (3.39)–(3.44), the nondimensional recycling box equations are

$$\frac{d}{d\zeta}(rw_p) = w_p, \quad (3.45)$$

$$\frac{d}{d\zeta}(rw_p^2) = rb_p, \quad (3.46)$$

$$\frac{d}{d\zeta}(rw_p b_p) = rw_p \frac{db_e}{d\zeta}, \quad (3.47)$$

and the nondimensional equations describing the interior flow (3.34)–(3.35) are

$$rw_p = -w_e, \quad (3.48)$$

$$w_e \frac{db_e}{d\zeta} = \frac{d}{d\zeta} \left[\gamma(\zeta) \frac{db_e}{d\zeta} \right], \quad (3.49)$$

where

$$\gamma = \frac{\kappa^*|_{\zeta}}{\kappa^*|_{\zeta=0}}. \quad (3.50)$$

The function $\gamma(\zeta)$ encompasses a spatially varying turbulent diffusivity normalized by the diffusivity at the surface, which is necessary to describe correctly the localized region of mixing generated by the surface stress. As defined in Hughes et al. (2007), the dimensionless specific buoyancy flux in the plume is defined as $\phi(\zeta) = rw_p b_p$, so that the boundary condition for B_0 given in (3.38) becomes

$$\phi(0) = \gamma(0) \left[-\frac{db_e(0)}{d\zeta} \right] = 1, \quad (3.51)$$

noting that b_e is always positive. In order to set up a system of equations to solve, the dimensionless conservation of volume equation given in (3.48) is substituted into the advection–diffusion equation in (3.49),

$$-rw_p \frac{db_e}{d\zeta} = \frac{d}{d\zeta} \left[\gamma(\zeta) \frac{db_e}{d\zeta} \right]. \quad (3.52)$$

This is equated with conservation of buoyancy in (3.47) to obtain

$$-\frac{d}{d\zeta} (rw_p b_p) = \frac{d}{d\zeta} \left[\gamma(\zeta) \frac{db_e}{d\zeta} \right], \quad (3.53)$$

which is rewritten as

$$-\frac{d}{d\zeta} (\phi) = \frac{d}{d\zeta} \left[\gamma(\zeta) \frac{db_e}{d\zeta} \right]. \quad (3.54)$$

The above expression is integrated from $\zeta' = 0$ to $\zeta' = \zeta$ to give,

$$-[\phi(\zeta) - \phi(0)] = \gamma(\zeta) \frac{db_e(\zeta)}{d\zeta} - \gamma(0) \frac{db_e(0)}{d\zeta}. \quad (3.55)$$

Applying the boundary condition in (3.51), the final result is

$$\phi(\zeta) = -\gamma \frac{db_e}{d\zeta} = -\frac{\gamma}{rw_p} \frac{d\phi}{d\zeta}. \quad (3.56)$$

The fourth–order system is thus comprised of (3.45)–(3.47), and (3.56). It should be noted that the system can be solved with only (3.45)–(3.46), and (3.56), since (3.47) is simply a product of the solutions; however, it is added to the system of equations to omit the step of post–integration of the ODE solution for ϕ . Defining $Q = rw_p$, the equations may be manipulated so the derivatives are in terms of ϕ , Q , Q^2/r , and b_e ,

$$\frac{d\phi}{d\zeta} = -\frac{Q\phi}{\gamma}, \quad (3.57)$$

$$\frac{dQ}{d\zeta} = \frac{Q^2}{r} \frac{1}{Q}, \quad (3.58)$$

$$\frac{d}{d\zeta} (Q^2/r) = \phi Q \frac{r}{Q^2}, \quad (3.59)$$

and

$$\frac{db_e}{d\zeta} = \frac{-\phi}{\gamma}, \quad (3.60)$$

subject to the boundary conditions $\phi(0) = 1$, $Q(0) = 0$, $Q^2/r(0) = 0$, and $b_e(0) = 0$. Written in terms of a function y to be solved in MATLAB where $y_1 = \phi$, $y_2 = Q$, $y_3 = Q^2/r$, and $y_4 = b_e$,

$$y'_1 = -\frac{y_1 y_2}{\gamma} \quad (3.61)$$

$$y'_2 = \frac{y_3}{y_2} \quad (3.62)$$

$$y'_3 = \frac{y_1 y_2}{y_3} \quad (3.63)$$

$$y'_4 = -\frac{y_1}{\gamma} \quad (3.64)$$

Obtainment of $\gamma(\zeta)$ per each experiment is discussed in § 3.4.4. The system of equations is solved in MATLAB using *ode15s*, with the relative tolerance and absolute tolerance set to 2.5×10^{-14} and 1×10^{-14} , respectively. The choice of ODE solver stemmed from its faster computation time in yielding the same results relative to using *ode45*, for example.

3.4.3 Virtual origin correction

On account of the finite mass flux of dense fluid entering the working volume, a virtual origin correction is implemented. The experimental plume originating from $z = 0$ with finite mass and buoyancy fluxes is equivalent to a line half-plume sinking from a virtual source located above the actual source at height $z = z_{vs}$, with buoyancy flux B_{vs} , and interior density ρ_{vs} . As first discussed in Stewart et al. (2012) for the experimental configuration under consideration, two limits exist for the virtual source: the “near source” and “far source” approximations, contingent on whether the actual source lies outside or inside the virtual boundary layer created by the virtual source, respectively. Stewart et al. (2012) found that the correction is nonnegligible when $\kappa^* < 10^2 \kappa_{mol}$, in which case the actual source lies outside of the virtual source boundary layer. Indeed, comparison of the virtual and actual source quantities reveals an insignificant change for experiments where regional mixing occurs. However, for experiments with $S_{\delta f} < 0.42$, corresponding to the limit $\kappa^* < 10^2 \kappa_{mol}$, the virtual source becomes dynamically important.

Source inside virtual boundary layer

Following Stewart et al. (2012), if the salt source lies within the virtual boundary layer, the equations describing the origin, $z_{vs,n}$, the specific buoyancy flux, $B_{vs,n}$, the reference density, $\rho_{vs,n}$, and the boundary layer thickness, $\delta_{vs,n}$ of the virtual source are

$$z_{vs,n} = 2^{-1/3} E^{-2/3} B_{vs,n}^{-1/3} Q_d, \quad (3.65)$$

$$B(0) \approx B_{vs,n} \exp \left[-2^{-4/3} E^{-2/3} B_{vs,n}^{-1/3} (\kappa^* L)^{-1} Q_d^2 \right], \quad (3.66)$$

$$\frac{g(\rho_{vs,n} - \rho_0)}{\rho_{vs,n}} \approx -B_{vs,n} (\kappa^* L)^{-1} z_{vs,n} \left[1 - 2^{-2/3} 3^{-1} E^{2/3} B_{vs,n}^{1/3} (\kappa^* L)^{-1} z_{vs,n}^2 \right], \quad (3.67)$$

$$\delta_{vs,n} = 2^{-1/6} E^{-1/3} B_{vs,n}^{-1/6} (\kappa^* L)^{1/2}, \quad (3.68)$$

where the subscript n reiterates that the values are calculated using the “near source” approximation. In order to obtain the necessary virtual source quantities, (3.66) is solved for $B_{vs,n}$ using the MATLAB *fzero* function, and the resulting value is substituted into (3.65), (3.67), and (3.68). This approximation is valid for $z_{vs,n} \leq \delta_{vs,n}$. For experiments which fall within this criteria, the calculated virtual source correction is verified as negligible due to the relatively small difference between actual and virtual source values.

Source outside virtual boundary layer

In the case of the salt source lying outside of the virtual boundary layer,

$$B_{vs,f} = \frac{(\psi_{max}^2 - Q_d^2)^2}{16E^2 \kappa^* LH^2}, \quad (3.69)$$

$$z_{vs,f} = 2^{-1/6} E^{-1/3} B_{vs,f}^{-1/6} (\kappa^* L)^{1/2} \left[0.903 + 2^{-11/6} E^{-2/3} B_{vs,f}^{-1/3} (\kappa^* L)^{-1} Q_d^2 \right], \quad (3.70)$$

$$\frac{g(\rho_{vs,f} - \rho(H))}{\rho_{vs,f}} = -1.28 \times 2^{-1/6} E^{-1/3} B_{vs,f}^{5/6} (\kappa^* L)^{-1/2}. \quad (3.71)$$

The boundary layer scaling $\delta_{vs,f}$ is found by substituting the value of $B_{vs,f}$ into (3.68). In the present analysis, these equations are used to calculate the quantities B_{vs} , ρ_{vs} , and z_{vs} in both the near source and far source limits, which are then applied to obtain the corrected theoretical predictions of the maximum streamfunction, maximum density difference, and boundary layer thickness, as well as to plot accurately the theoretical normalized buoyancy profiles in § 3.5. The calculated values are subject to large error

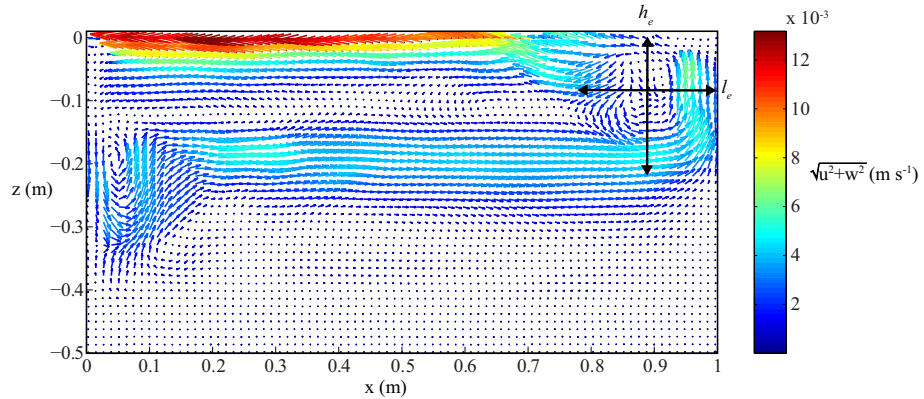


Figure 3.10: Velocity field for an experiment where $S_{\delta f} = 1.25$, obtained from PIV measurements. The horizontal and vertical extent of the eddy, l_e and h_e , respectively, are depicted by corresponding arrows. An estimate of the value of h_e is used in parameterizing $k^*(z)$.

due to the strong dependence on the streamfunction, ψ_{max} , which itself relies on the integration of velocity fields that contain regions of high density gradient. Analogous to the synthetic schlieren technique, steep density gradients shift the tracer particles in the area on account of the proportionally large refractive index gradients. These areas are avoided as best as possible in calculating ψ_{max} by initializing integration in the vertical at the opposite end from the upper boundary, where the density gradient is expected to develop.

3.4.4 Estimation of the turbulent diffusivity

In order to estimate the magnitude of the turbulent mixing coefficient in the region of mixing, $\kappa^*(z)$ is parameterized by the characteristics of the eddy that develops in the region. An example of such an eddy is shown in figure 3.10 for an experiment with $S_{\delta f} = 1.25$. The eddy characteristics are estimated from PIV data with the relation (Pope, 2000),

$$\kappa^*(z) \sim u^* h_e, \quad (3.72)$$

where h_e is the vertical extent of the eddy, and u^* is its rms velocity, defined as,

$$u^* = \sqrt{\text{rms}(u'^2) + \text{rms}(w'^2)}. \quad (3.73)$$

Here, u' and w' are deviations from the temporally averaged velocity field, $u' = u - \bar{u}$ and $w' = w - \bar{w}$. The fitted relation between $S_{\delta f}$ and $\kappa^*(z)$ is found to be

$$\kappa^*(z) = 5.07e^{-4} \times S_{\delta f}^{2.60} \text{ m}^2 \text{ s}^{-1}. \quad (3.74)$$

The scaling constant is determined from an empirical estimate of $\kappa^*(z)$ by considering the inverse problem and fitting measured buoyancy profiles to those calculated from the solution of the recycling box equations. The empirical estimate and eddy-derived $\kappa^*(z)$ differ by a mean constant value of $c = 0.0287$. Therefore, the final estimate of $\kappa^*(z)$ is

$$\kappa^*(z) = 5.07e^{-4}c \times S_{\delta f}^{2.60} \text{ m}^2 \text{ s}^{-1}. \quad (3.75)$$

In order to solve the system of equations in § 3.4.2 for experiments where mixing occurs, a piecewise constant profile is used to model the turbulent mixing coefficient, whereby $\kappa^*(z)$ takes on a fitted value given by (3.75) from the surface $z = 0$ until the depth of mixing, $z = -d_{mix}$, beneath which $\kappa^*(z) = \kappa_{mol}$, taken to be $1.38e^{-9}\text{m}^2\text{s}^{-1}$ (Benítez, 2009). This is written as,

$$\kappa^*(z) = \begin{cases} 1.45e^{-5} \times S_{\delta f}^{2.60} \text{ m}^2 \text{ s}^{-1} & \text{if } 0 \leq z \leq -d_{mix} \\ 1.38 \times 10^{-9} \text{ m}^2 \text{ s}^{-1} & \text{if } -d_{mix} < z \leq -H \end{cases}. \quad (3.76)$$

For experiments with no apparent mixing, the value of $\kappa^*(z)$ is $2.67e^{-9}\text{m}^2\text{s}^{-1}$, as estimated by Stewart et al. (2012) in the case of buoyancy-driven convection experiments with no external mechanical forcing. Entrainment into the plume and corresponding convective motions amplify κ^* from its molecular value in the case of a full-depth circulation. The final profile for $\gamma(\zeta)$ for each experiment is obtained by normalizing $\kappa^*(\zeta)$ with $\kappa^*(0)$, as per (3.50).

3.5 Results of the recycling box model

The system of equations in § 3.4.2 is solved numerically for each set of experiment parameters. Figure 3.11 displays normalized buoyancy profiles obtained from conductivity probe measurements (dashed lines) as well as corresponding solutions (solid lines) for various values of $S_{\delta f}$. In order to compare correctly the experiment den-

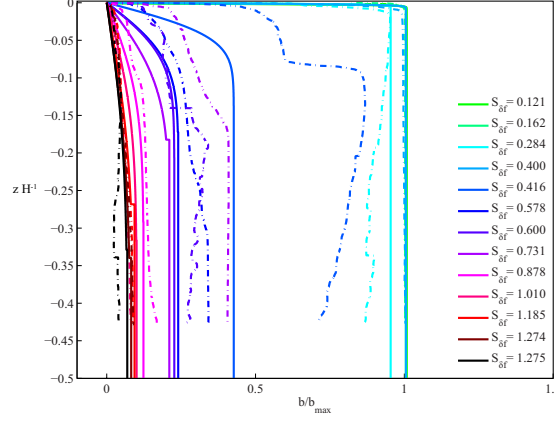


Figure 3.11: Normalized buoyancy profiles vs. normalized depth for select values of $S_{\delta f}$; dashed lines indicate conductivity probe measurements, and solid lines are the solutions to the plume equations. For $S_{\delta f} < 0.42$, the interior fluid density is very close to the maximum density input into the tank, so that the normalized buoyancy is very close to 1. As $S_{\delta f}$ is increased, the profiles indicate a freshening of the interior density, marked by a progressively smaller normalized buoyancy, as well as a thickening of the boundary layer.

sity profiles to those obtained by solving the system of equations, the first few mm of the conductivity profile which correspond to the surface freshwater layer are discarded; the boundary between this layer and the working volume is discernible from the profile shape. For experiments with $S_{\delta f} > 0.42$, the minimum density in the tank is then taken to be the interfacial density at the boundary of the working volume and freshwater surface layer. Because mixing occurs very near the freshwater source, the minimum fluid density entering the volume is no longer that of freshwater, as discussed in § 3.2. Therefore, the normalized buoyancy is defined as

$$\frac{b}{b_{\max}} = \frac{g(\rho(z) - \rho_i)/\rho_i}{g(\rho_d - \rho_i)/\rho_i} = \frac{\rho(z) - \rho_i}{\rho_d - \rho_i}, \quad (3.77)$$

where ρ_i is the interfacial density, equal to that of freshwater for experiments where $S_{\delta f} < 0.42$. Generally, as $S_{\delta f}$ is increased, both the measurements and theoretical predictions show that the fluid density in the environment becomes fresher at all measured depths. Also evident from figure 3.11 is the gradual thickening of the boundary layer for increasing $S_{\delta f}$, as the upper layer becomes more homogenized by the localized region of turbulence. Even though there is considerable noise in the measured profiles, the approximate shape is recovered by the majority of the solutions to the plume equations.

Table 3.2: Table summarizing asymptotic solutions to plume equations. For $S_{\delta_f} < 0.42$, the quantities match exactly those predicted by the recycling box model of Hughes et al. (2007). For $S_{\delta_f} > 0.42$, the solutions become functions of d_{mix} and therefore of S_{δ_f} ; the mean and standard deviation for each quantity are presented.

	$S_{\delta_f} < 0.42$	$S_{\delta_f} > 0.42$
$\Delta b_e(\zeta_h) =$	1.28	1.29 ± 0.011
$\delta_{0.95} =$	2.06	2.00 ± 0.15
$w_e(\delta_{0.95}) =$	1.83	1.79 ± 0.114

The dimensionless solutions to key quantities, including the maximum density difference, $\Delta b_e(\zeta_h)$, the thickness of the boundary layer that incorporates 95% of the density anomaly, $\delta_{0.95}$, and the corresponding interior vertical velocity at the boundary layer, $w_e(\delta_{0.95})$, are shown in table 3.2, where $\zeta_h = \delta_{bl}^{-1} h$ is the effective dimensionless box depth. The scaling for the boundary layer thickness, $\delta_{0.95}$, is retrieved by setting ζ to 1 in the parameterization of z from § 3.4.2. All values for experiments with $S_{\delta_f} < 0.42$ match exactly those predicted by the recycling box model of Hughes et al. (2007), valid in the limit $\phi \rightarrow 0$. The asymptotic approximations vary at most 0.01% from the mean value. For the explored range of values when $S_{\delta_f} > 0.42$, the solutions for $\Delta b_e(\zeta_h)$ and $\delta_{0.95}$ vary within 0.85% and 7.5% of the mean, respectively; the mean and standard deviations for each quantity are given in table 3.2. The larger deviation in the boundary layer thickness is discussed further in § 3.6.

In order to better compare to results of Stewart et al. (2012), the solutions to the streamfunction, maximum density difference, and boundary layer thickness in terms of the turbulent diffusivity, $\kappa^*(\zeta)$ are therefore (Hughes et al., 2007),

$$\psi_{max} = 2E^{1/2} \left(\frac{H}{L} \right)^{1/2} B_{vs}^{1/4} L^{3/4} \kappa^{*1/4}, \quad (3.78)$$

$$\left. \frac{\rho_e - \rho_0}{\rho_0} \right|_{max} = C_{\Delta b_e} \times 2^{-1/6} E^{-1/3} g^{-1} L^{-1/2} B_{vs}^{5/6} \kappa^{*-1/2}, \quad (3.79)$$

$$\delta_{0.95} = C_{\delta_{0.95}} \times 2^{-1/6} E^{-1/3} B_{vs}^{-1/6} L^{1/2} \kappa^{*1/2}, \quad (3.80)$$

where $C_{\Delta b_e}$ and $C_{\delta_{0.95}}$ are the solutions predicted by the theoretical model, and B_{vs} is the specific buoyancy flux at the virtual source. Experiment measurements (circles) along with least squares (dashed lines) and theoretical fits (solid lines) are displayed

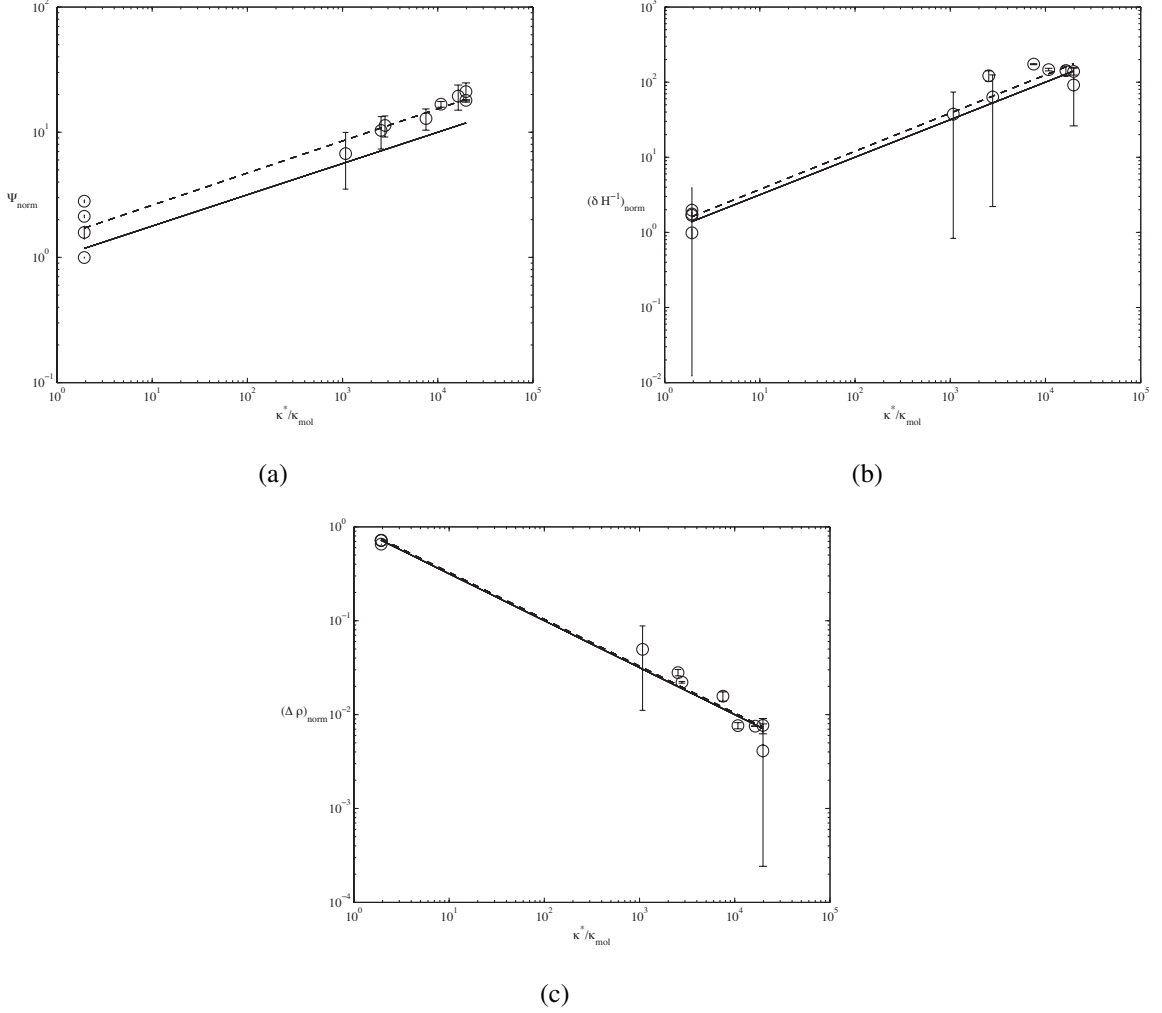


Figure 3.12: Summary of key experimental quantities (circles) as well as corresponding least squares fits (dashed lines) and recycling box model predictions (solid lines). The subscript *norm* reiterates that the measured values are normalized by their theoretical analogues. All error bars are estimated from averaging two data sets recorded per experiment, taken approximately 4 hrs (or half a filling timescale) apart. (a) plots the normalized streamfunction as a function of $\kappa^* \kappa_{mol}^{-1}$. The least-squares fit is $\psi_{norm} = 1.446 \times (\kappa^* \kappa_{mol}^{-1})^{0.2567}$, and the corresponding theoretical prediction is $\psi_{norm,t} = 1 \times (\kappa^* \kappa_{mol}^{-1})^{0.25}$. (b) plots the normalized boundary layer thickness, calculated from conductivity probe profiles. The fitted and theoretical solutions are $(\delta_{bl}H^{-1})_{norm} = 1.158 \times (\kappa^* \kappa_{mol}^{-1})^{0.5078}$ and $(\delta_{bl}H^{-1})_{norm,t} = 1 \times (\kappa^* \kappa_{mol}^{-1})^{0.5}$, respectively. (c) plots the measured maximum density difference from conductivity probe data as well as the corresponding fitted solution, $\Delta\rho_{norm} = 1.037 \times (\kappa^* \kappa_{mol}^{-1})^{-0.5003}$ and theoretical prediction, $\Delta\rho_{norm,t} = 1 \times (\kappa^* \kappa_{mol}^{-1})^{-0.5}$. Four points nearly overlap each other in the limit $\kappa^* < 10^2 \kappa_{mol}$.

in figure 3.12. All experiment values are normalized by their corresponding solution predictions given in (3.78)-(3.80), due to the variability in solutions for $S_{\delta f} > 0.42$.

Errors in the calculations of the streamfunction and density arise from averaging two recorded data sets per each experiment, at half a filling timescale apart. For experiments with $S_{\delta f} < 0.42$, errors in the density measurement are low, as evidenced by the overlapping conductivity profiles in figure 3.4(d). However, once localized mixing occurs, and specifically for experiments near the transition point, the conductivity profiles are relatively noisier, made evident by the magnitude of the error bars in figure 3.12(b). As discussed briefly in § 3.2, the eddying nature of the flow field is likely causing $\mathcal{O}(s)$ fluctuations picked up in the conductivity profile. At the extent of the conductivity probe's traverse, the flow tended to be more stable.

In general, the fitted lines for the streamfunction and boundary layer thickness both suggest that the experimentally measured quantities are larger than predicted by the solutions to the equations. For low values of $S_{\delta f}$, the maximum streamfunction is somewhat scattered. The results are sensitive to the virtual source origin correction of B_0 , which is somewhat a challenge to calculate, as small errors in the prediction of the maximum streamfunction are accentuated in the calculation of B_{vs} , and consequently all other virtual source–corrected quantities. Other possible reasons for the discrepancy are discussed in § 3.6.

3.6 Discussion

At the onset of each experiment, the plume is entering a homogeneous, freshwater environment, wherein it necessarily maintains sufficient specific buoyancy and momentum to sink the full depth of the volume. Qualitative observations of the equilibration process verify that the plume penetrates the full depth of the volume on its initial descent, with mixing constrained to the upper surface. Because the plume exists in a confined space, its outflow inevitably interacts with the region of developed turbulence. If stabilizing mechanisms such as viscosity and stratification are too weak to suppress instabilities near the surface, turbulent motions mix the surrounding fluid. The result is a mixed layer that increases in depth as the flow evolves, ultimately extending to d_{mix} ,

an equilibrium depth. During this transient adjustment, the plume is continually subject to an input of stabilizing buoyancy in the form of fresher fluid, which in turn creates a buoyancy excess, resulting in a weakened plume that loses its momentum flux before it is able to penetrate the full domain. Consequently, the plume finds itself in a stratified environment which, below a certain level, is denser than itself, causing it to detrain at variable depth into the tank interior.

The variability in the boundary layer thickness reveals that the value is a relatively strong function of d_{mix} . More specifically, the boundary layer thickness is altered if the depth of mixing is close to, or less than the boundary layer thickness that would otherwise develop if mixing occurred through the full depth of the volume. Consider a full-depth circulation subject to turbulent mixing through the whole domain, with corresponding boundary layer thickness, δ_0 . If turbulent mixing becomes confined to a region shallower than δ_0 , the resulting boundary layer will become thinner than δ_0 . The density difference between the upper mixed layer and underlying stagnant region develops in such a way that at the base of the layer, the density is automatically at least 95% of the maximum density anomaly in the volume. In this sense, the mixed layer depth is responsible for setting the boundary layer thickness. On the other hand, if turbulent mixing is confined to a distance beyond the boundary layer that is less than approximately 50% of δ_0 , the resulting boundary layer will thicken; past this threshold, the boundary layer thickness becomes independent of the depth of mixing.

Figures 3.13(a) and 3.13(b) display the variation in the solutions to the boundary layer thickness, $C_{\delta_{0.95}}$, as a function of mixing depth. All experiments are plotted at each point to highlight the collapse of the boundary layer thickness solutions. The mixing depth is written as a fraction of the boundary layer thickness, δ_0 , that would develop in the case of uniform mixing through the volume. Therefore, the horizontal axis in figure 3.13(a) ranges from a mixing depth that is exactly equal to δ_0 at 0, to a mixing depth that is 50% larger than δ_0 at 0.5. Additionally, the horizontal axis in figure 3.13(b) corresponds to a mixing depth which is becoming up to 10% shallower than δ_0 , at -0.1. The plots indicate that if the mixing depth is downstream of the boundary layer but sufficiently close to it, the thickness of the layer will increase at most 2% from its original depth. If the mixing depth is far enough removed downstream, the boundary layer

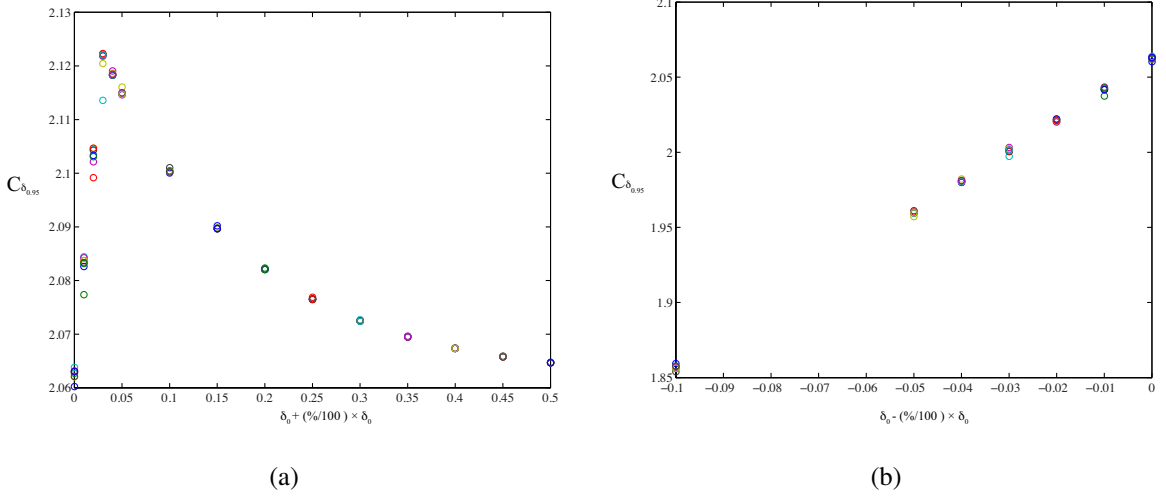


Figure 3.13: (a) and (b) plot the solutions to the dimensionless boundary layer thickness for all experiments as a function of d_{mix} . The horizontal axis represents d_{mix} as a fraction of the boundary layer thickness, δ_0 , that would develop if mixing was applied uniformly to the whole volume. (a) explores the case where $d_{mix} \geq \delta_0$, and (b) explores $d_{mix} \leq \delta_0$.

thickness is independent of the depth of mixing. The most stark change occurs when the mixing depth is thinner than δ_0 ; in this case, the boundary layer thickness is set by the mixing depth. A decrease in the boundary layer thickness will have implications on the resulting flow field. The streamfunction is expected to decrease as less water is entrained by the plume. Additionally, the top-to-bottom density difference is expected to decrease. In the experiment set, the last three data points correspond to decreased boundary layer thicknesses on account of the mixing depth being thinner than the expected boundary layer thickness. The predicted values coincide well with thicknesses determined from experiments.

In general, figure 3.12(b) reveals that the measured boundary layer thickness is larger than predicted by the theory. This is consistent with a larger streamfunction, which is also evident in the experiments. However, the mechanism responsible for thickening the boundary layer and consequently increasing the streamfunction is unclear. In fact, the increased streamfunction is extremely peculiar. Its theoretical calculation relies on entrainment through the full depth of the volume, which would increase with increasing depth since $\psi_{max} \propto H$. During data acquisition in the experiments with $S_{\delta f} > 0.42$,

the plume did not penetrate the full volume, but the measured streamfunction is still approximately 10-20 times the theoretical value. The experiment with the shortest penetration depth of 6.52 cm contains a measured streamfunction which is approximately 7 times its theoretical value while only penetrating 13% of the domain. If this is not due to measurement error, then it may be a result of inhibited local upwelling due to the surface stress, which would act to thicken the boundary layer.

The formation of a laminar sublayer on the wall adjacent to the plume outflow permits dense water to penetrate past the plume detrainment depth, and eject dense fluid into the stagnant abyss. To date, there is no literature which reports the existence of a laminar sublayer forming against an endwall adjacent to a line half-plume. However, the recorded data consistently supports its maintenance, even after the plume source tubing configuration was adjusted on approximately three separate occasions. Because it resupplies dense fluid into the stagnant region of the flow, diffusion cannot erode away the interface between the plume and stagnant interior. Maintenance of a steady-state partial-depth circulation could then be achieved if the advection of buoyancy flux by the laminar sublayer is exactly matched by diffusion across the interface separating the circulation and underlying stagnant region, such that the horizontally averaged net buoyancy flux at any given depth is zero.

3.7 Conclusions

A series of experiments have been performed in which a surface buoyancy-forced circulation, driven by salt fluxes, is subject to a surface stress in the form of a freshwater layer flowing along the same boundary at which the convection is forced. When the ratio of mechanical to buoyancy forcing, $S_{\delta f}$, exceeds 0.42, a region of mixing develops near the freshwater inlet, which thereafter deepens linearly with increasing $S_{\delta f}$. The resulting turbulent mixing coefficient, $\kappa^*(z)$, is no longer uniform in the vertical, and must be scaled by the characteristics of the developed eddy in the turbulent region. The value of $\kappa^*(z)$ is found to approximately scale with $S_{\delta f}^{2.6}$. The depth of the mixing region develops until it reaches an equilibrium level, which is estimated well by the corresponding ratio of mechanical to buoyancy forcing. During its spatial de-

velopment, the mixing region imparts a temporal input of stabilizing buoyancy into the plume, causing it to weaken and consequently intrude into the interior at partial depth. Furthermore, a laminar sublayer develops on the left-hand endwall adjacent to the plume outflow, supplying dense plume fluid into the relatively quiescent interior. Generally, the partially sinking plume does not exhibit signs of penetrative convection at the interface of the plume outflow and underlying stagnant region, which would otherwise reduce the timescale required to obtain equilibrium. As such, it is unclear if the partial-depth circulations are in steady-state. Due to the existence of a laminar sublayer, there could potentially be no net buoyancy flux through any level in the fluid, and therefore the system may be in fact have reached a well-defined equilibrated flow. However, there is no way of knowing if this is the case using the acquired set of experiment data. Additional experiments, specifically ones in which the convection is driven by a thermal forcing, are required, because they can be run for the long diffusive timescale of the system, ensuring that a steady state is acquired. The mechanism of penetrative convection also requires further investigation on order to determine under what conditions will horizontal convection reestablish itself on the timescale observed in Vreugdenhil et al. (2015) following a net input of buoyancy flux into the plume.

The solutions of the recycling box model equations with nonuniform $\gamma(\zeta)$ agree well with key flow characteristics, supporting the main result that the order-one effect of a surface stress imposed in the same direction as the flow generated by surface buoyancy fluxes is to impart mechanical energy into the circulation by creating a spatially nonhomogeneous turbulent diffusivity in that limit that $S_{\delta f} > 0.42$. The model can be improved by using a more accurate function than piecewise constant to describe the vertical profile of $\kappa^*(z)$. The solutions for the maximum streamfunction and boundary layer thickness are generally larger than their theoretical counterparts. A thicker boundary layer is consistent with an increase in the streamfunction, and boundary layer thicknesses approximately 20% greater than the corresponding theoretical prediction have been reported in experiments where mixing is confined to the upper portion of the domain using the same experimental setup as in the current study (Vreugdenhil et al., 2015). It is yet unclear why this is the case for confined mixing, since figure 3.13(a) suggests an increase in thickness by at most 2%, and only occurring if the mixing depth

is just at the right location relative to the expected boundary layer thickness. Alternately, Stewart et al. (2012) report thinner-than-predicted boundary layers for full-depth mixing, once again using the same configuration.

The experiment results may be generally applied to the oceans and other large bodies of water subject to wind stress. If strong enough, the wind stress can induce regional turbulence extending from the surface to some intermediate depth. This small-scale turbulence will act to homogenize the layer in which it persists, consequently deepening the thermocline and altering the characteristics of the upper ocean. Additionally, near sinking regions, the mixed layer will modify the plume density through the entrainment of relatively fresher fluid, resulting in a weakened plume that intrudes at partial depth. If the circulation is exposed to an oscillatory mechanical forcing for timescales on the order of the system's natural response timescale, any changes in magnitude and/or direction of the forcing can lead to changes in the bulk stratification, as the plume would once again alter its intrusion depth to accommodate the net supply of (de)stabilizing buoyancy. A series of such events can lead to complicated stratification profiles that extend beyond the depth of mixing induced by the surface stress, which is itself a function of the magnitude of the stress. The clearest example of this scenario is shown in figure 3.6(a), where the superposition of experiments all subject to variable forcing have resulted in a comprehensive stratification profile much more complicated than one expected for a solely buoyancy–driven system. Additionally, near topographical boundaries, a turbulent sinking plume may be accompanied by a laminar sublayer, further modifying the stratification profile by allowing dense fluid to reach deeper levels. The overarching theme is that changes in the upper boundary layer can be communicated to the interior through the plume, altering the global flow structure in response to a long-term perturbation.

Parts of chapter 3 are currently being prepared for publication under the citation: Matusik, K. E. & Llewellyn Smith, S. G. “The response of surface buoyancy flux–driven convection to localized mechanical forcing on the same boundary”. The thesis author is the primary investigator and author of this paper. The work was funded by NSF Grant OCE1259580.

Chapter 4

Experiments with competitive mechanical and buoyancy forcing imposed on the surface

A total of 29 experiments have been carried out with a clockwise buoyancy–driven convective cell, such that the stress is acting against the circulation at the surface. The experimental setup corresponds to the red dashed line for the dense source configuration in figure 2.1. The freshwater volumetric flow rate per spanwise width, Q_f , for the set is in the range of $16.30\text{--}191.65 \text{ mm}^2 \text{ s}^{-1}$. A summary of the experiments and relevant quantities are presented in table 4.1, organized according to their respective $S_{\delta f}$ value. The uncertainty in calculated $S_{\delta f}$ values is at most 20%, stemming from systematic error associated with measuring the freshwater volumetric flow rate as well as the freshwater boundary layer thickness. The experiment set maintains buoyancy fluxes in the range $B_0 = (1.94 - 5.50) \times 10^{-6} \text{ m}^3 \text{s}^{-3}$, yielding flux Rayleigh number values of $Ra_B = (1.09 - 3.09) \times 10^{18}$ and a constant Pr of 678, calculated using molecular values for diffusivities.

Video recording of dye visualizations for the experiment set was typically limited to 25 min. In order to gain a more thorough understanding of the longtime flow patterns, additional experiments focused solely on dye visualization of the developed plume outflow spanning an interval of 4 hrs were performed, and are not listed in ta-

Table 4.1: Summary of experiments in which a surface stress is acting against a buoyancy driven circulation at the surface. The velocity u_f is the flow rate of the freshwater layer, defined in chapter 3. $\Delta\rho_{max}$ is the maximum density difference between the dense and freshwater sources. $\delta_{0.95}$ is the mean thickness of the boundary layer that encompasses 95% of the maximum density difference in the working volume. For experiments with no recorded value of $\delta_{0.95}$, the interface between the freshwater surface layer and underlying circulation is indiscernible, thus an accurate estimate of the boundary layer thickness cannot be made.

Exp	u_f (mm s ⁻¹)	$\Delta\rho_{max}$ (kg m ⁻³)	S_{δ_f}	$\delta_{0.95}$ (mm)
1	1.80	11.96	0.14	1.83
2	3.59	31.86	0.17	82.50
3	4.27	31.45	0.20	180.6
4	4.53	31.89	0.21	15.75
5	3.98	21.13	0.23	—
6	3.43	13.44	0.25	3.96
7	3.73	11.99	0.28	2.64
8	4.04	12.04	0.30	3.56
9	5.34	22.08	0.30	4.27
10	6.46	31.90	0.30	106.58
11	6.95	21.78	0.39	1.22
12	8.78	31.74	0.41	94.90
13	8.98	31.10	0.42	2.84
14	5.92	12.35	0.45	4.98
15	11.03	31.44	0.51	166.12
16	10.20	22.26	0.57	—
17	7.90	12.86	0.60	4.78
18	11.36	21.78	0.64	—
19	12.05	22.12	0.67	55.98
20	13.04	21.81	0.74	111.76
21	13.90	21.89	0.77	93.98
22	14.33	22.18	0.80	6.71
23	10.63	12.76	0.80	50.09
24	15.53	21.73	0.87	137.26
25	19.43	32.37	0.89	158.09
26	21.18	32.02	0.97	42.06
27	19.11	22.28	1.06	167.23
28	14.99	12.28	1.15	9.04
29	17.22	12.19	1.32	22.56

ble 4.1. The range of considered $S_{\delta f}$ values offers insight into a variety of flow regimes, each with its own complicated flow patterns. §§ 4.1 and 4.2 summarize the general qualitative and quantitative motifs in each regime, with discussion of flow stability and the onset of turbulence in § 4.2.1. Scaling arguments are presented in § 4.3 and applied to experiment results, with comparison to numerical simulations of Hazewinkel et al. (2012). § 4.4 and § 4.5 summarize findings and discuss their relevance to the ocean overturning circulation.

4.1 Qualitative results

Dye visualizations of the plume outflow for experiments with $S_{\delta f} < 0.20$ and $\rho_d > 1010 \text{ kg m}^{-3}$ reveal that the surface stress acts passively on the boundary and an equilibrated full-depth circulation is obtained. Within this parameter space, the flow exhibits horizontal convection features akin to those observed in related experiments (e.g. Mullarney et al. 2004; Stewart et al. 2012), including a narrow and turbulent endwall plume which sinks to the tank base and subsequently outflows into the interior with visible entrainment at all depths. The circulation is closed via broad upwelling back to the forcing boundary. Figure 4.1 displays the steady-state flow structure for a typical experiment unaffected by the surface stress, in which $S_{\delta f} = 0.17$. Tracer dye is added to the dense source in order to track the plume’s evolution. Figure 4.1(a) shows a snapshot of the flow field after 15 min, revealing a confined endwall plume that penetrates the full volume. The corresponding quiver plot in figure 4.1(b) exposes a highly asymmetric circulation featuring a distinct vortex eye offset to the bottom right-hand corner where the plume detrains; the largest velocities are constrained to the plume region.

For $0.20 < S_{\delta f} < 0.51$, the flow is responsive to the surface stress, and a cyclical, unsteady flow pattern is evident. The plume no longer adheres to the right-hand endwall, but rather is smeared laterally near the surface by the stress. Consequently, the plume outflows into the working volume at an angle, now subject to entrainment from all sides. The plume outflow recirculates on itself, gradually acquiring enough negative buoyancy to sink to the base of the domain, after which the convective cell is shut down, the plume returns to a shallower depth, and the process is repeated.

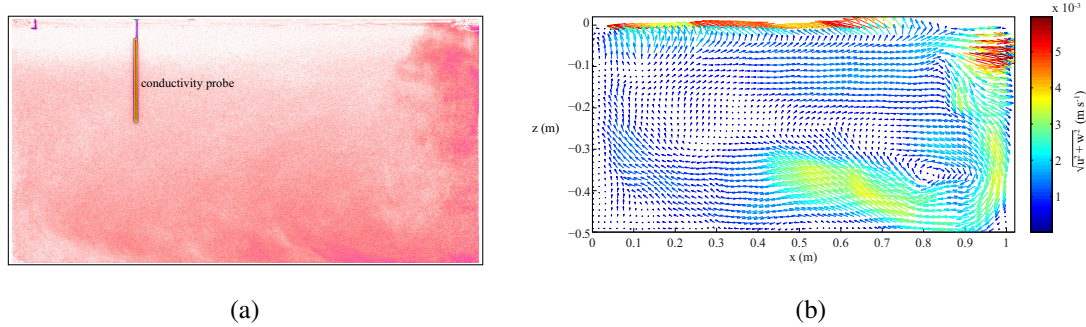


Figure 4.1: (a) Dye visualization of the equilibrated flow field for an experiment where $S_{\delta f} = 0.17$. KMnO₄ crystals are mixed into the dense source fluid in order to track the plume outflow. (b) plots the corresponding velocity map of the flow, revealing an asymmetric circulation driven by a plume that penetrates the full domain. The magnitude of the vectors are stretched by a factor of 5 for improved visibility. The colormap corresponds to the velocity magnitude. The experiment has been running for approximately 52 hrs.

Figure 4.2 displays a time-averaged quiver plot and corresponding contour plot of an experiment with $S_{\delta f} = 0.30$, obtained by averaging PIV measurements over a 20 s interval to resolve eddying features. In place of a single vortex eye in the velocity field shown in figure 4.2(a), the plume outflow is composed of smaller-scale eddies, and directed away from the endwall. Also evident is a region of flow directed into the plume in the top right-hand corner, signifying strong recirculation into the plume. The filled contour plot in figure 4.2(b) reveals a counterclockwise, stress driven circulation overlying clockwise convecting cells.

At the lower end of $S_{\delta f}$ values within this regime, the plume is quicker to convect the full depth of the tank, as the relatively larger buoyancy flux allows it to penetrate deeper into the volume before succumbing to surface stress effects. On the opposite end of the regime, the flow evolves slowly as the plume is forced to recirculate on itself and consequently does not escape the region of influence of the stress. Two dye images in figure 4.3 illustrate this point more clearly. Figures 4.3(a) and 4.3(b) have respective $S_{\delta f}$ values of 0.42 and 0.30 and plume densities $\rho_d = 1029$ and 1020 kg m^{-3} . The image stills are both taken after the dye has circulated for 500 s. The plume experiencing a smaller $S_{\delta f}$ value of 0.30 is able to advance further in 500 s than a denser plume at $S_{\delta f} = 0.42$ in the same amount of time. The complicated flow pattern is reminiscent of

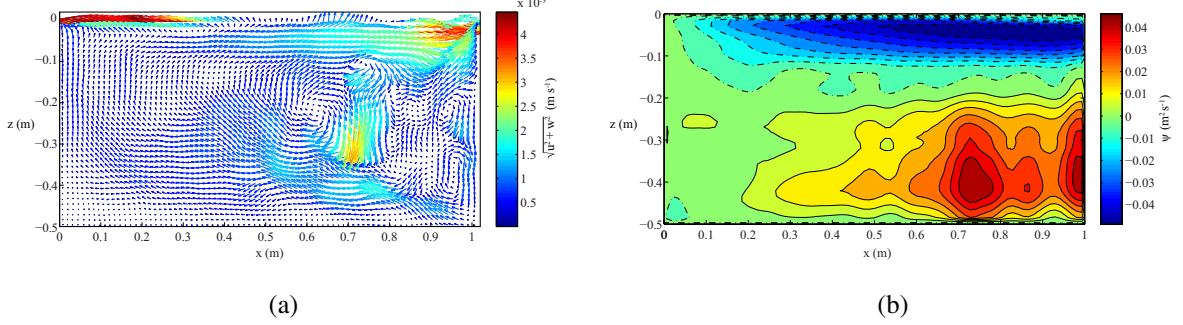


Figure 4.2: (a) Velocity field for an experiment with $S_{\delta f} = 0.30$, where the buoyancy–driven cell is affected by the surface stress. The magnitude of the vectors are stretched by a factor of 7 for improved visibility, and the colormap corresponds to the velocity magnitude. The plume outflow is deflected toward the center of the domain, with a more chaotic eddying outflow than typically observed for solely buoyancy–driven systems, such as the one shown in figure 4.1(b). (b) shows the corresponding contour plot of the streamfunction ψ . The colormap represents the magnitude of the streamfunction. Solid contours are $\psi > 0$ and dashed contours are $\psi < 0$, corresponding to clockwise and counterclockwise circulation, respectively.

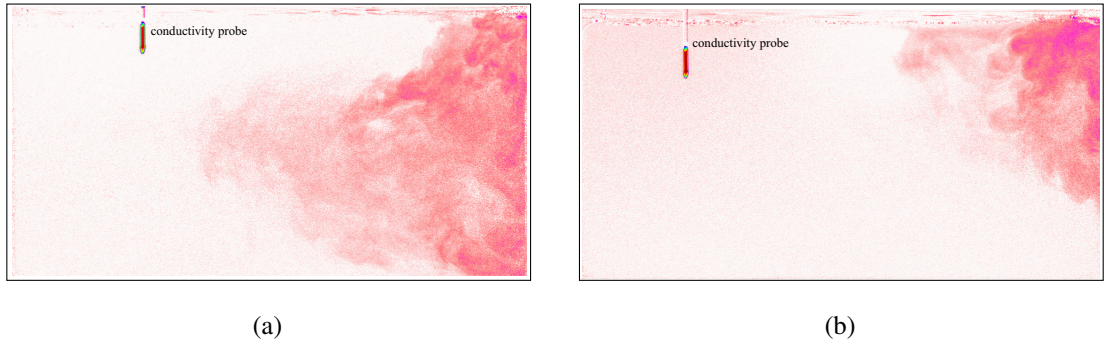


Figure 4.3: (a) Dye visualization of an experiment with $S_{\delta f} = 0.30$ and $\rho_d = 1020 \text{ kg m}^{-3}$. This is compared to (b), a dye image of an experiment with $S_{\delta f} = 0.42$ and $\rho_d = 1029 \text{ kg m}^{-3}$. The time elapsed after dye is introduced into the volume is 500 s for both experiments. Even though (b) contains a larger plume density, the advancement of the plume is hindered by the stronger surface stress, relative to the experiment in (a).

one detailed in numerical simulations of Hazewinkel et al. (2012), performed at $Pr = 10$, $Ra = 64 \times 10^7$ and intermediate stress levels. The authors report a regime in which the flow cycles through intervals of convection and inversion, whereupon a counter-rotating cell is formed at the surface, increasing in strength until plumes suddenly form to release built-up potential energy, consequently reestablishing convection. Once the potential energy is released, the cycle repeats. Figure 4.2(b) reveals the inversion leg of this cycle, where a counterclockwise cell has formed above the buoyancy–driven circulation. Once the plume entrains sufficient negative buoyancy, it will sink to the bottom, being replaced by fluid which is not as dense and therefore more responsive to stress effects.

At $S_{\delta f} \approx 0.51$, the flow experiences mixing in the boundary layer near the fresh water source. For experiments which exhibit this localized turbulence, the density in the interior freshens at all depths. Evidence of this freshening may be seen in normalized density profiles in figure 4.7. Qualitatively, the stress establishes a shallow counterclockwise cell at the surface that competes with the underlying circulation. On account of the net buoyancy flux input caused by mixing with the freshwater layer, the plume detrains at partial depth, resulting in finger–like intrusions below the surface layer. Intrusions form as the stressed layer on the surface effectively drags fluid beneath it, supporting a counterclockwise cell. Simultaneously, plume detrainment tends to occur below this layer, and flow in a clockwise sense. The result is a complicated circulation pattern featuring a tug–of–war of sorts between the layer dragged by the surface stress and the underlying cell. Figure 4.4(a) displays a dye visualization of an experiment which falls into this regime.

Experiments with sufficiently high $S_{\delta f}$ values (observed for $S_{\delta f} \approx 0.87$), support a laminar sublayer that allows fluid to penetrate the full depth of the volume. Figure 4.4(b) is a snapshot taken 2 hrs after dye is introduced into the dense source drum. The flow in the upper layer appears to switch direction periodically, supporting internal waves at the interface between the upper and lower cells. This regime features a two–cell circulation, in which the upper shallow cell is recirculating in the counterclockwise sense, and therefore mechanically forced, while the deeper lower cell is buoyancy–driven and circulates in a clockwise direction.

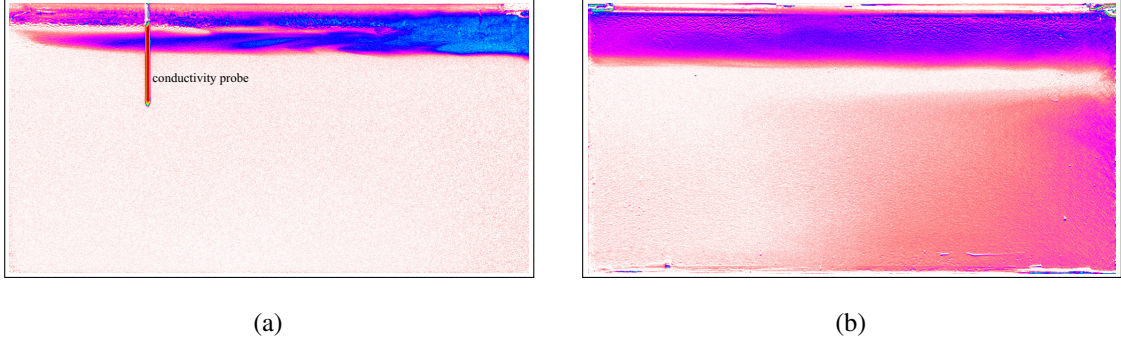


Figure 4.4: (a) Dye image of an experiment with $S_{\delta f} = 0.77$ where regional mixing is present near the surface. Plume evolution is monitored for 25 min, with the image taken at the end of the interval. (b) shows the plume evolution after 2 hrs for a flow where $S_{\delta f} = 1.21$.

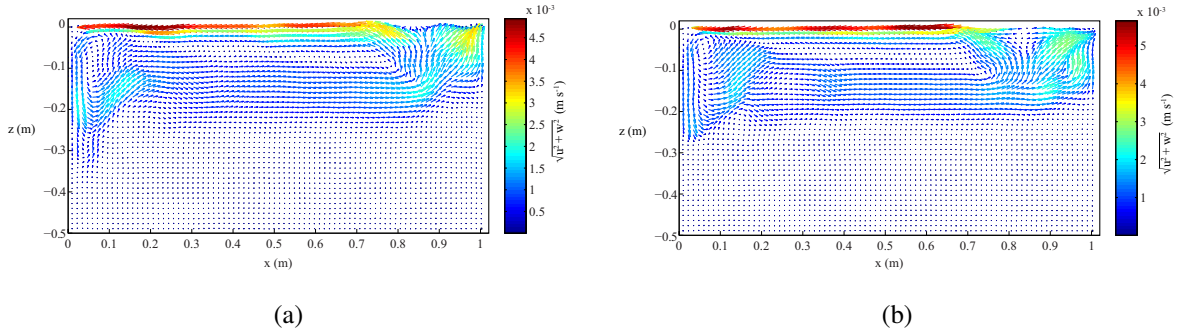


Figure 4.5: (a) and (b) plot the long-time velocity field for an experiment with $S_{\delta f} = 0.14$, obtained from PIV measurements. The time step between the images is 4 hrs. The magnitude of the vectors are stretched by a factor of 5 for improved visibility. The colormap gives the velocity magnitude.

4.1.1 Flow features for a low density plume

For experiments where the plume density is $\rho_d \approx 1010 \text{ kg m}^{-3}$, the circulation is affected by the surface stress for all explored values of $S_{\delta f}$. Figure 4.5 plots the flow field for an experiment with $S_{\delta f} = 0.14$ and $\rho_d = 1010 \text{ kg m}^{-3}$ for both sets of data acquisition, taken approximately 4 hrs apart. The velocity fields show a circulation that flows in opposition to the clockwise buoyancy-driven cell. For this particular experiment, the surface stress successfully sweeps the flow laterally before the plume has time to descend. The resulting stress-driven circulation appears to be in steady-state as evidenced by the minimal change between successive images in figure 4.5 as well

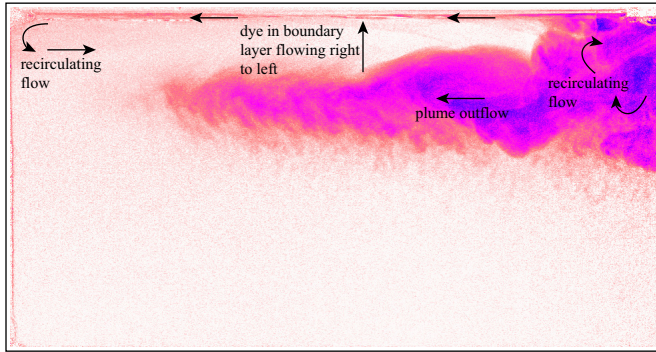


Figure 4.6: Dye image of plume outflow for an experiment with $S_{\delta f} = 0.45$. The dye is solely added to the dense plume fluid, and can be seen in the thin boundary layer at the surface. Traces of dye in the left-hand corner show evidence of a shallow counterclockwise cell that recirculates back to the plume. Black arrows show general direction of flow in corresponding regions.

as by overlapping conductivity profiles in figure 4.7(a). This is the only experiment in which the stress effectively reverses the direction of the buoyancy–driven cell for long timescales, with no evidence lending support for a two–cell system.

Generally, dye visualizations of experiments with $\rho_d \approx 1010 \text{ kg m}^{-3}$ indicate that the surface stress readily advects fluid in a thin boundary layer. The result is a relatively shallow counterclockwise cell near the surface, an example of which is pictured in figure 4.6. The flow inside the boundary layer is reversed and consequently moves away from the plume, only to recirculate toward the plume once it reaches the opposite vertical boundary. The boundary layer thickness is therefore increased from what would be expected in a purely buoyancy driven flow, being almost doubled by the lateral advection and subsequent recirculation into the plume. The boundary layer thickness remains thinner than typical values for larger plume density (see figure 4.13 for a plot of normalized $\delta_{0.95}$).

All experiments with $\rho_d \approx 1010 \text{ kg m}^{-3}$ maintain a long–time stable stratification with no indication of a density inversion within the boundary layer, or anywhere in the flow. The steady nature of these experiments is supported by both the coincident boundary layer thicknesses between two data sets, plotted in figure 4.13, as well as the overlapping normalized buoyancy profiles in figure 4.7(a). Furthermore, the normalized bottom buoyancy measurements in figure 4.8(b) suggest distinctive dynamics that cause

a shift in the data, separating it from experiments at higher Ra_B . The dependence on B_0 therefore seems to be nonlinear.

4.2 Quantitative results

Figure 4.7 plots normalized interior density profiles obtained from conductivity probe measurements extending to approximately the mid-depth of the tank, organized by maximum plume density. The origin of all profiles is taken to be at the interface between the upper fresh water layer and the working volume. A subset of profiles which extend past the normalized value of 1 experienced an electrical drift during the conductivity probe's 38 min traverse to the half-depth of the tank. Physically, it is not possible for the density in the tank to be denser than the plume source, but the raw data are displayed nonetheless for completeness. In the same vein, the profile corresponding to $S_{\delta f} = 0.965$ is included in figure 4.7(c), acknowledging that the flow cannot maintain the large density inversion at depth, and the profile must therefore be a product of eddying features present in the domain which are picked up by the probe.

Experiments which do not exhibit regional mixing at the boundary of the fresh-water layer and underlying circulation maintain a thin boundary layer above a weakly stratified interior, where the fluid density is close to the maximum density input into the experiment. Once mixing ensues ($S_{\delta f} \gtrsim 0.50$), the interior density freshens at all depths and the boundary layer thickens, analogous to observations described in chapter 3, in which the circulation was exposed to localized turbulence near the surface. Generally, the flow becomes more unsteady, as evidenced by the misalignment between the two recorded data sets per each experiment (dashed and solid lines of the same color). The unsteadiness may be either attributed to the induced turbulence present in the flow, or transient adjustment of the circulation in response to the mixing region (see § 3.3 for discussion of relevant timescales).

Figure 4.8(a) plots profiles of the horizontally averaged normalized buoyancy frequency $N^2(z)$, taken from the second set of data acquisition. The vertical density gradient is averaged in the interior, outside any regions of mixing. The profiles reveal a weakly stratified interior density field when no mixing is present in the flow. For

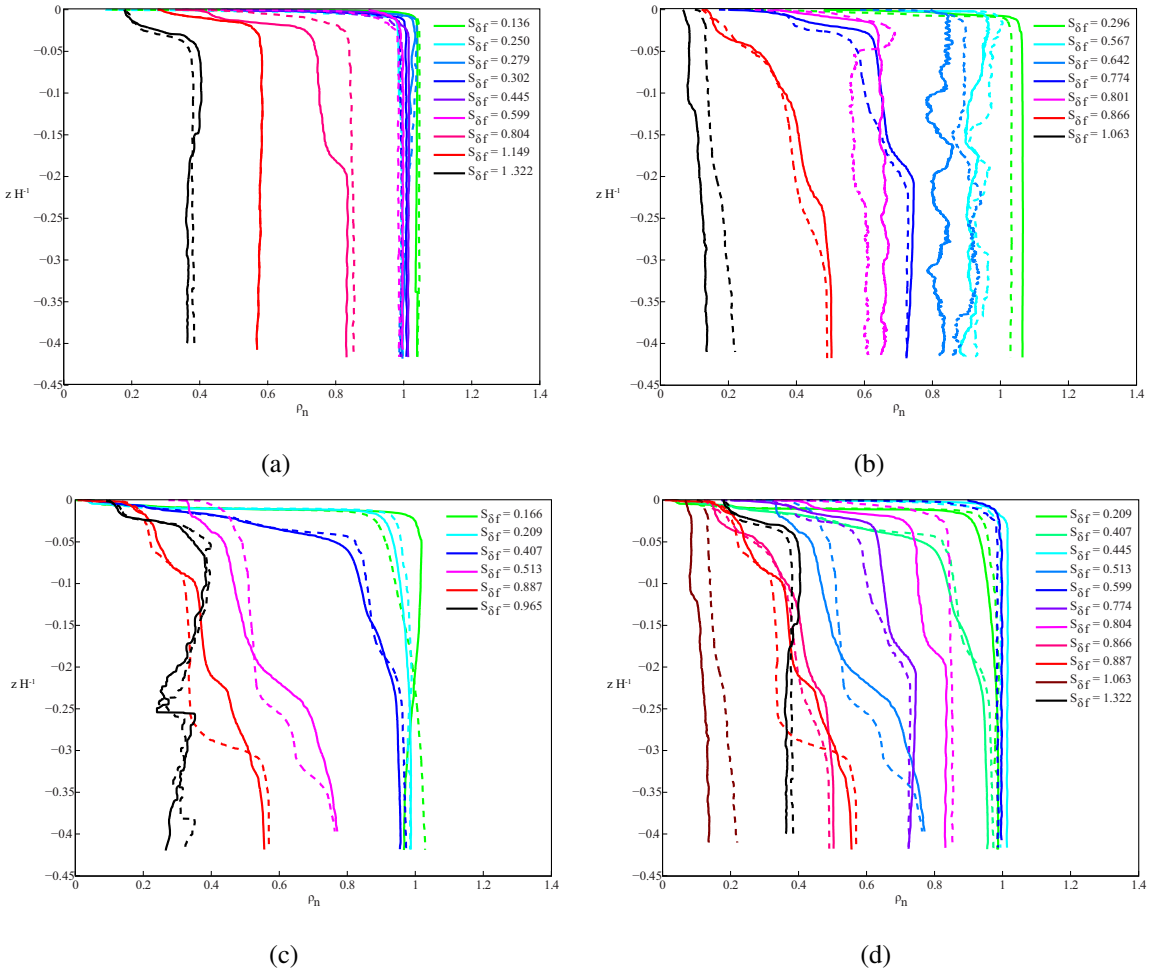


Figure 4.7: Plots of normalized interior density measured by the conductivity probe as a function of normalized depth. Because the conductivity probe could only measure the upper half of the domain, the profiles end just shy of the normalized half-depth of the tank. (a) – (c) display profiles recorded during the first set (solid lines) and second set (dashed lines) of data acquisition. (a) and (b) plot experiments where the initial density of the plume is approximately 1010 kg m^{-3} and 1020 kg m^{-3} , respectively. All experiments show good agreement between the two sets of data collection (approximately half a filling timescale apart, i.e. $\sim 4\text{hrs}$), indicative of the flow reaching an equilibrated state. (c) plots the normalized profiles for an initial plume density of 1030 kg m^{-3} . The two sets of profiles per experiment are misaligned, indicating a noisier circulation. (d) is a cumulative plot of the average normalized density profiles in (a)–(c).

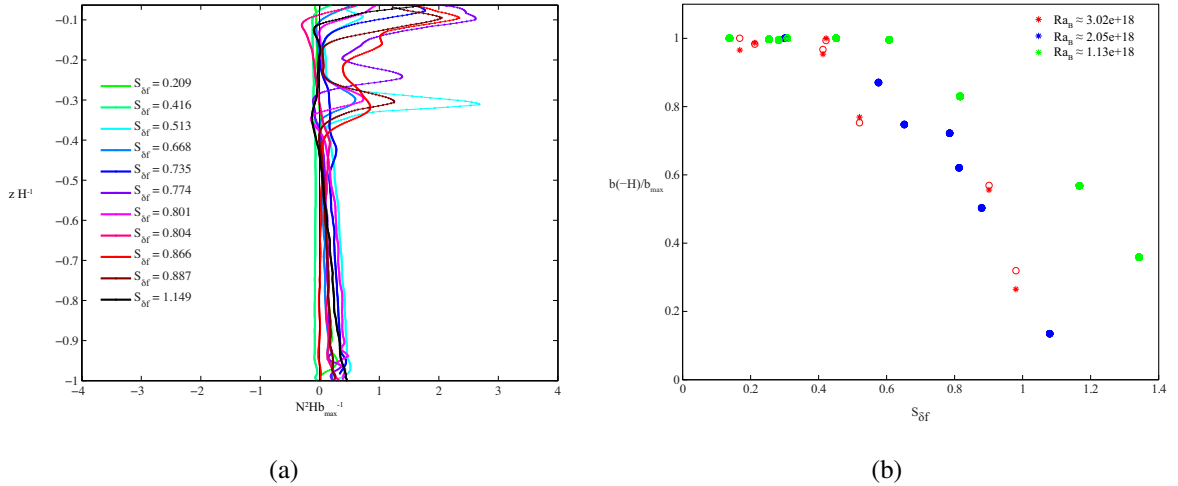


Figure 4.8: (a) Normalized buoyancy frequency profiles as a function of depth for select $S_{\delta f}$ values. The profiles are obtained from SS images by horizontally averaging ρ_z outside of the plume as well as any patches of turbulence. For flows with relatively thin boundary layers, data upstream of $z H^{-1} = 0.5$ corresponds to this region and is an unreliable estimate of the buoyancy frequency due to the steep refractive index gradients. (b) plots the normalized buoyancy obtained from conductivity probe measurements at approximately the mid-depth of the domain. The stars and circles indicate measurements from the first and second data set, respectively. The plot is color-coded to distinguish between the three mean Ra_B values considered.

$S_{\delta f} \gtrsim 0.50$, the stratification is confined to the upper surface, where the plume typically detains. Two protrusions are present below the boundary layer region, corresponding to the finger-like intrusions displayed in figure 4.4(a). A plot of normalized buoyancy measured at mid-depth in figure 4.8(b) once again supports interior freshening for experiments where $S_{\delta f} \gtrsim 0.50$. There is no strong evidence within the studied range of $S_{\delta f}$ values that surface stress alone is capable of pumping buoyant fluid downwards into the circulation. The only mechanism by which the interior is freshened is through shear-induced turbulence near the fresh water source.

Figure 4.9 plots the two recorded horizontally averaged profiles of the horizontal velocity, $u(z)$, for an experiment categorized in the competitive regime with $S_{\delta f} = 0.30$. The time interval between the two profiles is 4 hrs. The first PIV measurement (line with crosses) shows a flow field in which the plume penetrates to about three-quarters of the domain before detraining near the base. The positive velocity values indicate entrainment into the plume, resulting in a maximum $u(z)$ of $\approx 1.2 \text{ mm s}^{-1}$. In contrast, the

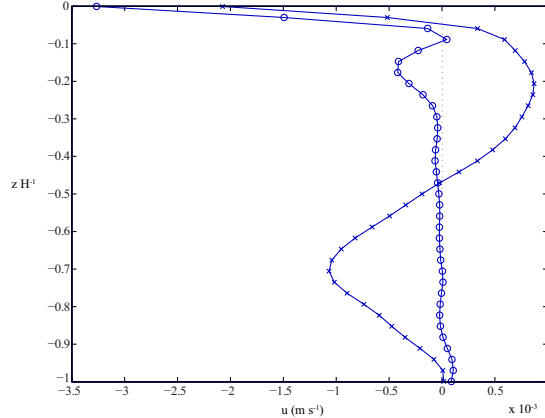


Figure 4.9: Horizontally averaged vertical profiles of u , the horizontal velocity, for an experiment with $S_{\delta f} = 0.30$. The cross and circle line markers correspond to profiles obtained from the first set and second set of data acquisition, respectively. The time interval between the two data sets is 4 hrs.

second profile (line with circles) detains near the surface at approximately 0.5 mm s^{-1} . Therefore, experiments that fall within this competitive regime are dynamic with regard to advection of the flow field. The interior density structure remains largely unchanged below the boundary layer. Even though fluid parcels are being periodically advected in various directions, the fluid itself is mostly uniform everywhere in the domain below the boundary layer. The advected particles are all very close to the same density, rendering virtually no change to the interior density field in response to the advection. If there are density variations, they are too small to be resolved by the conductivity probe. In contrast, figure 4.13 indicates that the density structure in the boundary layer does seem to vary between data acquisition sets for experiments with relatively low $S_{\delta f}$ values, where the fluid parcels cover a wider range of density values.

Figure 4.10(a) plots the maximum velocity magnitude normalized by the maximum surface velocity as a function of $S_{\delta f}$. Vertical lines correspond to the spread of recorded values between data acquisition sets. As evidenced by figure 4.9, it is not expected for the velocity to remain temporally unchanged; the vertical lines are, to some extent, indicators of the spread. It is acknowledged that both points may not encompass the maximal range of the mean velocity magnitude in the system, since data recording was in no way synchronized with the periodicity in the flow. For experiments with $S_{\delta f} > 0.50$, the flow field is relatively more variable between the two data sets. This cor-

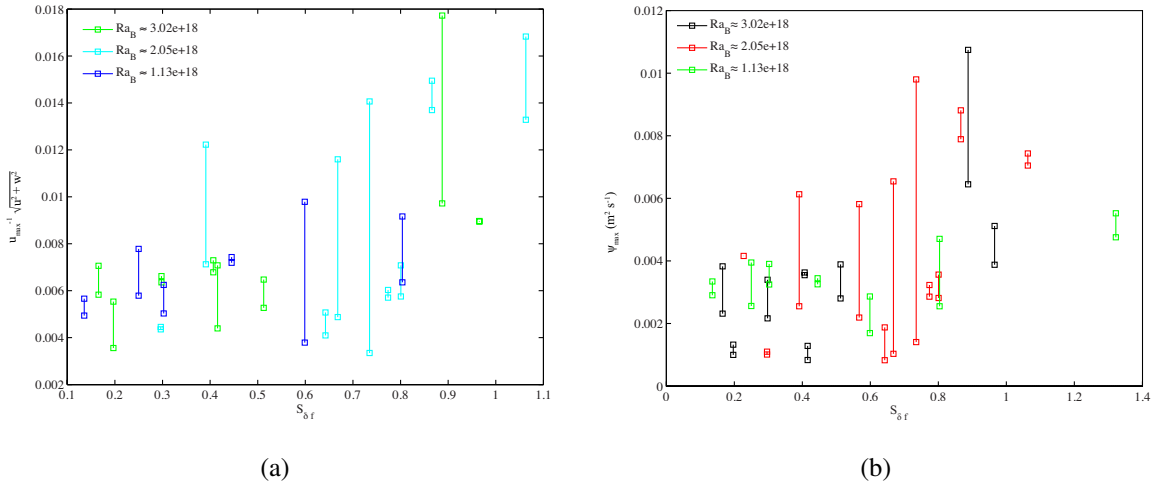


Figure 4.10: (a) Normalized maximum velocity magnitude, $\sqrt{u^2 + w^2}$, obtained from PIV measurements as a function of $S_{\delta f}$. The vertical lines are associated with the spread between the two recorded data sets per each experiment. (b) maximum positive ψ_{max} in the flow. Marker color distinguishes between Ra_B values.

responds to the regime where mixing has started, causing a net input of buoyancy flux into the plume and consequently generating a shallow circulation. The stress–driven upper layer and underlying circulation are competing near the surface, leading to large fluctuations in the velocity magnitude. The maximum positive streamfunction is plotted in figure 4.10(b) to track the response of the buoyancy–driven circulation to increased stress. Once again, data becomes variable after the onset of mixing. The cell is toggling back and forth between clockwise and counterclockwise circulation, leading to either a buoyancy–driven or stress–driven cell, respectively. What is important is the general downward trend of ψ_{max} until $S_{\delta f} \approx 0.67$, at which point it begins to increase. This increase is likely due to fluid escaping from the competitive upper cell and sustaining a buoyancy–driven circulation below, as shown in figure 4.4(b). At the interface of these two cells, both circulations will be directed toward the plume as long as stress dominates the upper cell.

4.2.1 Flow stability

The bulk Richardson number as a function of $S_{\delta f}$ is plotted in figure 4.11, where (3.5) is used to calculate the value. The distance over which Ri_B is calculated is 1.62

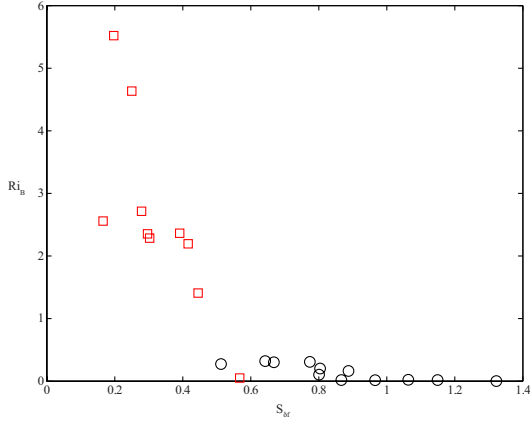


Figure 4.11: Ri_B as defined in eq. (3.5) plotted as a function of $S_{\delta f}$. The red squares correspond to experiments where no mixing is evident in the flow, and the black circles correspond to experiments with visible mixing. The threshold past which mixing occurs is at approximately $S_{\delta f} > 0.51$ corresponding to $Ri_B = 0.27$; all experiments which exhibit mixing maintain $Ri_B < 0.33$.

mm. The first experiment to accommodate a mixing region occurs at $S_{\delta f} = 0.51$, corresponding to $Ri_B = 0.27$. The estimated cutoff for experiments with visible mixing is $Ri_B < 0.33$. Non-mixing experiments maintain $Ri_B > 1.41$, barring one outlier, shown in figure 4.11. The surface flow is expected to be turbulent from the onset since the experiment initializes with no density difference between the freshwater layer and the working volume. Therefore, transition to a laminar regime requires $Rit \geq 1$, consistent with the observed Ri_B threshold. However, it should be noted once again that the calculated value is a bulk Richardson number, and is therefore not expected to be fully compliant with theoretical threshold values. More important is the indication of a transition that effectively separates the stable and unstable flow fields.

4.3 Scaling arguments

The current results may be compared to Hazewinkel et al. (2012), who explored horizontal convection subject to mechanical and buoyancy forcing in the relevant high Pr parameter space of $Ra = 64 \times 10^7$, $Pr = 10$, and $S_\delta = 1.23$, 2.06, and 3.32, where

the maximum buoyancy is used to calculate S_δ and defined as,

$$S_\delta = \frac{\sigma S}{Ra^{3/5}}. \quad (4.1)$$

The authors hypothesize that in the limit $Ra \rightarrow \infty$ and $S \rightarrow \infty$ with Pr , A , and S_δ fixed, relevant quantities should be described well by

$$\delta_{0.95} = L Ra_B^{-1/6} \delta_*(\sigma, S_{\delta_f}, A), \quad (4.2)$$

$$U_s = \kappa L^{-1} Ra_B^{-1/3} \delta_*(\sigma, S_{\delta_f}, A), \quad (4.3)$$

where U_s is a typical horizontal velocity at the surface, and the equations have been adjusted for a buoyancy flux rather than imposed buoyancy difference. Figure 4.12 plots the mean of the normalized surface velocity, obtained by averaging the horizontally averaged profile $u(z)$ in a 3 cm interval approximately 1.5 cm below the surface of the flow. The vertical offset of 1.5 cm ensures that the data is not skewed by the interface of the freshwater layer and underlying circulation. Once again, the vertical bars correspond to the spread between the pair of recorded data sets per experiment. As evidenced in figure 4.9, competitive flows are susceptible to a range of velocities due to the dynamic velocity field, including near the boundary layer. Figure 4.12 suggests that once mixing occurs near $S_{\delta_f} \approx 0.50$, the surface velocity generally switches direction from buoyancy-forced ($+\bar{u}_s$) to stress-forced ($-\bar{u}_s$). Positive surface velocities at low ρ_d corroborate flow reversal in the developed thin boundary layer, which was shown in figure 4.6 to create a shallow recirculation pathway underneath the boundary layer, with flow toward the plume. Because PIV measurements cannot resolve steep regions of density gradient which are expected to occur for these experiments based on boundary layer thicknesses in figure 4.13, the values in figure 4.12 fall below the reversed boundary layer flow, instead picking up the velocity in the recirculating portion of the cell.

Figure 4.13 plots the boundary layer thickness normalized by Ra_B as a function of S_{δ_f} for both data sets. In general, the boundary layer thickness increases with increasing S_{δ_f} . However, there is no visible collapse of data for the range of explored densities using the scaling in (4.2). For some experiments, there is a considerable disparity in the measured boundary layer thicknesses between data sets. This is likely attributed to the unsteadiness of the flow for experiments that fall into the competitive regime.

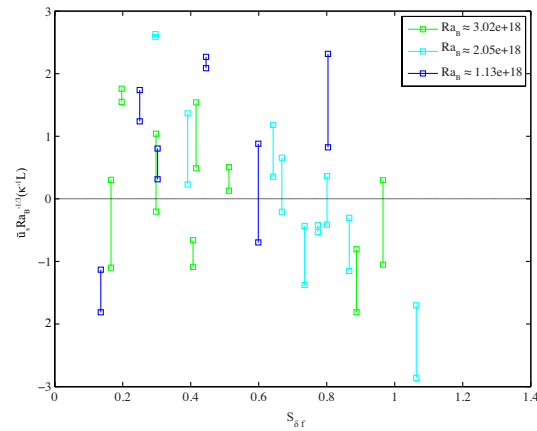


Figure 4.12: Normalized average horizontal surface velocity, obtained from PIV measurements by averaging u in a 3 cm interval approximately 1.5 cm below the surface. The vertical bars are associated with the spread in measurements between each pair of recorded data sets per experiment.

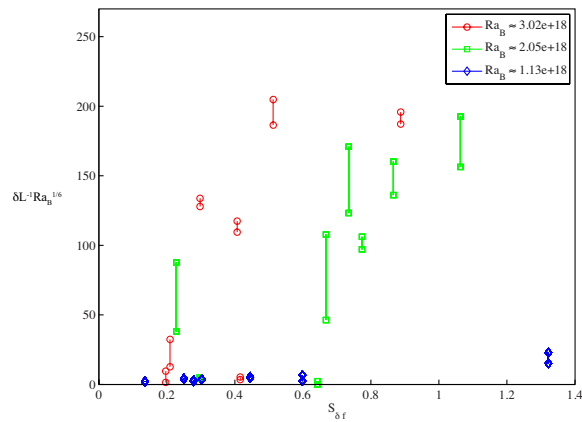


Figure 4.13: Boundary layer thickness scaled by (4.2) plotted as a function of $S_{\delta f}$. The vertical lines correspond to the spread between recorded data sets per each experiment.

The boundary layer thickness responds faster to the surface shear for increasing Ra_B , implying that $\delta_{0.95}$ is proportional to B_0 in some nonlinear sense.

Considering timescales that a fluid parcel may experience as it enters the domain, the time for a parcel to fall through the boundary layer if solely in the presence of a buoyancy forcing is given by,

$$t_{buoy} = \frac{\delta}{B_0^{1/3}}. \quad (4.4)$$

For the same boundary layer thickness, the time required for shear to advect a fluid parcel laterally is

$$t_{shear} = \frac{v}{\tau_{max}}. \quad (4.5)$$

The ratio of the timescales, $t^* = t_{buoy}/t_{shear}$, should then determine whether the shear is fast enough to deflect a parcel from its vertical downward trajectory ($t^* \gg 1$) in the boundary layer, or if the boundary layer is thin enough and/or the buoyancy flux strong enough to sink the parcel before it succumbs to the shear ($t^* \ll 1$). Figure 4.14 plots the timescale as a function of S_{δ_f} for the larger plume density values, using both sets of recorded data per experiment. For low ρ_d , qualitative observations suggest that the boundary layer flow is always stress-dominated, which is not captured by the plot due to the thin boundary layer in the region. At higher values of S_{δ_f} but downstream of the value at which mixing occurs, qualitative observation support a stress-driven flow along the upper surface.

4.4 Discussion

Because the velocity field and boundary layer thickness are unsteady, only general trends in the measurements may be considered. The dispersion in data in figure 4.13 suggest that boundary layers associated with a plume of density $\rho_d = 1020 \text{ kg m}^{-3}$ seem to be the most competitive with the shear stress, or at least the most dynamic in the 4 hrs between data recording. The small change in boundary layer thickness for experiments at $\rho_d = 1010 \text{ kg m}^{-3}$, coupled with qualitative observations, imply that the stress is not competitive with the plume near the surface, but rather readily sweeps fluid parcels laterally from the vicinity of the plume. Because of the lower density, the timescale for

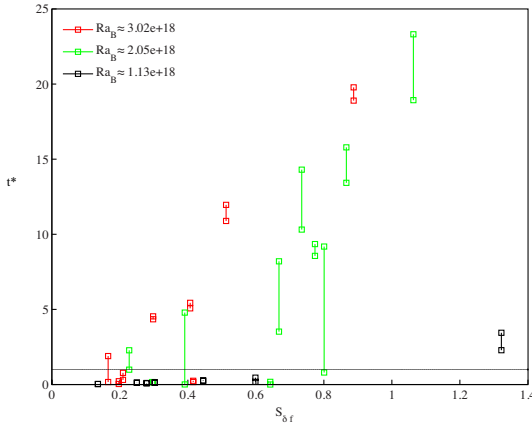


Figure 4.14: Plot of t^* as a function of $S_{\delta f}$. The vertical lines represent the spread in values between two recorded data sets. The experiments for the lowest explored Ra_B seem to always maintain a thin, stress–driven boundary layer, which is not represented correctly in the plot.

reestablishing convection in the cycle may be relatively long compared to other experiments, potentially creating the illusion that the short intervals of recorded data appear to be steady, when in fact the flow requires a longer time to build up enough negative buoyancy for the plume to escape the effect of the surface stress and sink.

In the case of $\rho_d = 1030 \text{ kg m}^{-3}$, the boundary layer thickness also seems relatively unchanged for $S_{\delta f} > 0.30$, but the direction of flow is ambiguous; figure 4.14 would suggest that it is stress–driven, whereas qualitative observations are inconclusive. Typically, if the boundary layer is stress–driven, dye movies show dye picked up by the boundary layer from the plume and swept from right to left by the stress. In some videos, it is hard to decipher if there is any dye in the region. It is possible that the boundary layer velocity is slowed down by the underlying circulation, making it difficult to tell in which direction the layer is flowing. Once mixing occurs, the surface velocity in the boundary layer is stress–controlled for all plume densities considered. No conductivity probe measurements show any indication of a boundary layer density inversion in the interior.

It should be noted that boundary layer measurements with the conductivity probe are prone to error. The boundary layer region tends to be surrounded by faster moving, and at times eddying, flow induced by the overlying freshwater layer. For flows with

strong mixing, the interface between the freshwater layer and working volume becomes increasingly indiscernible, further complicating measurements. Furthermore, the unsteady flow structure observed in the competitive regime may be responsible for altering the profile shape near the boundary layer, whereby parcels covering a range of densities may be advected by the shear stress.

It is unclear why the data for $\rho_d = 1010 \text{ kg m}^{-3}$ sets itself apart from other considered plume densities, since the ratio of stress to buoyancy forcing seems like the relevant measure of the fluid's likelihood to respond to either mechanism. In the same vein, not all experiments are perfectly compartmentalized by their corresponding $S_{\delta f}$ value into regimes of full-depth buoyancy–driven convection ($S_{\delta f} < 0.20$), competitive regime ($0.20 < S_{\delta f} < 0.50$), mixing with partial-depth circulation ($0.50 < S_{\delta f} < 0.87$) and mixing with the formation of an underlying buoyancy–driven cell ($S_{\delta f} > 0.87$). Such dynamic flows are severely undersampled with only two data acquisition sets, and demand longer recording intervals to capture the $\mathcal{O}(\text{hrs})$ periodicity present in a subset of the experiments.

Even if t^* might be somewhat useful for determining if the boundary layer is expected to be stress–driven, the resulting convection in the system is for the most part unknown. The ratio can only offer a snapshot of what is expected to occur in the boundary layer at a given time, since the boundary layer thickness seems to be cyclically adjusting. At moments, some parcels may be completely swept by the surface stress, while others may be only somewhat displaced from a vertical trajectory. This results in complicated dynamics where the plume outflows at an angle into the domain, altering the level of entrainment it experiences. How far the plume penetrates is a function of its buoyancy flux, which is constantly changing as the plume sinks due to entrainment at all levels. Depending on the region of influence of the stress, the plume may sink and become susceptible to stress effects at varying distances from the surface. The different mechanisms for altering the flow pattern almost seem dauntingly endless.

The scalings of Hazewinkel et al. (2012) do not work for the present set of experiments. The authors looked at a much wider parameter space, with Ra values spanning 4 orders of magnitude. At all Ra explored, the plume is not expected to be turbulent, which occurs for $Ra \gtrsim 10^{10}$ (Gayen et al., 2014). Hazewinkel et al. (2012) acknowledge

that once three-dimensional effects and turbulence are present in the system, the Rossby scaling will no longer be valid. The thin boundary layer used for analysis in Hazewinkel et al. (2012) becomes realistically thick in the high Ra_B limit, which alters the region over which the stress and buoyancy forcings are expected to be competitive. The data in figure 4.13 lends strong support for a dynamic boundary layer thickness. It appears that the boundary layer is thinnest for either the stress-driven or buoyancy driven-case, and thickens in the intermediate region as the two mechanisms compete. Figure 4.10(b) suggests that once the stress-driven cell fully develops on the surface (largest S_{δ_f} values explored), the maximum streamfunction is increased beyond that for a very low to no stress case.

For a subset of S_{δ_f} values, the flow is undoubtedly responsive to the surface stress, and the streamfunction will reach a minimum at the point where the stress and buoyancy forcing are most competitive, which deters sinking of the plume. Once the velocity at the surface is completely reversed, a shallow counterclockwise circulation forms at the upper boundary, generally allowing dense water to fall under it to create a two-cell circulation. In the presence of low mixing, the stress and buoyancy are most competitive due to the development of a shallow buoyancy-driven cell which can no longer escape to the abyss. The reversal of the surface velocity does not have to be triggered by small-scale turbulence, as it is observed at smaller S_{δ_f} values than 0.50. Lastly, while the flow is dynamic, the interior density remains relatively unchanged if no mixing is present at the surface. Once mixing ensues, the interior is freshened as the plume advects the fresher fluid through the domain.

4.5 Conclusions

Experiments have been performed to investigate the effect of a surface stress imposed on a buoyancy-driven convective cell such that the surface stress opposes the sense of the circulation on the surface. The flow is studied for three different plume densities as well as a handful of surface stress magnitudes. An effort has been made to classify the observed regimes by corresponding S_{δ_f} thresholds in a general manner, acknowledging that the system is rather complex.

The motivation for carrying out such a study is to provide insight into a coupled buoyancy and mechanically–driven system such as the global oceans, which are subject to average meridional buoyancy fluxes as well as strong wind stress. At times, the wind stress acts in such a direction as to oppose the buoyancy–driven circulation at the surface, and some form of competition between the two forcings is expected for $S_{\delta f} \sim \mathcal{O}(1)$. The experiments have shown that indeed, a competitive region exists. In a broad sense, full–depth buoyancy–driven convection persists for $S_{\delta f} < 0.20$, where the surface stress acts passively on the underlying circulation. Near the transition values $0.20 < S_{\delta f} < 0.50$, a competitive regime appears, in which the flow responds dynamically to the rivalry by altering the thickness of the boundary layer and the strength of the circulation. At times, this regime features a two–cell circulation. There is evidence that the direction of flow in the boundary layer is reversed before small–scale turbulence develops near the surface, for $S_{\delta f} \gtrsim 0.50$. Once mixing develops, the boundary layer flow seems reversed consistently, but engages in a sort of tug–of–war with the now shallow underlying buoyancy–driven circulation. For $S_{\delta f} > 0.87$, a two–cell circulation develops, in which the stress drives a shallow cell near the surface, and the buoyancy drives a deeper underlying cell.

Hazewinkel et al. (2012) quote typical ocean values for the surface stress to buoyancy ratio as $S_{\delta f} = 2400$ and $S_{\delta f} = 24$ in the limits of molecular and eddy viscosities, respectively. In this parameter space, the resulting computations indicate that the flow would consist of a single, stress–driven cell, with the buoyancy acting as a passive scalar. Only one such experiment hinted at the existence of a single, stress–driven cell (see figure 4.5), but it was still confined to the upper half of the domain. Moreover, this happened at relatively low $S_{\delta f}$ values, in fact for one of the lowest values considered. The range of $S_{\delta f}$ values that might trigger a single stress–driven cell is most likely not covered in this study, as the main intent was to maintain $S_{\delta f} \sim \mathcal{O}(1)$. Data at the highest $S_{\delta f}$ values suggest the maintenance of a two–cell circulation. However, when comparing the current results to the ocean, more caution must be taken than just potentially existing in the wrong parameter space. The experiments and resulting data only consider averages in the spanwise direction, thus averaging over any three–dimensional turbulence that is not uniform across the depth. Moreover, rotation is com-

pletely withheld from the analysis, which has implications on the resulting circulation (Barkan et al., 2013). Another shortcoming is the existence of boundaries, and their ability to support laminar sublayers which would otherwise not exist if the plume was displaced at a sufficient distance from vertical walls. To some extent, gravity currents along topographical features are relevant to the oceans, but the study becomes limited by geometric constraints. Nevertheless, a complicated system like the global overturning circulation demands simplification in an experimental setting, and corresponding results must be considered with discretion. What remains to be found is a large- Ra_B scaling that effectively collapses the data in order to compare the effect of each forcing on the system.

Chapter 5

Conclusions

5.1 Overview and application

Two sets of laboratory experiments have been carried out that investigate the effect of mechanical forcing imposed on a circulation driven by surface buoyancy fluxes. The mechanical forcing is provided via a surface stress that acts along the same boundary as the buoyancy forcing. The first set of experiments, discussed in chapter 3, explores the case in which the stress is applied in the same direction as the sense of the buoyancy–driven circulation. The main result of this experimental study is that the stress creates shear–induced turbulence in the upper region of the domain, and therefore contributes to mixing processes in the flow. More specifically, for experiments where $S_{\delta f} > 0.42$, the local stratification near the surface cannot dampen shear–induced unstable modes, consequently forming a region of mixing at the upper boundary. The depth of this mixing region is found to increase linearly with $S_{\delta f}$, and ultimately reach an equilibrium depth determined by a ratio of the surface stress and imposed buoyancy flux. The mixing region creates a vertically nonuniform turbulent diffusivity, $\kappa^*(z)$, which is approximated by a piecewise constant function with an amplified value of κ^* from the surface to the depth of mixing. The diffusivity is parameterized by the characteristics of the developed eddy in the region, but requires the solution of the inverse problem to determine the constant of proportionality.

The experiment data is well described by the recycling box model of Hughes et al. (2007), which is solved numerically in order to incorporate the spatially–varying

$\kappa^*(z)$ profile for each experiment. With increased turbulent diffusivity, the theory predicts an increase in the boundary layer thickness and maximum overturning rate, as well as a smaller top-to-bottom density difference. The streamfunction and boundary layer thickness are underpredicted by the theory, which might be caused by reduced local upwelling at the upper boundary due to the surface stress. In the case of no developed mixing, the experiments are sensitive to a virtual source correction, which is required to take into consideration the finite input of volume flux by the density source. When no external mixing is imposed on the system, Stewart et al. (2012) found that instabilities in the convective flow as well as the turbulent plume amplify the diffusivity by a factor of 2 from its molecular value.

For experiments which exhibit small-scale turbulence on the upper boundary, the circulation is subject to a net input of stabilizing buoyancy as the mixing region develops, causing the plume to detrain at partial depth into the interior. There is supporting evidence that the partial-depth circulation is in a transient state that would require a timescale on the order of years to fully equilibrate, contingent on the mechanism of molecular diffusion to erode the interface between the convective cell and underlying stagnant layer. However, due to the existence of a laminar sublayer which constantly resupplies dense water into the abyss, the system may be in an equilibrated state in which advection of negative buoyancy by the laminar sublayer is exactly balanced by diffusion across the interface, so that there is no net input of buoyancy into the system at any level.

The strong agreement with theory suggests that the bulk of the interior stratification is either set during the early transient stage when the plume is still able to penetrate the full volume, or by the laminar sublayer continually feeding dense water into the relatively stagnant interior. The former hypothesis is supported by work of Stewart et al. (2012) and Vreugdenhil et al. (2015).

Experiment results can be broadly applied to the global oceans, which are subject to wind stress as well as surface buoyancy fluxes in the form of rain, ice formation, and evaporation. Strong winds that blow in the same direction as the upper circulation may induce wind-driven mixing, i.e. small-scale turbulent motion created by the wind stress. While this mechanism is different from wind-driven upwelling in the energy budget, and instead gets categorized as a mixing process, it is still an effect of the wind

on the ocean surface. The main consequence of regional mixing is that it introduces a long-persisting perturbation in the form of an input of stabilizing buoyancy, which leads to a shutdown of the full-depth circulation. Mechanical forcing acting on the surface of bodies of water can span a wide range of timescales, and affect mixing in the thermocline. Because this boundary layer feeds directly into the plume, the plume is able to communicate any perturbations at the surface into the abyss. The change to the overall circulation is then dependent on the type of perturbation imposed in the thermocline. As an example, an increase in the net buoyancy flux results in an energized flow (Mullarney et al. 2004; Griffiths et al. 2013) whereas a decrease results in a shallow convective cell and relatively stagnant interior. A conglomeration of such events occurring on relatively long timescales can set up interesting stratification profiles as the plume continually responds to any changes to the fluid in the thermocline.

For experiments which explored a surface mechanical forcing acting in opposition to the buoyancy-driven circulation at the upper boundary, a suite of interesting regimes are observed; results are described in detail in chapter 4. Specifically, for very low values of $S_{\delta f}$ and relatively large plume densities, the buoyancy-driven circulation remains unaffected by the surface stress. As $S_{\delta f}$ is increased, the two forcings become competitive at the surface, creating a periodic circulation. The surface stress inhibits the plume from reaching the bottom boundary, instead causing it to spread laterally and entrain on itself. As the plume acquires buoyancy flux through the re-entrainment of dense fluid, it escapes the confines of the surface stress and sinks to the bottom. The process is repeated because new fluid replacing the recirculating region is again fresher, and consequently more sensitive to the effects of the surface stress. When $S_{\delta f}$ becomes sufficiently large, near 0.50, small-scale turbulence develops in the upper layer, creating a perturbation in the form of a net buoyancy flux input into the plume, rendering it too weak to penetrate the full depth of the domain. The stress-driven boundary layer flow is observed to compete with the underlying shallow buoyancy-driven cell, such that the flow in either layer pulsates. At even higher $S_{\delta f}$ values, the stress-driven cell is well developed and dense fluid escapes to the bottom boundary, creating a deeper buoyancy-driven flow. The flow dynamics are different for a low density plume. The resulting boundary layer thickness increases with $S_{\delta f}$, and the Rossby scaling describing

the boundary layer seems to be no longer relevant for the system.

In an oceanographic context, the results provide some insight into the existence of a multi-cell overturning structure in the global oceans (Hazewinkel et al., 2012). The experiments are carried out in a larger parameter space than has been allowed by numerical simulations, which are limited by computational costs. In this high Ra_B and Pr regime, a two-cell structure may still exist under certain conditions. The experiments certainly show a competitive regime between the two forcings that develops before any regional mixing exists in the flow. The results also suggest that once the surface stress is able to create a shallow stress–driven cell at the upper boundary, it works to increase the maximum overturning transport in the presence of an underlying buoyancy–driven cell.

5.2 Future work

The experiments carried out in this work have introduced a series of new questions whose consideration should help explain current results. For one, the timescale issue in the experiments of chapter 3 needs to be resolved. Because salt–driven experiments have such a small molecular diffusivity, they are not ideal for investigating the longest timescales in the system, which are proportional to κ^{-1} . However, thermally–driven horizontal convection may be run for the full long diffusive timescale, and would put to rest the question of whether a partial–depth circulation coupled with a laminar sublayer is a steady–state solution to the system.

Another question of interest is the robustness of the results to the experimental setup. No previous experiments have shown any evidence of a laminar sublayer, and it is unclear what role it plays in maintaining the observed circulation. Moreover, what would be the response of the circulation in the case of an isolated plume? Such a different plume geometry is likely to change the equilibrated density and velocity fields. The current experimental setup also does not provide a pure buoyancy flux condition, and must always be accompanied by an input of volume flux. Additionally, the maximum density is set by the plume source. All of these conditions cause the experiment to deviate from pure horizontal convection, and should be considered in the next iteration of

the experimental setup. It is also unclear if the fact that the surface stress is not imposed directly above the plume source is important in the overall analysis. Intuitively, if the surface stress acted directly above the destabilizing buoyancy source, one would expect an amplification in the response of the buoyancy–driven cell to the mechanical forcing.

Experiments which investigate a competitive mechanical forcing require numerical simulations at high Ra_B and increased sampling of the velocity and density fields in the laboratory. The periodicity of the flow no longer allows for the exploitation of a steady–state circulation in which all data may be recorded in a short time interval, but does not have to be carried out simultaneously. To truly understand the flow structure, PIV measurements should be synchronized with synthetic schlieren measurements, and the velocity and density fields should be sampled for a full cycle. As it stands, the only information known about the timescale of the periodicity is that it is on the order of hrs, and dependent on the ratio of mechanical to buoyancy forcing. Once computational limitations are overcome, the numerical simulations of Hazewinkel et al. (2012) will be of interest in higher parameter space, which is more relevant to the current experiments as well as the global oceans. Lastly, all experiments are performed in a two–dimensional world with no Coriolis force–two restrictions that, if rectified, can offer a truer comparison to reality. This has already been done numerically by Barkan et al. (2013). Horizontal convection experiments in a rotating configuration are being currently set up (K. Stewart, personal communication) and will offer some laboratory insight in regard to the role of the plume as well as additional instabilities that are not supported in a rectangular domain.

Bibliography

- Adrian, R. and Westerweel, J. (2011). *Particle Image Velocimetry*. Cambridge University Press.
- Anton Paar GmbH (2002). *DMA 4500/5000 Density/specific gravity/concentration meter instruction handbook*. Austria, Europe.
- Baines, W. D. and Turner, J. S. (1969). Turbulent buoyant convection from a source in a confined region. *J. Fluid Mech.*, 37:51–80.
- Barkan, R., Winters, K. B., and Smith, S. G. L. (2013). Rotating horizontal convection. *J. Fluid. Mech.*, 723:556–586.
- Barkan, R., Winters, K. B., and Smith, S. G. L. (2015). Energy cascades and loss of balance in a reentrant channel forced by wind stress and buoyancy fluxes. *Journal of Physical Oceanography*.
- Batchelor, G. K., Moffatt, H. K., and Worster, M. G., editors (2000). *Perspectives in Fluid Dynamics*. Cambridge University Press.
- Beardsley, R. C. and Festa, J. F. (1972). A numerical model of convection driven by a surface stress and non-uniform horizontal heating. *J. Phys. Oceanogr.*, 2:444–455.
- Benítez, J. (2009). *Principles and modern applications of mass transfer operations*. John Wiley & Sons, 2nd edition.
- Chiu-Webster, S., Hinch, E. J., and Lister, J. R. (2008). Very viscous horizontal convection. *J. Fluid Mech.*, 611:395–426.
- Coman, M. A., Griffiths, R. W., and Hughes, G. O. (2006). Sandström’s experiments revisited. *J. Mar. Res.*, 64:783–796.
- Dalziel, S., Hughes, G., and Sutherland, B. (2000). Whole-field density measurements by ‘synthetic schlieren’. *Exp. in Fluids*, 28:322–335.
- Dalziel Research Partners (2008). *DigiFlow User Guide*.
- Defant, A. (1961). *Physical Oceanography*, volume 1. Pergamon, New York.

- Dewar, W. K., Bingham, R. J., Iverson, R. L., Nowacek, D. P., St. Laurent, L. C., and Wiebe, P. H. (2006). Does the marine biosphere mix the ocean? *J. Mar. Res.*, 64:541–561.
- Edmund Optics (2013). Using cylinder lenses. <http://www.edmundoptics.com/technical-resources-center/optics/using-cylinder-lenses/>.
- Gayen, B., Griffiths, R., and Hughes, G. (2014). Stability transitions and turbulence in horizontal convection. *J. Fluid Mech.*, 751:698–724.
- Gayen, B., Griffiths, R. W., Hughes, G. O., and Saenz, J. A. (2012). Energetics of horizontal convection. *J. Fluid. Mech. Rapids*.
- Griffiths, R. W., Hughes, G. O., and Gayen, B. (2013). Horizontal convection dynamics: insights from transient adjustment. *J. Fluid. Mech.*
- Hazewinkel, J., Paparella, F., and Young, W. (2012). Stressed horizontal convection. *J. Fluid. Mech.*, 692:317–331.
- Hecht, E. (2002). *Optics*, chapter 13. Pearson Addison Wesley, San Francisco, fourth edition.
- Hopfinger, E. J. and Linden, P. F. (1982). Formation of thermoclines in zero-mean-shear turbulence subjected to a stabilizing buoyancy flux. *J. Fluid. Mech.*
- Hughes, G. O. and Griffiths, R. W. (2006). A simple convective model of the global overturning circulation, including effects of entrainment into sinking regions. *Ocean Model.*, 12:46–79.
- Hughes, G. O. and Griffiths, R. W. (2008). Horizontal convection. *Annu. Rev. Fluid Mech.*, 40:185–208.
- Hughes, G. O., Griffiths, R. W., Mullarney, J. C., and Peterson, W. H. (2007). A theoretical model for horizontal convection at high Rayleigh number. *J. Fluid. Mech.*, 581:251–276.
- Hughes, G. O., Hogg, A. M., and Griffiths, R. W. (2009). Available potential energy and irreversible mixing in the meridional overturning circulation. *J. Phys. Oceanogr.*, 39:3130–3146.
- Ilicak, M. and Vallis, G. K. (2012). Simulations and scaling of horizontal convection. *Tellus A*, 64:18377.
- Jeffreys, H. (1925). On fluid motions produced by differences of temperature and humidity. *Q.J. Royal Meteor. Soc.*, 51:347–356.
- Johnson, H. L., Marshall, D. P., and Sproson, D. A. J. (2007). Reconciling theories of

- a mechanically driven meridional overturning circulation with thermohaline forcing and multiple equilibria. *Clym, Dyn.*, 29:821–836.
- Kanda, I. (2002). *Conductivity Measurement System*.
- Killworth, P. (2001). On the rate of descent of overflows. *Journal of Geophysical Research*, 106:22267–22275.
- Killworth, P. D. and Manins, P. C. (1980). A model of confined thermal convection driven by non-uniform heating from below. *J. Fluid. Mech.*
- Kuhlbrodt, T., Griesel, A., Montoya, M., Levermann, A., Hofmann, M., and Rahmstorf, S. (2007). On the driving processes of the atlantic meridional overturning circulation. *Reviews of Geophysics*, 45:(RG2001).
- Kundu, P. K., Cohen, I. M., and Dowling, D. R. (2012). *Fluid Mechanics*. Elsevier Inc., 5th edition.
- LaVision (2004). *DaVis Software Manual for DaVis 6.2*. LaVision GmbH, Gottingen.
- Linden, P. F. (1999). The fluid mechanics of natural ventilation. *Annu. Rev. Fluid Mech.*, 31:201–238.
- Manins, P. C. (1979). Turbulent buoyant convection from a source in a confined region. *J. Fluid. Mech.*
- Morton, B. R., Sir Geoffrey Taylor, F. R. S., and Turner, J. S. (1956). Turbulent gravitational convection from maintained and instantaneous sources. *Proc. R. Soc. Lond. A*, 234.
- Mullarney, J. C., Griffiths, R. W., and Hughes, G. O. (2004). Convection driven by differential heating at a horizontal boundary. *J. Fluid Mech.*, 516:181–209.
- Mullarney, J. C., Griffiths, R. W., and Hughes, G. O. (2007). The role of freshwater fluxes in the thermohaline circulation: insights from a laboratory analogue. *Deep-Sea Res. I*.
- Munk, W. (1966). Abyssal recipes. *Deep-Sea Res.*, 13:707–730.
- National Instruments Inc. (2011). *NI myDAQ User Guide and Specifications*. <http://www.ni.com/pdf/manuals/373060e.pdf>.
- New Wave Research (2002). *Operator's Manual: Solo PIV Nd:YAG Laser*. Fremont, CA. Part No. 90-1020B.
- Nycander, J., Nilsson, J., Döös, K., and Broström, G. (2007). Thermodynamic analysis of ocean circulation. *Journal of Physical Oceanography*.

- Pankratov (1994). How to compute a streamfunction?
- Paparella, F. and Young, W. R. (2002). Horizontal convection is non-turbulent. *J. Fluid Mech.*, 466:205–214.
- Parker, V. (1965). Thermal properties of uni-univalent electrolytes. *Natl. Stand. Ref. Data Series*, 2.
- Pierce, D. W. and Rhines, P. B. (1996). Convective building of a pycnocline: laboratory experiments. *J. Phys. Oceanogr.*, 26:176–190.
- Pierce, D. W. and Rhines, P. B. (1997). Convective building of a pycnocline: a two-dimensional non-hydrostatic numerical model. *J. Phys. Oceanogr.*, 27:909–925.
- Pope, S. B. (2000). *Turbulent Flows*. Cambridge University Press.
- Raffel, M., Willert, C., and Kompenhans, J. (1998). *Particle image velocimetry: a practical guide*, chapter 2. Springer, New York.
- Rossby, T. (1965). On thermal convection driven by non-uniform heating from below: an experimental study. *Deep-Sea Res.*, 12:9–16.
- Rossby, T. (1998). Numerical experiments with a fluid heated non-uniformly from below. *Tellus*, 50A:242–257.
- Sandström, J. W. (1908). Dynamische versuche mit meerwasser. *Annalen der Hydrographic und Maritimen Meteorologie*, 36:6–23.
- Schindelin, J., Arganda-Carreras, I., Frise, E., Kaynig, V., Longair, M., Pietzsch, T., Preibisch, S., Rueden, C., Saalfeld, S., Schmid, B., Tinevez, J., White, D., Hartenstein, V., Eliceiri, K., Tomancak, P., and Cardona, A. (2012). Fiji: an open-source platform for biological-image analysis. *Nature Methods*, 9(7):676–682.
- Schmittner, A. (2005). Decline of the marine ecosystem caused by a reduction in the Atlantic overturning circulation. *Nature*, 434:628–633.
- Scotti, A. and White, B. (2011). Is horizontal convection really “non-turbulent”? *Geophys. Res. Lett.*
- Sharqawy, M. H., V, J. H. L., and Zubair, S. M. (2010). Thermophysical properties of seawater: A review of existing correlations and data. *Desalination and Water Treatment*.
- Stewart, K. D., Hughes, G. O., and Griffiths, R. W. (2012). The role of turbulent mixing in an overturning circulation maintained by surface buoyancy forcing. *Journal of Physical Oceanography*, 42:1907–1922.

- Stull, R. B. (1988). *An introduction to boundary layer meteorology*. Kluwer Academic Publishers.
- Tailleux, R. and Rouleau, L. (2010). The effect of mechanical stirring on horizontal convection. *Tellus*, 62A:138–153.
- Thielicke, W. (2014). *The Flapping Flight of Birds – Analysis and Application*. PhD thesis, Rijksuniversiteit Groningen.
- Thielicke, W. and Stamhuis, E. J. (2014). Pivlab - towards user-friendly, affordable, and accurate digital particle image velocimetry in MATLAB. *Journal of Open Research Software*, 2(e30).
- Toggweiler, J. R. and Samuels, B. (1997). On the ocean's large-scale circulation near the limit of no vertical mixing. *J. Phys. Oceanogr.*, 28:1832–1852.
- Vallis, G. K. (2000). Large-scale circulation and production of stratification: effects of wind, geometry, and diffusion. *Journal of Physical Oceanography*.
- Vellinga, M. and Wood, R. A. (2002). Global climatic impacts of a collapse of the Atlantic Thermohaline Circulation. *Climatic Change*, 54:251–267.
- Velmex Inc. (1996). *VP9000 Series Stepping Motor Controllers User's Guide*. Bloomfield, NY.
- Vreugdenhil, C. A., Hogg, A. M., Griffiths, R. W., and Hughes, G. O. (2015). Adjustment of the meridional overturning circulation and its dependence on abyssal and upper ocean mixing. Submitted to *Journal of Physical Oceanography*.
- Wang, W. and Huang, R. X. (2005). An experimental study on thermal circulation driven by horizontal differential heating. *J. Fluid Mech.*, 540:49–73.
- Whitehead, J. A. and Wang, W. (2008). A laboratory model of vertical ocean circulation driven by mixing. *American Meteorological Society*, 38:1091–1106.
- Winters, K. B. and Young, W. R. (2009). Available potential energy and buoyancy variance in horizontal convection. *J. Fluid Mech.*, 629:221–230.
- Wunsch, C. (2005). The total meridional heat flux and its oceanic and atmospheric partition. *J. Climate*, 18:4374–4380.
- Wunsch, C. and Ferrari, R. (2004). Vertical mixing, energy, and the general circulation of the ocean. *Annu. Rev. Fluid Mech.*, 36:281–314.